Università degli Studi di Bologna - Alma Mater Studiorum

Dipartimento di Fisica e Astronomia
SCUOLA DI SCIENZE
Corso di Laurea in Astrofisica e Cosmologia

Tesi di Laurea

Looking for intermediate mass black holes in globular clusters using action-based dynamical models

Candidato:
Eric Giunchi

Relatore:
Chiar.mo Prof. Carlo Nipoti

Correlatore:
Dott. Raffaele Pascale

Anno Accademico 2019–2020
Sessione II

Questa Tesi è dedicata a tutti coloro che hanno sempre creduto in me, e su cui so che potrò sempre contare.
Alla mia famiglia, per avermi cresciuto con amore e per avermi insegnato tutti i valori che fanno di me la persona che sono. Non so quanto lontano mi porterà il viaggio che sto per intraprendere, ma so che in voi potrò sempre trovare un posto da chiamare casa. Vi voglio bene.
Ai miei amici, perché alla fine, in tutti questi anni, ci siete sempre stati. Una costante nella mia vita, che spero possa rimanere tale anche in futuro.
A Silvia, e il perché non devo neanche spiegarlo. La lontananza, sai, è come il vento.

Contents

Abstract

The aim of this project is to study the structural and kinematic properties of globular clusters (GCs) by means of novel dynamical models based on analytic distribution functions (DFs) depending on the action integrals. In particular, we focus on the open question of presence or absence of intermediate mass black holes (IMBHs) at the center of these systems. In analogy with galaxies, which host supermassive back holes of mass $\mathrm{M_{BH}} \sim 10^6 - 10^9\,\mathrm{M_\odot}$ at their center, we might expect GCs to host central IMBHs with $\mathrm{M_{BH}} \sim 10^2 - 10^3\,\mathrm{M_\odot}$ (Greene, Strader & Ho, 2019).

As discussed in detail in van der Marel & Anderson (2010) and Greene, Strader & Ho (2019), the existence of IMBHs is still controversial, due to: 1) observational and technical issues in collecting kinematic tracers, as the typical extent of the region where we might see the gravitational effects of these BHs is, at best, comparable with the spatial resolution of current telescope capabilities; 2) mass segregation, which can drag towards the center of the system both the most massive stars, introducing a gradient in the mass-to-light ratio M/L, and the stellar-mass remnants to the center, whose cumulative gravitational effects can mimic the ones of an IMBH; 3) black hole-anisotropy degeneracy, which can be broken considering proper motions or with a high statistics in the central region; 4) uncertainties in the determination of the center of the GC, which can bias surface brightness and line-of-sight velocity dispersion profiles, leading to wrong inferences on the presence and mass of the IMBH.

In this Thesis, we use a novel family of DFs to produce dynamical models of simulated observations of GCs (mocks) by the 5-th Gaia Challenge. These mocks are equilibrium spherical N-body systems, they are generated from DFs and can either have or not a central IMBH. Dealing with mocks rather than real GCs allows us to test the efficiency of our dynamical models and to explore how much statistics we need to constrain the existence of an IMBH in an ideal GC, whose characteristics and parameters are known a priori.

For a steady-state collisionless system, a DF is a normalizable function of the phase-space coordinates $(\mathbf{x}, \mathbf{v})$ which gives the probability of finding a star at a given point of the phase space and encodes all the kinematic characteristics of the system itself. By means of the Jeans (1915) theorems, every equilibrium system can be described by a DF that depends on the phase-space coordinates $(\mathbf{x}, \mathbf{v})$ only through isolating integrals of motion. The actions $\mathbf{J}$ are a special set of integrals of motion: together with their conjugated angles $\boldsymbol{\theta}$, they form a set of canonical coordinates; furthermore, action-based DFs can easily deal with multi-component models and can be extended to add rotation and/or flattening (Binney, 2014).

Dynamical models based on $f(\mathbf{J})$ DFs have already been applied in other studies to model the Milky Way (Sanders & Binney, 2014; Cole & Binney, 2016), dwarf spheroidals (Pascale et al., 2018) and GCs (Jeffreson et al., 2017; Pascale et al., 2019). The analytic $f(\mathbf{J})$ DF we use is the one introduced by Pascale et al. (2018). The DF depends on very few free parameters and, in the absence of other components, it produces anisotropic spherical systems with a density distribution with a core of constant density in the center and exponentially truncated in the outer parts.

We selected four mock GCs, which mainly differ in the number of stars and in the mass of the central IMBH. For each mock we compute the binned stellar projected number density $\Sigma_\star(R)$, we discuss the dependence of the line-of-sight velocity dispersion profile $\sigma_{\rm los}(R)$ on the binning, we produce a realistic profile and we assign to the profiles realistic uncertainties. We compare them through χ^2 fitting with the ones derived from the DF-based models and test the models. The observables of the models are computed using the software package AGAMA[1] (Action-based Galaxy Models Architecture; Vasiliev 2019). Exploring the parameter space, we infer best fit values and confidence intervals of the free parameters, including the BH-to-stellar mass fraction $\mu_{\rm BH}$, to be compared to the known input values of the mock.

Our results show that, for what concerns $\mu_{\rm BH}$, the true value falls within the 1σ confidence level for the mocks with a total number of particles $N \simeq 10^3$ and within the 2σ confidence level in the case of $N \simeq 10^4$. Thus, we can trust, for an hypothetical system of unknown $\mu_{\rm BH}$, that the real value of $\mu_{\rm BH}$ falls within 1σ or 2σ, dependent of the total number of particles. In the case of the studied mocks: for $N \simeq 10^4$ we get $\mu_{\rm BH} = 0.020^{+0.012}_{-0.014}$ when $\mu_{\rm BH,true} = 0.01$ (i.e. $\rm M_{BH,true} = 10^4\,M_\odot$), and $\mu_{\rm BH} \leqslant 0.020$ when $\mu_{\rm BH,true} = 0.001$ (i.e. $\rm M_{BH,true} = 10^3\,M_\odot$); for $N \simeq 10^3$ we get $\mu_{\rm BH} \leqslant 0.013$ when $\mu_{\rm BH,true} = 0.01$, and $\mu_{\rm BH} \leqslant 0.010$ when $\mu_{\rm BH,true} = 0.001$.

The isotropic velocity distribution of the mocks is reproduced within 1σ in the case of $\mu_{\rm BH,true} = 0.001$ and within 3σ when $\mu_{\rm BH,true} = 0.01$. The fact that the model better infers the velocity distribution of the mock when $\mu_{\rm BH}$ is smaller can be an indication of the fact that the adopted DF is not flexible enough, even if this does not affect the ability of the models to infer the correct BH-to-stellar mass fraction.

The true total mass of the system $\rm M_{\star,true} = 10^6\,M_\odot$ falls within 1σ in case of $N \simeq 10^4$, while it is at most within 2σ for the mocks with $N \simeq 10^3$. Thus, we can trust that, for a system of unknown total mass, the real value of $\rm M_\star$ falls within 1σ if $N \simeq 10^4$ or within 2σ if $N \simeq 10^3$. Therefore, the inferred total masses for the studied mocks are the following. If $N \simeq 10^4$, $\log(\rm M_\star/M_\odot) = 6.002^{+0.003}_{-0.003}$ when $\mu_{\rm BH,true} = 0.01$ and $\log(\rm M_\star/M_\odot) = 6.000^{+0.005}_{-0.005}$ when $\mu_{\rm BH,true} = 0.001$. If $N \simeq 10^3$, $\log(\rm M_\star/M_\odot) = 6.03^{+0.0083}_{-0.008}$ when $\mu_{\rm BH,true} = 0.01$ and $\log(\rm M_\star/M_\odot) = 5.955^{+0.050}_{-0.055}$ when $\mu_{\rm BH,true} = 0.001$.

Before applying the method developed in this Thesis to real GCs, in the near future we plan to perform more detailed model-data comparison (for instance including individual velocity measurements and/or proper motions of stars), which should significantly improve our ability to constrain the mass of the IMBH.

---

[1] `https://github.com/GalacticDynamics-Oxford/Agama`

Riassunto del progetto di Tesi in lingua italiana

L'obiettivo di questo progetto è studiare le proprietà strutturali e cinematiche degli ammassi globulari (GCs) per mezzo di nuovi modelli dinamici basati su funzioni di distribuzione (DFs) analitiche dipendenti dagli integrali azione. In particolare, ci concentriamo sulla questione ancora aperta della presenza o meno di buchi neri di massa intermedia (IMBHs) al centro di questi sistemi. In analogia con le galassie, che ospitano nei loro centri buchi neri supermassicci di massa $\mathrm{M_{BH}} \sim 10^6 - 10^9\,\mathrm{M_\odot}$, possiamo aspettarci che nei GCs risiedano IMBHs aventi $\mathrm{M_{BH}} \sim 10^2 - 10^3\,\mathrm{M_\odot}$ (Greene, Strader & Ho, 2019).

Come discusso in dettaglio da van der Marel & Anderson (2010) e Greene, Strader & Ho (2019), l'esistenza degli IMBHs è ancora controversa, a causa di: 1) difficoltà strumentali e osservative nel raccogliere i dati sui traccianti cinematici, in quanto l'estensione tipica della regione dove ci si potrebbe aspettare di avere evidenze degli effetti gravitazionali di un ipotetico IMBH sono, nei migliori dei casi, comparabili con la risoluzione spaziale dei telescopi moderni; 2) segregazione di massa, un processo che tende a portare verso il centro del sistema sia le stelle più massicce, introducendo un gradiente nel rapporto massa-luminosità M/L, sia remnant di stelle massicce (come buchi neri stellari o stelle di neutroni), che potrebero riprodurre gli stessi effetti gravitazionali di un IMBH; 3) degenerazione massa-anisotropia, che può essere rotta prendendo in considerazione anche i moti propri delle stelle o avendo a disposizione un'elevata quantità di dati nelle regioni centrali; 4) incertezze nella determinazione del centro del GC, che possono alterare i profili di brillanza superficiale e di dispersione di velocità lungo la linea di vista, portando a conclusioni errate circa la presenza o meno di un IMBH.

In questa Tesi verrà utilizzata una nuova famiglia di DFs, al fine di generare modelli dinamici da applicare a una serie di osservazioni simulate di GCs (mock) distribuite dalla 5-th Gaia Challenge. Questi mock sono sistemi sferici N-body all'equilibrio, sono generati anch'essi da DFs e possono includere al loro centro un IMBH. Trattando i mock, di cui conosciamo a priori tutte le caratteristiche, anziché sistemi reali, abbiamo la possibilità di verificare l'efficienza dei nostri modelli dinamici e di studiare quanta statistica sia necessaria per avere forti vincoli sulla presenza di un IMBH al centro di un GC ideale.

Per un sistema non collisionale e stazionario, una DF è una funzione normalizzabile nelle coordinate $(\mathbf{x}, \mathbf{v})$ dello spazio delle fasi, che fornisce la probabilità di trovare una stella in un determinato punto dello spazio delle fasi e che determina univocamente tutte le proprietà cinematiche del sistema. Per mezzo dei teoremi di Jeans (Jeans, 1915), ogni sitema all'equilibrio può essere descritto da una DF dipendente dalle coordinate $(\mathbf{x}, \mathbf{v})$ nello spazio delle fasi solo tramite integrali primi del moto. Le azioni $\mathbf{J}$ sono un set particolare di integrali del moto: insieme alle loro coordinate coniugate $\boldsymbol{\theta}$, formano un set di coordinate canoniche; inoltre, DFs dipendenti dalle azioni possono essere ottimamente utilizzate nella costruzione di modelli a più componenti, e possono essere estese per includere rotazione e/o schiacciamento (Binney, 2014).

Modelli dinamici basati sulle DFs dipendenti dalle azioni $f(\mathbf{J})$ sono stati già applicati in altri studi, al fine di descrivere la Via Lattea (Sanders & Binney, 2014; Cole & Binney, 2016), le galassie nane sferoidali (Pascale et al., 2018) e i GCs (Jeffreson et al., 2017; Pascale et al., 2019). La DF analitica $f(\mathbf{J})$ qui utilizzata è quella introdotta da Pascale et al. (2018). La DF dipende da pochi parametri liberi e, in assenza di altre componenti, produce sistemi sferici anisotropi con una distribuzione di densià avente un core di densità costante al centro e un troncamento esponenziale nelle regioni più esterne.

Per questa Tesi abbiamo selezionato quattro mock, che differiscono principalmente nel numero di stelle e nella massa dell'IMBH. Per ogni mock viene costruito un profilo di densità numerica proiettata $\Sigma_\star(R)$ raggruppando in bin i dati simulati, viene discussa la dipendenza dal binning del profilo di dispersione di velocità lungo la linea di vista $\sigma_{\rm los}$, e vengono generati dei profili a cui vengono assegnati incertezze realistiche. Tali profili vengono confrontati con quelli ottenuti dai modelli basati su DFs tramite la tecnica del χ^2. Le osservabili dei modelli vengono calcolate tramite il pacchetto software AGAMA (Action-based Galaxy Models Architecture; Vasiliev 2019). Esplorando lo spazio dei parametri, vengono individuati i valori di best fit dei parametri liberi del sistema, inclusa la frazione in massa del BH rispetto alla massa stellare del sistema $\mu_{\rm BH}$, da confrontare con i reali valori con cui sono stati costruiti i mock.

I nostri risultati mostrano che, per quanto concerne $\mu_{\rm BH}$, il valore reale cade entro l'intervallo di confidenza 1σ per i mock aventi un numero totale di stelle $N \simeq 10^3$, ed entro il livello di confidenza 2σ nel caso di $N \simeq 10^4$. Di conseguenza, possiamo inferire che, per un sistema ipotetico con $\mu_{\rm BH}$ sconosciuto, il valore reale di $\mu_{\rm BH}$ cada entro 1σ o 2σ a seconda del numero totale di particelle. Nel caso dei mock in esame: per $N \simeq 10^4$ otteniamo $\mu_{\rm BH} = 0.020^{+0.012}_{-0.014}$ quando $\mu_{\rm BH,true} = 0.01$ (per cui $\mathrm{M_{BH,true}} = 10^4\,\mathrm{M_\odot}$), e $\mu_{\rm BH} \leqslant 0.020$ quando $\mu_{\rm BH,true} = 0.001$ (corrispondente a $\mathrm{M_{BH,true}} = 10^3\,\mathrm{M_\odot}$); per $N \simeq 10^3$ troviamo $\mu_{\rm BH} \leqslant 0.013$ quando $\mu_{\rm BH,true} = 0.01$, e $\mu_{\rm BH} \leqslant 0.010$ quando $\mu_{\rm BH,true} = 0.001$.

La distribuzione di velocità isotropa dei mock è riprodotta entro 1σ nel caso di $\mu_{\rm BH,true} = 0.001$ ed entro 3σ per $\mu_{\rm BH,true} = 0.01$. Il fatto che il modello riproduca meglio la distribuzione di velocità del mock quando $\mu_{\rm BH}$ è più piccolo può essere un'indicazione del fatto che la DF utilizzata non sia abbastanza flessibile, benché ciò non infici la capacità dei modelli di inferire correttamente il valore della frazione in massa del BH. La massa totale vera del sistema $\mathrm{M_{\star,true}} = 10^6\,\mathrm{M_\odot}$ cade entro 1σ nel caso di $N \simeq 10^4$, mentre è al massimo entro 2σ per i mock aventi $N \simeq 10^3$. Possiamo quindi asserire che, per un sistema di massa sconosciuta, il valore reale di $\mathrm{M_\star}$ cada entro 1σ se $N \simeq 10^4$ o entro 2σ se $N \simeq 10^3$. Conseguentemente, i risultati ottenuti per le masse totali dei mock sono i seguenti: se $N \simeq 10^4$, $\log(\mathrm{M_\star/M_\odot}) = 6.002^{+0.003}_{-0.003}$ quando $\mu_{\rm BH,true} = 0.01$ e $\log(\mathrm{M_\star/M_\odot}) = 6.000^{+0.005}_{-0.005}$ quando $\mu_{\rm BH,true} = 0.001$; se $N \simeq 10^3$, $\log(\mathrm{M_\star/M_\odot}) = 6.03^{+0.0083}_{-0.008}$ quando $\mu_{\rm BH,true} = 0.01$ e $\log(\mathrm{M_\star/M_\odot}) = 5.955^{+0.050}_{-0.055}$ quando $\mu_{\rm BH,true} = 0.001$.

Prima di procedere con l'applicazione del metodo sviluppato in questa Tesi a GCs reali, nel prossimo futuro pianifichiamo di effettuare un confronto più dettagliato tra i modelli e i dati (per esempio includendo le misure individuali e/o i moti propri delle stelle), il che dovrebbe significativamente migliorare la nostra abilità di inferire la massa dell'IMBH.

Chapter 1

Globular clusters and intermediate mass black holes

The aim of this Thesis is to test the ability of a new family of dynamical models based on analytic distribution functions depending on the action integrals to infer the presence of intermediate mass black holes (IMBHs) in globular clusters (GCs). In this Chapter we give a brief introduction to GCs and IMBHs.

In Section 1.1 we focus on the general properties and dynamical processes that characterize GCs (Sections 1.1.1, 1.1.2 and 1.1.3), together with the observational techniques typically used to study them (Section 1.1.4). Section 1.2 is dedicated to IMBHs, we explain the reasons why we may expect to find IMBHs in the center of GCs, we discuss how they influence the main dynamical and structural properties of a GC (Section 1.2.1), we present other phenomena mimicing the effects of an IMBH (Section 1.2.2) and some of the latest results regarding their putative presence in GCs (Section 1.2.3).

1.1 Globular clusters

1.1.1 Stellar populations

Globular clusters (GCs) are nearly spherical stellar systems, with masses $\sim 10^4 - 10^6\,\mathrm{M}_\odot$, generally populated by $\sim 10^4 - 10^6$ stars with intermediate to old ages. They do not contain significant amounts of gas, dust or dark matter, and their typical luminosity ranges from $\sim 10^4$ to $\sim 10^6\,L_\odot$(Binney & Merrifield, 1998). Our Galaxy hosts about 150 GCs, while M31 about 460 (Barmby & Huchra, 2001), and the analysis of their main-sequence turn-off shows ages typically between 10 and 13 Gyr (see Figure 1.2, Section 1.1.4 and Carroll & Ostlie 1996). As an example of GC, in Figure 1.1 we show an image of 47 Tucanae.

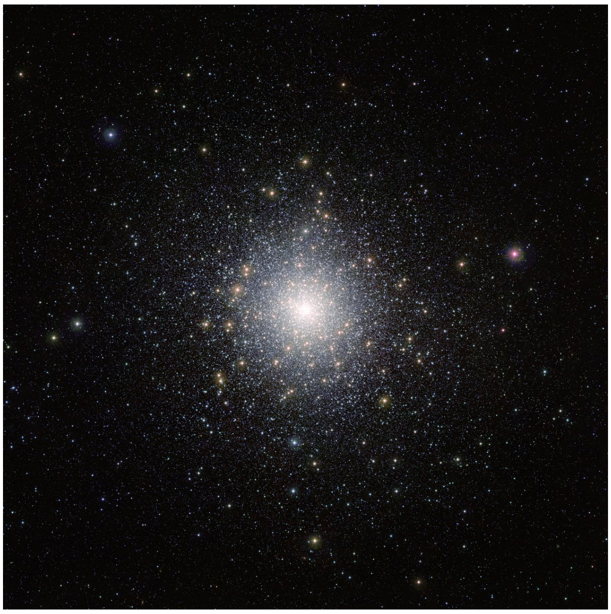

Figure 1.1: Image of the GC 47 Tucanae, taken by the ESO telescope VISTA (Visible and Infrared Survey Telescope for Astronomy). Credits: ESO/M.-R. Cioni/VISTA Magellanic Cloud survey. Acknowledgments: Cambridge Astronomical Survey Unit.

Given that the stars of a GC have similiar metallicity as well as similar age, its stellar population can be approximately modelled as a simple stellar population (SSP), i.e. a single generation of stars formed simultaneously in a burst of star formation. SSP models require three main components: a set of isochrones, a stellar library and an assumption about the stellar initial mass function (IMF). Isochrones predict the evolution of the color-magnitude diagram (CMD), i.e. the flux of each star in a chosen photometric filter as a function of the color index (see Section 1.1.4), of a coeval stellar population on the basis of ages, chemical compositions and masses of the stars, predicting their effective surface gravity, temperature and luminosity. The isochrones are then populated with stars on the basis of the adopted IMF, which determines the fraction of stars with a given mass. The stellar libraries quantify the spectra of stars given their age and metallicity. However, there is today much evidence that some GCs are more consistent with multiple stellar populations, that are combinations of SSP with different ages (Bastian & Lardo, 2018). In Figure 1.2 we show the CMD of the

GC M13, in which all the main evolutionary stages populated in a typical CMD are shown, including the main-sequence turn-off.

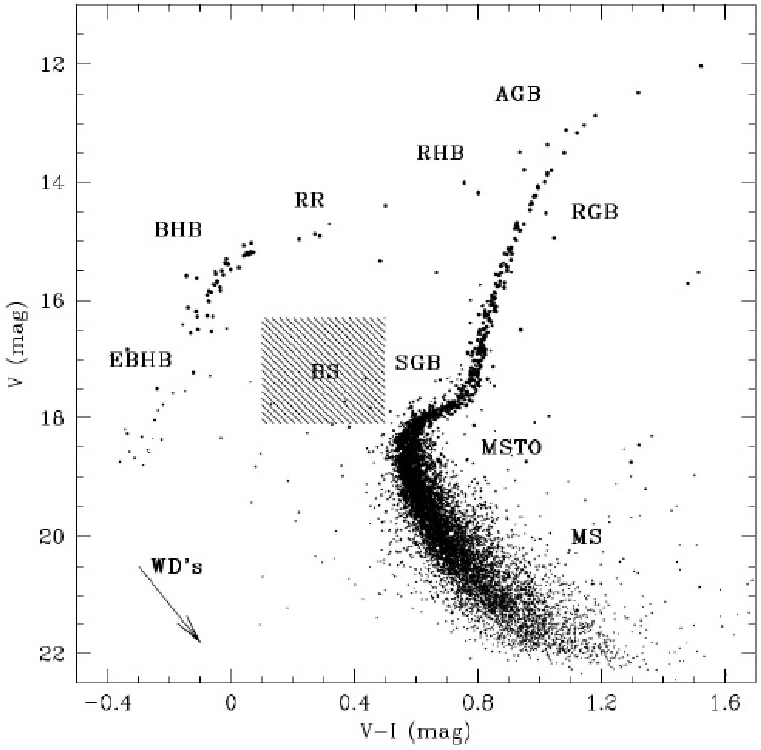

Figure 1.2: I: colour-magnitude diagram (CMD) of the Milky Way GC M13. The main features of the CMD are indicated: main-sequence (MS), main-sequence turn-off (MSTO), subgiant branch (SGB), red giant branch (RGB), asymptotic giant branch (AGB), red-side horizontal branch (RHB), RR Lyrae variables (RR), blue horizontal branch (BHB), extreme blue horizontal branch (EBHB), blue stragglers (BS) and white dwarfs (WDs). Figure from Beasley (2020).

Typically, the GCs considered as metal-rich have abundances $Z \sim 1/3 - 1/10\, Z_{\odot}$, where $Z_{\odot}$ is the solar metallicity, while the metal-poor clusters have abundances $Z \sim 1/300\, Z_{\odot}$ (Sparke & Gallagher, 2007). The metallicity of GCs seems to correlate with their spatial and orbital distribution in the Milky Way (hereafter MW; Zinn 1985). As shown in Figure 1.3, the system of GCs having $[\mathrm{Fe/H}] \lesssim -1$ (80% of all the GCs of the MW) tends to populate the Galactic stellar halo with a spherical distribution, has no net rotation and is dominated by eccentric orbits. The system of metal-rich GCs with $[\mathrm{Fe/H}] \gtrsim -1$ consists of a flattened, highly rotating distribution of GCs (20% of all the Galactic GCs) orbiting near the disk and the bulge of the MW. The mean metallicities of these two populations are $\langle[\mathrm{Fe/H}]\rangle \simeq -1.6$ and $\langle[\mathrm{Fe/H}]\rangle \simeq -0.6$, respectively (Meylan & Heggie 1997). Also local dwarf satellites of the MW, such as the Magellanic Clouds and Fornax, are known to host GCs.

Since the metallicity is almost the same for all the stars belonging to a GC, it is thought that GCs experienced a fast star formation in the early phases of the cosmic history, in which they formed the bulk of their stellar mass (Binney & Tremaine, 2008). Afterwards, supernovae (mostly type II) feedback caused by the first stellar population quenched the star formation ejecting the gas out of the system, whose gravitational attraction was insufficient to retain it, and avoiding the formation of new stars.

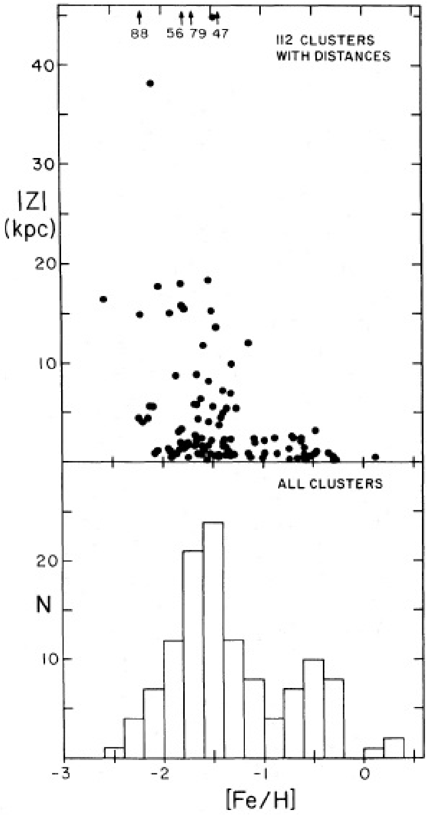

Figure 1.3: Top panel: the altitude above the disk plane $|Z|$ as a function of the metallicity [Fe/H] of 112 Galactic GCs of known heliocentric distance. Notice that there are no clusters within 20 kpc$< |Z| <$ 37 kpc and that the $|Z|$ distribution changes suddenly at [Fe/H] ~ 1. The bottom panel is a histogram of the metallicity distribution considering the 112 GC of the top panel, showing the bimodal distributions in both the Galactic altitude and the metallicity distributions. Figure from Zinn (1985).

1.1.2 Structural and dynamical properties of GCs

GCs appear almost circularly symmetric, with an average axis ratio of $q = 0.93 \pm 0.01$[1] (White & Shawl, 1987). GCs are supported against gravity mainly by the disordered kinetic energy of their stars, as it is inferred by measurements of their line-of-sight velocity dispersions (Tabel 1.1). They also may have net rotation. To make an example, ω Centauri, a cluster located approximately 5 kpc away from the Sun in the direction of the bulge, has an axial ratio $q = 0.78 \pm 0.03$ and an average rotation speed of $V_{\rm rot} \sim 8$ km/s (van de Ven et al., 2006). Another example is NGC 6388, which is almost spherical ($q = 0.99$; Harris 1996) but rotates at a speed $V_{\rm rot} \simeq 8.5$ km/s in the inner regions, and at $V_{\rm rot} \simeq 3$ km/s in the outer regions (Lanzoni et al., 2013).

As we will discuss in the next Chapter, GCs have relaxation times larger than their ages. This means that the internal dynamics of a GC evolves on relatively short timescales.

---

[1] The axis ratio q is defined as the semi-minor to semi-major axes ratio.

Cluster		d (kpc)	[Fe/H]	M_V (*mag*)	r_c (pc)	r_t (pc)	$\sigma_{\rm los}$ (km/s)
NGC 5139	ω Cen	5.2	−1.6	−10.2	4	70	20
NGC 104	47 Tuc	4.5	−0.71	−9.5	0.5	50	11
NGC 7078	M15	10.8	−2.15	−9.3	< 0.01	85	12
NGC 6341	M92	8.5	−2.15	−8.3	0.5	35	5
NGC 7099	M30	9.1	−2.13	−7.6	< 0.1	45	5
NGC 6121	M4	1.73	−1.2	−7.2	0.5	25	4
	Pal 13	24.3	−1.9	−3.8	0.5	> 50	0.6 − 0.9
NGC 1049	Fornax 3	140	−2	−7.8	1.6	> 50	9

Table 1.1: A list of GCs of the Milky Way, and one of the Fornax dSph (Sparke & Gallagher, 2007). From the left-hand to the right-hand column: name of the GC (Cluster), heliocentric distance (d), iron abundance ([Fe/H]), absolute magnitude in V band (M_V), core radius (r_c, see Section 1.1.2), truncation radius (r_t, see Section 1.1.2), line-of-sight velocity dispersion (σ_r, equation 2.2.21).

In such conditions, the interactions between the stars of a GC are very efficient and trigger processes that will eventually modify the kinematics and structure of GCs.

At first the system develops an isotropic velocity distribution (see Section 2.2.4) that tends to the Maxwellian distribution

$$f(v)\,\mathrm{d}v = 4\pi \left(\frac{1}{2\pi\sigma^2}\right)^{3/2} v^2 e^{-\frac{v^2}{2\sigma^2}}\mathrm{d}v, \tag{1.1.1}$$

where σ^2 is the velocity dispersion. A spherical system with position-independent velocity dispersion is known as **isothermal sphere** (Binney & Tremaine, 2008). The density distribution of the isothermal sphere, which does not have analytic expression, is almost flat within the so-called core radius $r_c = [9K/(4\pi G\rho_c)]^{1/2}$, where ρ_c is the central stellar density of the GC and K is a characteristic gravitational potential scale. Typically, $r_c \simeq 5$ pc for GCs. The isothermal sphere has infinite mass. A simple analytic model often used to approximately describe the density distribution of the isothermal sphere is the **modified Hubble profile** (Binney & Tremaine, 2008)

$$\rho(r) = \frac{\rho_0}{\left[1 + \left(\frac{r}{r_0}\right)^2\right]^{3/2}}, \tag{1.1.2}$$

where r_0 and ρ_0 are a characteristic scale radius and a reference density, respectively. In GCs, $r_0 \simeq r_c$. About the $80 - 85\%$ of the actually discovered GCs are well described by such profile (Djorgovski & King, 1986). However, GCs with an infinite mass are unrealistic: they are not isolated systems, and they orbit within the gravitational field of their host galaxy (e.g. the MW), which, over long timescales, strips the GC outermosts, less bound stars. That is why equation 1.1.2 is often modified by the introduction of the so-called truncation (or tidal) radius r_t. For radii larger than r_t, the density profile drops to zero more steeply than in equation 1.1.2 and the mass becomes finite. The typical value of GCs truncation radii is $r_t \approx 30$ pc.

In addition to the core radius, it is useful to define the half-light radius, that is the radius of the sphere containing half of the system total luminosity. To make a comparison, dwarf spheroidal galaxies (dSphs) have a typical half-light radius ~ 300 pc, while the typical half-light radius of a GC is of the same order of magnitude of the core radius (Binney & Tremaine, 2008). Since the luminosities of GCs and dSphs are similar, GCs have a much higher average surface brightness. The central density of GCs is extremely high, about $10^4\,\mathrm{M}_\odot/\mathrm{pc}^3$ (in the solar neighbourhood it is about $0.5\,\mathrm{M}_\odot/\mathrm{pc}^3$). Indeed, in Figure 1.4 we show the central surface brightness in V band against the absolute magnitude in V band of the most common stellar systems. Despite their low luminosity, the central surface brightness of GCs is of the same order of magnitude of that of early-type galaxies.

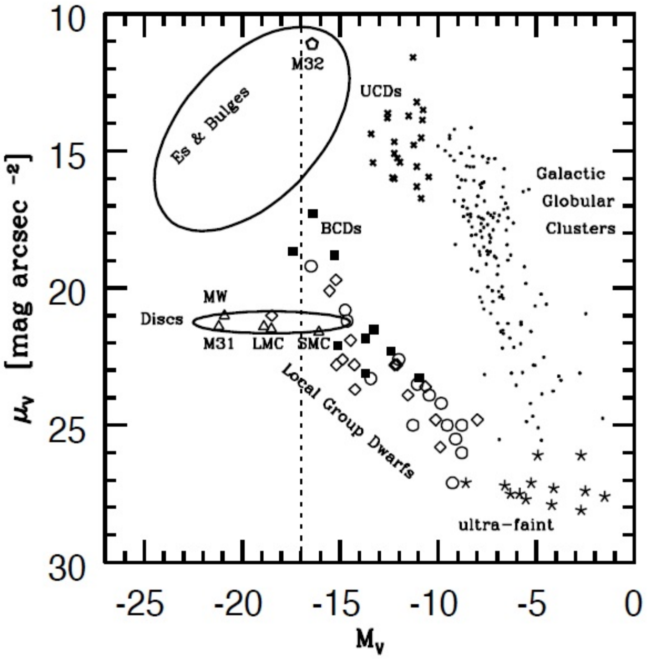

Figure 1.4: Central surface brightness in V band against the absolute magnitude in V band of many stellar systems. Figure by Cimatti, Fraternali & Nipoti (2019).

1.1.3 Dynamical evolution of GCs

In a system with a Maxwellian velocity distribution (equation 1.1.1), the energy is equally distributed among all the particles, by means of a process called **energy equipartition** (Meylan & Heggie, 1997). As all the stars of such a system tend to have the same kinetic energy,

$$m_i\overline{v_i^2} = m_j\overline{v_j^2}, \tag{1.1.3}$$

where $m_{i/j}$ and $\overline{v_{i/j}^2}$ are the mass and the mean squared velocity of the i/j-th star. In the case of a system with stars of different masses, if for instance $m_i > m_j$, the above equation implies

$$\overline{v_i^2} < \overline{v_j^2}. \tag{1.1.4}$$

Therefore, as the system tends to the equilibrium, massive stars slow down and migrate towards the center of the system, while lighter stars increase their velocities moving at larger distances.

Due to energy equipartition, it is possible that, among the low mass stars, some of them gain a velocity exceeding the system escape velocity $v_{\rm esc} = \sqrt{2\Phi_\star(\mathbf{x})}$, where $\Phi_\star(\mathbf{x})$ is the gravitational potential. On sufficiently long timescales, these stars will eventually be expelled from the GC. The more the GC loses stars, the more it contracts due to the loss of kinetic energy. Assuming that the systems remains close to equilibrium, the Virial theorem implies

$$K = \frac{|W|}{2}, \tag{1.1.5}$$

where K is the kinetic energy of the system and W the potential energy. The total energy of the system $E = K + W = K - |W|$ is conserved. Let E_i, K_i and W_i be the GC initial total, kinetic and potential energies, respectively. The loss of a fraction of kinetic energy $\mathrm{d}K = -|\mathrm{d}K| < 0$ leads the system off equilibrium and to a decrease of the final energy $E_f = E_i + \mathrm{d}E = E_i - |\mathrm{d}K| < E_i$. When the GC recovers equilibrium, then the virial theorem will apply to the the final configuration as well, leading to

$$\begin{cases} E_f = K_i + \mathrm{d}K - |W_i| = K_f - |W_f|, \\ K_f = \frac{|W_f|}{2}. \end{cases} \tag{1.1.6}$$

The first equation in 1.1.6 can be rewritten as

$$W_f = W_i - 2|\mathrm{d}K| < W_i, \tag{1.1.7}$$

or

$$K_f = K_i + |\mathrm{d}K| > K_i. \tag{1.1.8}$$

In conclusion, losing energy makes the system more bound, as its potential energy becomes more negative by $2\,|\mathrm{d}K|$. On the contrary, its final kinetic energy is higher by an amount $|\mathrm{d}K|$. This prosess is called **gravothermal catastrophe**: the more the GC loses energy, the more it contracts. The more it contracts, the more it loses energy, in a runaway process that can eventually dissolve the GC (evaporation).

As GCs are populated by stars of different masses, another process that drives their dynamical evolution is the **dynamical friction** (Chandrasekhar, 1943). A massive star with mass m_t and velocity v_t is decelerated by lighter stars with mass m and it sinks towards the center of the system. The process occurs over a timescale (Alessandrini et al., 2014)

$$t_{\rm DF}(r) = \frac{v_t^3(r)}{4\pi G^2 n(r)\, m(m+m_t)\phi(v_t)\ln\Lambda}, \tag{1.1.9}$$

where $n(r)$ is the number density of the lighter particles, $\phi(r)$ is the fraction of stars slower than v_t and $\ln\Lambda$ is the Coulomb logarithm (for details, see equation 2.1.7). Equation 1.1.9 depends on n^{-1}, thus dynamical friction is more efficient in the core of the GC rather than in the outskirts. Also, the higher m_t, the more efficient the dynamical friction. This is why black holes and neutron stars are expected to be in the innermost regions of GCs, being the remnants of stars with masses $M \gtrsim 8\,\mathrm{M}_\odot$, which are likely to sink quickly towards the center of the GC.

Dynamical friction drives the **mass segregation** (Meylan & Heggie, 1997). Massive stars sink towards the center of the system faster than less massive stars, causing an increase in the relative fraction of massive stars in the center. Mass segregation is an important proxy of the dynamical state of the system: if the dynamical friction had enough time to act, then the GC will be more mass segregated and dynamically evolved. Notice that mass segregation is different from energy equipartition: a system formed by stars of identical mass, for example, cannot segregate mass, but can reach the thermal equilibrium in any case. As more massive stars lose more and more kinetic energy in favour of lighter stars, the core becomes denser, with a steepening in the inner regions of the density profile ($\rho \propto r^{-1} - r^{-0.8}$ for $r \to 0$) (Meylan & Heggie, 1997). GCs with such profiles are called **core collapsed**. The core collapse can, theoretically, cause a singularity in the density profile. Today it is thought that this runaway process is quenched by hard binary systems through **three-body encounters**. A three-body encounter occurs when a single external star approaches close enough to a a binary system to exchange energy with it. Depending on the orbital parameters of the encounter (Heggie, 1975):

1. the binary shrinks, losing energy in favour of the external star, which gains recoil velocity;
2. the binary expands, taking energy from the external star, which loses kinetic energy;
3. if the external star is more massive than one of the stars of the binary system, it can take its place, increasing the binding energy of the binary;
4. if the external star speed is high enough, the binary can be ionized (the two stars of the binary become unbound).

For instance, simulations by Gao et al. (1991) showed that when a binary encounters a single star, it can use its binding energy to kick the external star outward, quenching core collapse. Moreover, simulations show also that the core of a GC can undergo several contractions and expansions: this process is called **gravothermal oscillation**. Finally, note that massive stars sink over eccentric orbits, which causes the radial velocity dispersion σ_r to increase (see Section 2.2.4) and the velocity distribution of the stars to become radially biased.

The last process we briefly examine is called **Spitzer instability**. According to Spitzer (1969), in a two-component system formed with heavy and light stars of masses m_1 and m_2, respectively, equipartition is possible only if the mass fraction in heavy particles is smaller than a critical value: $M_2/M_1 \lesssim 0.16(m_1/m_2)^{3/2}$, where M_1 and M_2 are the total masses in stars of mass m_1 and m_2, respectively. If the total mass of heavy stars is high enough with respect of that of light stars, energy equipartition is not possible, and the high-mass stars form a sub-cluster dynamically decoupled from the low-mass stars. This sub-cluster continues to contract until all the massive stars eject each other or collapse into single object. This last scenario can be a formation path for **intermediate mass balck holes** (IMBHs), even though which of the two process (ejection or collapse) dominates is still an open question. Holley-Bockelmann et al. (2008) and Fragione, Ginsburg & Kocsis (2018) showed through simulations and semi-analytic models that the gravitational waves emission by black-hole (BH) binaries cause the resulting IMBHs to be ejected in most cases. On the contrary, Breen & Heggie (2013) obtained opposite results, with a high probability for GCs to retain their IMBHs.

1.1.4 Photometric and spectroscopic observations of GCs

We can divide the observables that can be obtained from GCs in two categories: photometric and spectroscopic. While photometry provides the integrated emission of the stars of the GC in a specific band, spectroscopy provides spectra, i.e. the flux as a function of the wavelength of the radiation emitted by the target.

From photometry it is possible to collect information (for example position and flux) of a large number of stars at once, when the system is resolved. Also, comparing observations taken for the same target at different times, it is possible to obtain the proper motions of stars (hereafter PMs, i.e. the target angular velocity on the plane of the sky). Considering the average distance of GCs ($\approx$ 10 kpc), PMs of GC stars can be obtained with a baseline between two observations longer than 2 years (van der Marel & Anderson, 2010). Furthermore, having observations of resolved stars of the same target in at least two different photometric filters allows one to build the CMD of the observed stars (Section 1.1.1). CMDs are essential to obtain metallicity and age of the GC stellar populations. If the stars are too crowded to be resolved, photometry is not able to provide star fluxes and positions, thus neither PMs and CMDs. An issue related to photometric observations is the saturation of the pixels of a CCD, which occurs when the number of photons hitting a pixel is too high. Saturation usually occurs when observing bright stars for long exposure times. In conclusion, it is necessary to tune the integration time in order to be able to resolve as many stars as possible or, alternatively, take many different images with different exposure times.

In case of resolved stellar populations as in a local GC, the spectra can provide for each star the spectral class, the metallicity, and the line-of-sight velocity from the shift of the lines with respect of the expected wavelength, as a consequence of Doppler effect. In the case of spectra of unresolved regions of the GC, the information is integrated along the line of sight, therefore it is possible to obtain the average spectral class and metallicity of the stars of that region, together with the rotation velocity and the line-of-sight velocity dispersion of the system at that point (equation 2.2.25 and 2.2.27). When doing spectroscopic observations of regions of the GC in which it is impossible to resolve stars, few bright stars can dominate the emissin from that location (**shot noise bias**; Lützgendorf et al. 2011a; Lanzoni et al. 2013; Lützgendorf et al. 2015). The bright stars overcome faint stars, and the broadening of the lines of the resulting spectrum is not a reliable measure of the line-of-sight velocity dispersion.

An issue arising with both spectroscopy and photometry is the necessity to remove field stars from the sample. In the case of GCs one can exploit that all the stars of a GC have similar metallicity (Section 1.1.1). Thus, stars having line-of-sight velocities or metallicities way too large than those expected from the systemic velocity or the average metallicity of that GC are usually rejected (Lanzoni et al., 2013).

1.2 Intermediate mass black holes

IMBHs are usually defined as black holes with masses in the range between $100\,\mathrm{M}_\odot$ and $10^5\,\mathrm{M}_\odot$ (Greene, Strader & Ho, 2019). We have observational compelling evidence of BHs with masses lower than $100\,\mathrm{M}_\odot$, which are called stellar BHs, and with masses higher than $10^5\,\mathrm{M}_\odot$, the so-called supermassive black holes (SMBHs). IMBHs are the natural link between stellar and supermassive BHs, for which, however, there is essentially no substantial evidence. The least massive stellar BHs are remnants of supernovae explosions caused by stars with masses higher than $8\,\mathrm{M}_\odot$ at the end of their life. Instead, it is believed that the most massive stellar BHs are formed via merging of the least massive ones in high density environments. They have been detected in our Galaxy by means of micro-quasar emission and, in the last few years, by gravitational waves emission produced by binary systems made of two BHs or by a BH and a neutron star. There is evidence that SMBHs are the engines of Active Galactic Nuclei (AGN) and that they reside at the center of the great majority of the galaxies in the Universe (in general in elliptical galaxies or in bulges of spirals). The most direct evidence for the existence of a SMBH has been recently provided by the Event Horizon Telescope Collaboration (Event Horizon Telescope Collaboration et al., 2019), which was able to get the image of the radio emission of the gas in the innermost stable orbit of the SMBH of M87 (measuring a BH mass $\sim 6.5\times10^9\,\mathrm{M}_\odot$), by means of a huge interferometric web of radiotelescopes. The extremely high masses of SMBHs seem to be the result of the accretion of gas, stars and other BHs, started during the early phases of the Universe.

The mass of the central SMBH M_BH is found to correlate with the stellar mass of the bulge of the host galaxy (Magorrian et al., 1998). Similar relations are found between M_BH and the stellar mass or stellar velocity of the host galaxy in the form

$$\log \mathrm{M}_\mathrm{BH} = \alpha + \beta \log\left(\frac{x}{x_0}\right), \tag{1.2.1}$$

where α and β are the intercept and slope of the relation, respectively, while x can be both the stellar mass of the host galaxy M_* or the line-of-sight velocity dispersion of its stars $\sigma_\star$, with x_0 a reference value. Greene, Strader & Ho (2019) provide

$$\begin{aligned}\log \mathrm{M}_\mathrm{BH} &= (7.87\pm0.06) + (1.25\pm0.23)\log\left(\frac{\sigma_\star}{160\,\mathrm{km/s}}\right),\\ \log \mathrm{M}_\mathrm{BH} &= (7.45\pm0.09) + (1.61\pm0.12)\log\left(\frac{\mathrm{M}_\star}{3\cdot10^{10}\,\mathrm{M}_\odot}\right),\end{aligned} \tag{1.2.2}$$

The above relations have been calibrated using a sample of SMBHs of both early-type and late-type galaxies from previous works (see Greene, Strader & Ho 2019 and references therein). In particular, as shown in Figure 1.5, the relationship $\mathrm{M}_\mathrm{BH} - \mathrm{M}_\star$ for late-type galaxies has a comparable slope, but lower normalization, than the same relationship for early-type galaxies. Extrapolating the relationship to the typical velocity dispersions of GCs ($\approx 10-30$ km/s), the expected mass for a BH in the center of a GC is in the range $10^2 - 10^4\,\mathrm{M}_\odot$. Thus, it is reasonable to think that GCs are good candidates to host IMBHs.

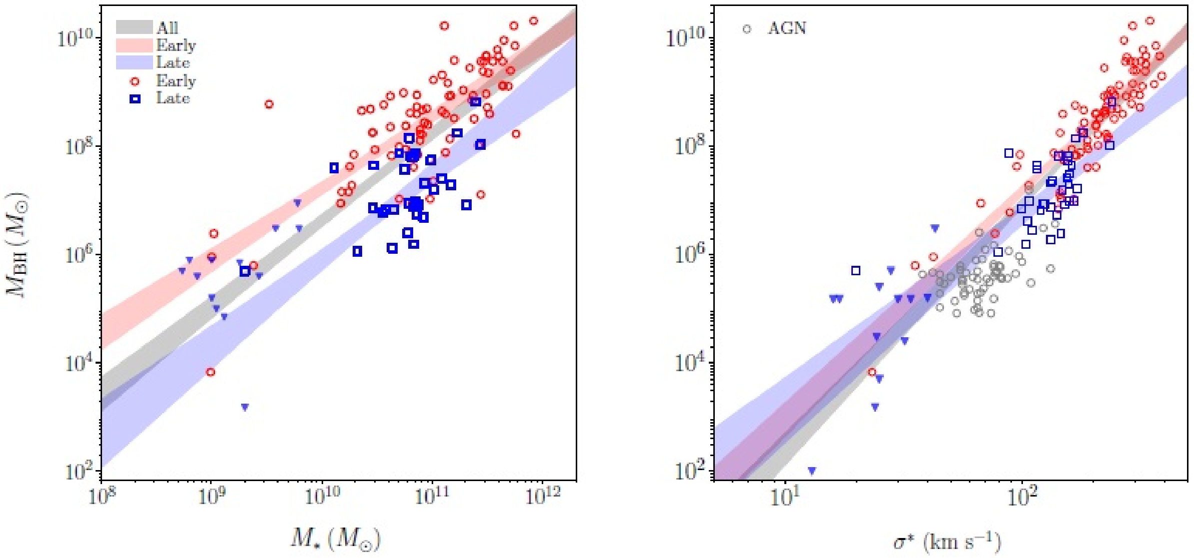

Figure 1.5: Left panel: relationship between the mass of the BH $\mathrm{M_{BH}}$ and the stellar mass of the host system M_* for early-type (red circles), late-type (blue squares), and upper limits (blue triangles). The red, blue and grey band correspond to the fit of equation 1.2.2 considering early-type galaxies, late-type galaxies and the full sample, respectively. Right panel: same as the left panel, but for $\mathrm{M_{BH}}$ versus σ_*. Here, the sample of AGNs from Xiao et al. 2011 (grey dots) is included, too. Figure from Greene, Strader & Ho (2019).

1.2.1 Looking for observational evidences of IMBHs

Since GCs are systems almost free from gas, detecting X-ray activity due to the gas accretion onto the BH should be extremely rare. Nonetheless, some GCs are characterized by the X-ray emission of the so-called Ultra-luminous X-ray sources (ULXs), which may be associated to the emission of gas accreting onto a BH. However, their spectra are inconsistent with those observed for Galactic stellar-mass black holes scaled to the IMBH mass regime. Instead, since they show features consistent with super-Eddington accretion, today it is believed that the emission of ULXs is caused by stellar-mass BHs emitting at a super-Eddington regime (Kaaret, Feng & Roberts, 2017).

A promising method to detect IMBHs is the study of the dynamical effects of IMBH on the stars in the innermost region of a GC, where the gravitational field of the IMBH is stronger than the one generated by the local stars. The observation of extremely high-velocity stars can be associated to the kick of a binary system including an IMBH, as described in 1.1.3. Other possible signatures of a central IMBH, in GCs, are a steep central line-of-sight stellar velocity dispersion profile (Noyola et al., 2010; van der Marel & Anderson, 2010; Pascale et al., 2019) and a mild cusp in the central stellar projected density profile $\Sigma_\star(R)$, with $\gamma \equiv \mathrm{d}\log\Sigma_\star/\mathrm{d}\log R \in [-0.2, -0.3]$ (Lanzoni et al., 2007). Moreover, observing quenched mass segregation and core collapse may be a proxy of the presence of a binary system including an IMBH (Section 1.1.3).

All these features can be detected only if the resolution of the instruments used to observe GCs is sufficiently high to probe the regions of the GC in which the gravity of the IMBH dominates. The extent of this region is measured by means of the so-called radius of influence of the IMBH $R_{\rm infl}$ (Binney & Tremaine, 2008), such that

$$\sigma_{\rm los}(R_{\rm infl}) = \left(\frac{G\mathrm{M_{BH}}}{R_{\rm infl}}\right)^{1/2}, \tag{1.2.3}$$

where $\sigma_{\rm los}(R_{\rm infl})$ is the stellar line-of-sight velocity dispersion at the radius of influence, G is the gravitational constant and $\mathrm{M_{BH}}$ is the mass of the BH. Alternatively, Greene, Strader & Ho (2019) adopted the different formula

$$R_{\rm infl}(\mathrm{pc}) \approx 0.0043\,(\mathrm{M_{BH}}/\mathrm{M_\odot})(\sigma_{\rm los}/\mathrm{km\,s^{-1}})^{-2}, \tag{1.2.4}$$

where $\sigma_{\rm los}$ is the typical line-of-sight velocity dispersion of the GC. Assuming as typical GCs line-of-sight velocity dispersion $\sigma_{\rm los} \approx 15$ km/s and given an expected IMBH mass $\mathrm{M_{BH}} \approx 10^3\,\mathrm{M_\odot}$, equation 1.2.4 provides an expected radius of influence $R_{\rm infl} \simeq 0.02$ pc. Taking for instance the reference distance of 7 kpc, $R_{\rm infl}$ corresponds to an angular size of $\theta_{\rm infl} \approx 0.6''$, which is at the limit of the angular resolution for the current instruments. Moreover, the central regions of GCs are extremely crowded, which makes it very difficult to resolve single stars in these regions. Thus, observing within the sphere of influence of an IMBH in a GC is complicated and it requires high-quality spectroscopy and resolved photometry. Also, even if a good sample of data is available, many phenomena can mimic the typical effects of an IMBH, as we shall discuss in the following Section.

1.2.2 Constraining the masses of IMBHs in GCs

The dynamical fingerprints that an IMBH leaves on the stars at the center of a GC is degenerate with a large number of effects.

At first **mass-anisotropy degeneracy**. A high central line-of-sight velocity dispersion can be due to radial anisotropy in the central velocity distribution as well as by a central IMBH. An example is the study of the putative SMBH in the center of the galaxy M87. Sargent et al. (1978) found out evidence of the existence of such SMBH assuming an isotropic velocity distribution, while Binney & Mamon (1982) showed that assuming a reasonable radially biased velocity distribution made the SMBH unnecessary. To break the mass-anisotropy degeneracy in resolved stellar populations, including PMs in the analysis may become essential, as the three-dimensional information on the velocity becomes available, so that the anisotropy is uniquely determined.

In Section 1.1.3 we showed how dynamical friction and energy equipartition cause high-mass stars to sink towards the center of the GC. Since the stellar luminosity of main-sequence stars are approximately related to the stellar mass by the non linear law $L \propto M^3$ (Salaris & Cassisi, 2005), high-mass stars have a higher mass-to-light ratio M/L than lighter stars. This is still true also when considering that the higher the mass of the star, the faster its evolution and the reaching of the red giant evolutionary stage, that further increases the luminosity of the star. As a consequence, the mass-to-light ratio is likely not to be constant throughout a GC and it is generally expected to be lower in its central parts. This effect should be taken into account when converting a surface brightness profile into a projected density profile, since a cusp in the surface brightess profile does not imply a cusp in the projected density profile. In principle, the inner slope in the surface brightness profiles caused by mass segregation is higher than the one expected for a IMBH (see Section 1.2.1). However, during the pre-collapse phase the surface brightness slope is flatter, and closer to the typical values caused by IMBHs (Vesperini & Trenti, 2010). Furthermore, a high fraction of binaries ($f_{\rm bin} \gtrsim 3\%$) may quench mass segregation so that the slope is kept lower than expected in the absence of binaries.

Also, IMBHs are not the only possible sources of high-speed stars and mass segregation quenching. Binary systems of stellar-mass BHs or neutron stars can mimic both these effects, as explained in Section 1.1.3 (Trenti, Vesperini & Pasquato, 2010), while high-speed stars can also be field stars in projection in the center of a GC.

The correct evaluation of the position of the center of the GC is essential to properly build the projected density and line-of-sight velocity dispersion profile. Indeed, misidentifying of the center of the system of even $0.2'' - 0.3''$ leads to wrong inferences on the presence and mass of the IMBH (Noyola et al., 2010; Anderson & van der Marel, 2010). The center can be calculated by means of many techniques, for example as the average center of the isophotes (i.e. curves of constant surface brightness) of the image, or as the point at which the denisty distribution is the most symmetric (Anderson & van der Marel, 2010).

Finally, a cluster of stellar-mass remnants (stellar-mass BHs and neutron stars) may mimic the effect of an IMBH on the projected density an line-of-sight velocity dispersion profiles, at the present available resolution for observations (Mann et al., 2019). Such remnants would sink in the center of the system due to their high masses, without merging in a single object. Such a system could form in the first evolutionary stages of GCs and survive up until now if the relaxation time (Section 2.1) of the host GC is long enough (~ 1 Gyr; Arca Sedda, Askar & Giersz 2018).

1.2.3 Recent results about IMBHs in GCs

Despite the fact that GCs are the perfect candidates to host IMBHs, until today there is no clear evidence of the existence of IMBHs in the center of GCs, mostly due to the aforementioned problems. Some of the most promising candidates are ω Centauri (ω Cen) and NGC 6388 (Greene, Strader & Ho, 2019).

ω Cen is the most luminous and massive Galactic GC ($\sim 10^6$ M$_\odot$), at a distance of $\simeq 5.2$ kpc (Table 1.1), which is thought to be the remnant of a dwarf galaxy tidally disrupted by the tidal field of the MW. Noyola, Gebhardt & Bergmann (2008) and Noyola et al. (2010) found evidence of a central IMBH of mass $\mathrm{M_{BH}} \sim 3 - 5.2 \times 10^4$ M$_\odot$ (depending on the choice of the center of ω Cen) from line-of-sight kinematic data. Jalali et al. (2012) confirmed these results, using N-body simulations of ω Cen to reproduce the same surface brightness and line-of-sight velocity dispersion profiles observed by Noyola, Gebhardt & Bergmann (2008). This seems to be possible only including an IMBH of mass $\mathrm{M_{BH}} \approx 10^4$ M$_\odot$. Anderson & van der Marel (2010) argued that these results were biased by a wrong evaluation of the center of the GC. Including also proper motions of $\sim 10^5$ stars (53382 within $2''$) and evaluating a new position of the center of ω Cen, in their analysis they found no statistical evidence of an IMBH, putting an upper limit to the BH mass of $\sim 1.4 \times 10^4\ \mathrm{M}_\odot$. More recently, Baumgardt (2017) obtained evidence of the presence of an IMBH of $\sim 4 \times 10^4\ \mathrm{M}_\odot$ in the center of the GC ω Centauri from projected density and line-of-sight velocity dispersion profiles. However, a model with no IMBH is preferable when PMs are considered (Baumgardt et al., 2019).

Also the presence of a putative IMBH in NGC 6388 has been highly debated: Lützgendorf et al. (2011b) and Lützgendorf et al. (2015) found kinematic signatures of an IMBH of mass $\mathrm{M}_{\mathrm{BH}} = (2.8 \pm 0.4) \times 10^4\,\mathrm{M}_\odot$ by means of light-integrated spectroscopy. Lanzoni et al. (2013) questioned these results, arguing that light-integrated spectroscopic data can be biased by a few bright stars (i.e. shot noise bias, see Section 1.1.4). Using resolved-star spectroscopy, they found no statistical evidence for IMBH, putting an upper limit to the BH mass of $\sim 2000\,\mathrm{M}_\odot$.

For what concerns different detection approaches, the study of emissions by ULXs in GCs provided only upper limits to the masses of putative IMBHs (Tremou et al., 2018), while the emission of gravitational waves by BHs merging in IMBHs has been detected in the late few years. As an example, we cite the recent result by The LIGO Scientific Collaboration et al. (2020), who detected a merging of 2 BHs forming an IMBH having mass $\mathrm{M}_{\mathrm{BH}} = 142^{+28}_{-16}\,\mathrm{M}_\odot$.

Chapter 2

Dynamical models of GCs with IMBHs

A GC with negligible interactions with other nearby stellar systems, for example tidal stripping due to the MW, can be considered in an equilibrium state. Also, over timescales comparable with the GC relaxation time, the N stars in the system can be approximated as a smooth density distribution and gravitational field, and we will call the system collisionless. In Section 2.1 we introduce the concept of relaxation time and discuss the limits of applicability of collisionless models to GCs. In Section 2.2 we focus on the theory of distribution functions for collisionless systems (Sections 2.2.1, 2.2.2 and 2.2.3) and expose the properties of some of the most used distribution functions to model GCs (Sections 2.2.4 and 2.2.5). After a brief introduction on action-angle formalism (Section 2.3.1), in Section 2.3 we focus on action-based distribution functions (Section 2.3.2), exploring their peculiarities and introducing the distribution function depending on action that we will adopt to model GCs throughout this Thesis (Sections 2.3.3 and 2.3.4).

2.1 The relaxation time

Let us consider a stellar system of N stars of mass m. We try to assess the importance of the granularity of the system by studying the motion of a **subject star**, travelling through the system, as it encounters the other **field stars**, assumed to be uniformly distributed within a characteristic radius R. We say that the collisionless approximation holds as long as the total energy of the subject star does not change significantly as a consequence of two-body encounters. The timescale over which such energy changes, and thus the system cannot be considered as collisionless, is called two-body relaxation time ($t_{\rm relax}$). Following the treatment of Binney & Tremaine (2008), in this Section we provide an analytic expression for $t_{\rm relax}$ given a system of N particles.

We assume that the subject star passes through a stationary distribution of field stars with a velocity $\mathbf{v}$ and we calculate the velocity variation $\delta\mathbf{v}$ due to an encounter with one of the field star, with position vector $\mathbf{r}$ with respect to the subject star. In this model $\delta\mathbf{v} \perp \mathbf{v}$, since the acceleration parallel to $\mathbf{v}$ averages to zero assuming that the encounter begins when $r \equiv ||\mathbf{r}|| \to -\infty$ and ends when $r \to +\infty$. Called δv and v the magnitudes of the deflection $\delta\mathbf{v}$ and the velocity $\mathbf{v}$, respectively, δv is evaluated assuming: $\delta v/v \ll 1$; a straight-line trajectory for the subject star; a perpendicular force $F_\perp$ exerted by the field star. The assumption of straight-line trajectory breaks down when $\delta v \simeq v$, which occurs for 90° deflection angles and therefore for an impact parameter $b \lesssim b_{\rm min} \equiv 2Gm/v^2$ (see Figure 2.1).

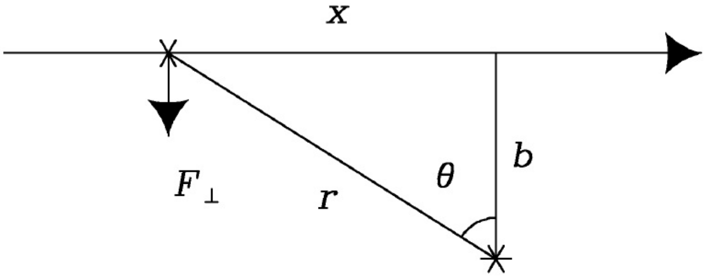

Figure 2.1: The subject star approaches the field star with a distance vector $\mathbf{r}$ and a velocity $\mathbf{v}$. θ is the angle between $\mathbf{r}$ and the direction perpendicular to the trajectory of the subject star, the distance x and the impact parameter b are the projection of $\mathbf{r}$ parallel and perpendicular to the trajectory of the subject star, respectively. Image taken from Binney & Tremaine (2008).

In the notation of Figure 2.1, we fix $t = 0$ when $x = 0$ and find

$$F_\perp = \frac{Gm^2}{b^2+x^2}\cos\theta = \frac{Gm^2 b}{(b^2+x^2)^{3/2}} = \frac{Gm^2}{b^2}\left[1+\left(\frac{vt}{b}\right)^2\right]^{-3/2}. \tag{2.1.1}$$

By Newton's law

$$m\dot{\mathbf{v}} = \mathbf{F} \qquad \text{so} \qquad \delta v = \frac{1}{m}\int_{-\infty}^{+\infty} dt\, F_\perp, \tag{2.1.2}$$

leading to

$$\delta v = \frac{Gm}{b^2}\int_{-\infty}^{+\infty}\frac{dt}{[1+(vt/b)^2]^{3/2}} = \frac{Gm}{bv}\int_{-\infty}^{+\infty}\frac{ds}{(1+s^2)^{3/2}} = \frac{2Gm}{bv}. \tag{2.1.3}$$

Roughly, δv can be described as the acceleration in $r = b$, exerted for a time duration $2b/v$.

The mean projected number density of such a stellar system can be approximated as of the order $N/(\pi R^2)$, so, when the subject star crosses the stellar system once, it encounters

$$\delta n = \frac{N}{\pi R^2} 2\pi b \, \mathrm{d}b = \frac{2N}{R^2} b \, \mathrm{d}b \tag{2.1.4}$$

stars with impact parameter between b and $b + \mathrm{d}b$. Each of these interactions causes a deflection $\delta \mathbf{v}$ in the velocity of the subject star, but since these small perturbations are randomly oriented, the mean deflection is zero. However, after one crossing, the mean-square variation due to encounters with an impact parameter within the interval $[b, b + \mathrm{d}b]$ is

$$\sum \delta v^2 \simeq \delta v^2 \delta n = \left(\frac{2Gm}{bv} \right)^2 \frac{2N}{R^2} b \, \mathrm{d}b \neq 0. \tag{2.1.5}$$

Integrating equation 2.1.5 over all the impact parameters from b_{min} to b_{max} gives the total mean-square velocity deflection

$$\Delta v^2 \equiv \int_{b_{\mathrm{min}}}^{b_{\mathrm{max}}} \sum \delta v^2 \simeq 8N \left(\frac{Gm}{Rv} \right)^2 \ln \Lambda, \tag{2.1.6}$$

where

$$\ln \Lambda \equiv \ln \left(\frac{b_{\mathrm{max}}}{b_{\mathrm{min}}} \right) \tag{2.1.7}$$

is a factor called the **Coulomb logarithm**. In equations 2.1.6 and 2.1.7 $b_{\mathrm{max}} \simeq R$ in order to keep the assumption of homogeneous field stars distribution valid. Then

$$\ln \Lambda \equiv \ln \left(\frac{R}{b_{\mathrm{min}}} \right), \tag{2.1.8}$$

where $R/b_{\mathrm{min}} \gg 1$ in most systems.

Assuming as typical velocity of the subject star that of a particle on a circular orbit at the edge of the galaxy

$$v^2 \approx \frac{GNm}{R}, \tag{2.1.9}$$

R is substituted in equation 2.1.6 by means of the above equation to obtain the total deflection-to-velocity ratio after one crossing

$$\frac{\Delta v^2}{v^2} \approx \frac{8 \ln \Lambda}{N}. \tag{2.1.10}$$

The number of crossings $\delta n_{\mathrm{relax}}$ needed to have $\Delta v^2 \approx v^2$ is then

$$\delta n_{\mathrm{relax}} \simeq \frac{N}{8 \ln \Lambda}. \tag{2.1.11}$$

The relaxation time t_{relax} is the timescale required to cross the system $\delta n_{\mathrm{relax}}$ times, so, called $t_{\mathrm{cross}} = R/v$ the **crossing time**, $t_{\mathrm{relax}} = \delta n_{\mathrm{relax}} t_{\mathrm{cross}}$. Furthermore, since $b_{\mathrm{min}} \equiv 2Gm/v^2$, we can write $\Lambda \approx Rv^2/(Gm) \approx N$ by equation 2.1.9, which leads to

$$t_{\mathrm{relax}} \simeq \frac{0.1 \, N}{\ln N} t_{\mathrm{cross}} \tag{2.1.12}$$

In all the stellar systems the dynamics over timescales shorter than $t_{\rm relax}$ is that of a **collisionless** system, in which the particles feel the gravitational field as if it were generated by a smooth density distribution. Table 2.1 reports the relaxation time and the lifetime-to-relaxation time ratio of many system categories, together with the parameters necessary to compute $t_{\rm relax}$. We notice that GCs are collisional stellar systems, since the typical lifetime of a GC is smaller than their relaxation time of at least an order of magnitude. Indeed, as we discussed in Section 1.1.3, such systems are experiencing processes related to relaxation, such as mass segregation and energy equipartition. Nonetheless, it is possible model the dynamical evolution of the GC as a sequence of many stationary collisionless systems, each over timescales shorter than $t_{\rm relax}$. In other words, the secular evolution of a GC, due to collisional effects, can be modelled by assuming that the system evolves through a series of steady-state solution of the collisionless Bolzmann equation (Section 2.2.1; see Hamilton et al. 2018).

System	N	R	v (km/s)	$t_{\rm relax}$ (yr)	$t_{\rm age}/t_{\rm relax}$
Open cluster	100	2 pc	0.5	10^7	$\gtrsim 1$
Globular cluster	10^5	4 pc	10	10^8	$\gtrsim 10$
Early type galaxy	10^{12}	10 kpc	200	10^{17}	$\sim 10^{-7}$

Table 2.1: From the left-hand to the right-hand column: system category (System); characteristic number of particles (N); characteristic scale radius (R); relaxation time ($t_{\rm relax}$); lifetime-to-relaxation time ratio ($t_{\rm age}/t_{\rm relax}$). Values from Binney & Tremaine (2008).

2.2 Theory of distribution functions

A collisionless system consisting of N particles can be modelled following the orbits of all the particles. However, since a typical stellar system (a GC or a galaxy) is composed by a very large number of particles, such an approach may be impractical and not worthwhile, and a statistical treatment may be preferred. Thus, following Binney & Tremaine (2008), we define $f(\mathbf{x}, \mathbf{v}, t)\, \mathrm{d}^3\mathbf{x}\, \mathrm{d}^3\mathbf{v}$ as the probability of finding a randomly chosen star in the six-dimensional phase-space volume $\mathrm{d}^3\mathbf{x}\, \mathrm{d}^3\mathbf{v} = \mathrm{d}^6\mathbf{w}$ centered in $(\mathbf{x}, \mathbf{v}) = \mathbf{w}$ at a time t. f is called **distribution function** (DF). As a probability density function, f must be such

$$\int_{\Omega \subseteq R^6} \mathrm{d}^3\mathbf{x} \mathrm{d}^3\mathbf{v} f(\mathbf{x}, \mathbf{v}, t) = 1, \qquad f(\mathbf{x}, \mathbf{v}, t) \geqslant 1 \quad \forall (\mathbf{x}, \mathbf{v}) \in R^6, \tag{2.2.1}$$

The above properties imply that the DF is normalized to unity when integrated over all the phase space and that it is everywhere a non-negative function. We notice that a DF can also be normalized in such a way that an integration over all the phase space gives the total mass of the system or the total number of stars. Unless otherwise specified, for the entire Thesis we will intend a DF normalized as in equation 2.2.1.

2.2.1 Collisionless Boltzmann Equation

As the stars move through the phase space, the DF must evolve in time in order to conserve the “star flux” in the phase space through time. The conservation of this flux is analogous to the conservation of mass in a fluid, where f resembles a fluid of stars moving through the phase space at a velocity $\dot{\mathbf{w}}$, so f must obey to the continuity equation

$$\frac{\partial f}{\partial t} + \sum_{k=1}^{6} \frac{\partial (f \dot{w}_k)}{\partial w_k} = 0. \tag{2.2.2}$$

Splitting the derivative of a product in the second term of the l.h.s. of equation 2.2.2 leads to

$$\frac{\partial f}{\partial t} + f \sum_{k=1}^{6} \frac{\partial \dot{w}_k}{\partial w_k} + \sum_{k=1}^{6} \dot{w}_k \frac{\partial f}{\partial w_k} = 0, \tag{2.2.3}$$

where the sum in second term can be explicitly written as

$$\sum_{k=1}^{3} \left(\frac{\partial v_k}{\partial x_k} + \frac{\partial \dot{v}_k}{\partial v_k} \right). \tag{2.2.4}$$

The first term of the above equation is zero since $\mathbf{v}$ and $\mathbf{x}$ are independent coordinates of the phase space, therefore $\partial v_k / \partial x_k = 0 \ \forall k = 1, 2, 3$. Also the second member is zero since

$$\dot{v}_k = -\frac{\partial H}{\partial x_k} = -\frac{\partial \Phi}{\partial x_k}, \tag{2.2.5}$$

where

$$H(\mathbf{x}, \mathbf{v}, t) = \frac{||\mathbf{v}||^2}{2} + \Phi(\mathbf{x}, t) \tag{2.2.6}$$

is the Hamiltonian of the system, with $\Phi = \Phi(\mathbf{x}, t)$ the gravitational potential of the system, which is independent on the velocity $\mathbf{v}$.

Considering the aforementioned rearrangements, equation 2.2.3 becomes

$$\frac{\partial f}{\partial t} + \sum_{k=1}^{6} \dot{w}_k \frac{\partial f}{\partial w_k} = 0, \tag{2.2.7}$$

which can be simply written as

$$\frac{\mathrm{d} f}{\mathrm{d} t} = 0, \tag{2.2.8}$$

having defined

$$\frac{\mathrm{d}}{\mathrm{d}t} \equiv \frac{\partial}{\partial t} + \sum_{k=1}^{3} \dot{w}_k \frac{\partial}{\partial w_k} \tag{2.2.9}$$

as the convective derivate, which describes the rate of change as seen by an observer who is travelling with the fluid.

Equations 2.2.7 and 2.2.8 are two different ways of writing the **Collisionless Boltzmann Equation** (CBE). In Cartesian coordinates, equation 2.2.7 can be written explicitly as

$$\frac{\partial f}{\partial t} + \sum_{k=1}^{3} \left(v_k \frac{\partial f}{\partial x_k} - \frac{\partial \Phi}{\partial x_k} \frac{\partial f}{\partial v_k} \right) = 0. \tag{2.2.10}$$

Now, defining a phase-space volume Ω, small enough to let $f(\mathbf{w})$ be constant in it, the probability of finding a star in Ω is $P = f(\mathbf{w}) \int_\Omega \mathrm{d}^6\mathbf{w}$. Let $\mathbf{W}$ be a new arbitrary set of coordinates, whose corresponding DF is $F(\mathbf{W})$; the probability of finding a star in Ω is then $P = F(\mathbf{W}) \int_\Omega \mathrm{d}^6\mathbf{W}$. Thus

$$P = f(\mathbf{w}) \int_\Omega \mathrm{d}^6\mathbf{w} = F(\mathbf{W}) \int_\Omega \mathrm{d}^6\mathbf{W}. \tag{2.2.11}$$

If $\mathbf{w}$ and $\mathbf{W}$ are sets of canonical coordinates, then $\int_\Omega \mathrm{d}^6\mathbf{w} = \int_\Omega \mathrm{d}^6\mathbf{W}$, therefore the above relation becomes

$$f(\mathbf{w}) = F(\mathbf{W}). \tag{2.2.12}$$

We say that a set of coordinates $\mathbf{w} = (\mathbf{q}, \mathbf{p})$ is canonical (for details see Binney & Tremaine 2008) when their Poisson's Brackets are such that

$$\{p_i, p_j\} = \{q_i, q_j\} = 0, \qquad \{q_i, p_j\} = \delta_{ij}, \tag{2.2.13}$$

where δ_{ij} is Kronecker's delta. Equations 2.2.11 and 2.2.12 state that the properties of the DFs are the same in any canonical coordinate system. Hence, equation 2.2.7 is valid for any canonical coordinate system.

In spherical coordinates $(r, \theta, \phi, p_r, p_\theta, p_\phi)$ the Hamiltonian is

$$H = \frac{1}{2} \left(p_r^2 + \frac{p_\theta^2}{r^2} + \frac{p_\phi^2}{r^2 \sin^2 \theta} \right) + \Phi, \tag{2.2.14}$$

while equation 2.2.7 becomes

$$\begin{aligned} \frac{\partial f}{\partial t} + p_r \frac{\partial f}{\partial r} + \frac{p_\phi}{r^2 \sin^2 \theta} \frac{\partial f}{\partial \phi} - \left(\frac{\partial \Phi}{\partial r} - \frac{p_\theta^2}{r^3} - \frac{\partial p_\phi^2}{r^2 \sin^3 \theta} \right) \frac{\partial f}{\partial p_r} \\ - \left(\frac{\partial \Phi}{\partial \theta} - \frac{p_\phi^2 \cos \theta}{r^2 \sin^2 \theta} \right) \frac{\partial f}{\partial p_\phi} - \frac{\partial \Phi}{\partial \phi} \frac{\partial f}{\partial p_\phi} = 0. \end{aligned} \tag{2.2.15}$$

In cylindrical coordinates $(R, \phi, z, p_R, p_\phi, p_z)$ the Hamiltonian is $H = \frac{1}{2}(p_R^2 + p_\phi^2/R^2 + p_z^2) + \Phi$ and equation 2.2.7 becomes

$$\begin{aligned} \frac{\partial f}{\partial t} + p_r \frac{\partial f}{\partial R} + \frac{p_\phi}{R^2} \frac{\partial f}{\partial \phi} + p_z \frac{\partial f}{\partial z} - \left(\frac{\partial \Phi}{\partial R} - \frac{p_\phi^2}{R^3} \right) \frac{\partial f}{\partial R} \\ - \frac{\partial \Phi}{\partial \phi} \frac{\partial f}{\partial p_\phi} - \frac{\partial \Phi}{\partial z} \frac{\partial f}{\partial p_z} = 0. \end{aligned} \tag{2.2.16}$$

However, it is important to notice that the CBE is a partial differential equation of phase-space coordinates and time that in general requires numerical solution.

2.2.2 The Jeans theorems

The Jeans theorem and the strong Jeans theorem (Jeans, 1915; Binney & Tremaine, 2008) are fundamental tools in the theory of DFs. While the Jeans theorem provides an easy way of writing DFs which always solve for the CBE, the strong Jeans theorem reduces the number of variables which a DF depends on when the system's orbits are regular (Bertin, 2000). A function of the phase-space coordinates $I(\mathbf{x}, \mathbf{v})$ is an integral of motion if and only if

$$\frac{\mathrm{d}}{\mathrm{d}t} I[\mathbf{x}(t), \mathbf{v}(t)] = 0 \tag{2.2.17}$$

along any orbit. Comparing equations 2.2.8 and 2.2.17, we notice that the condition for I to be an integral of motion is the same as requiring I to be a steady-state solution of the CBE (i.e $\partial f/\partial t = 0$ in equation 2.2.7). This is known as the Jeans theorem:

Any steady-state solution of the Collisionless Boltzmann equation depends on the phase-space coordinates only through integrals of motion in the given potential, and any function of the integrals yields a steady-state solution of the Collisionless Boltzmann Equation.

The first proposition of the theorem states that the DF can be written in terms of integrals of motion: we can infer the number of integrals of motion a DF can depend on studying the regularity of its stars' orbits. For example, a time-independent gravitational potential conserves the total energy, while a time-independent spherical potential conserves also the components of the angular momentum $\mathbf{L}$.

The strong Jeans theorem allows one to put constraints on the number of integrals of motion necessary to describe the DF:

The distribution function of a steady-state stellar system in which almost all orbits are regular with non-resonant frequencies may be presumed to be a function only of three independent isolating integrals, which may be taken to be the actions.

To summarize, if $I_1, \ldots, I_n$ are n independent integrals of motion of a given potential, then the DF can depend on any number of these integrals. In particular, if almost all orbits are regular, then the strong theorem states that the DF can depend on three independent integrals of motion, so it will be in the form $f(I_1, I_2, I_3)$.

2.2.3 Moments of a distribution function

Measuring the DF of any stellar system typically requires the use of a large number of stars with known position and velocity. In some approaches, studying the velocity moments of the DF is preferred, since any DF is uniquely defined by its moments. Here we list some of the most used moments of a DF, focusing on time-independent DFs.

Let $(\mathbf{x}, \mathbf{v})$ be a Cartesian coordinate system, the velocity moment of the 0-th order at any fixed position $\mathbf{x}$ is

$$\nu(\mathbf{x}) \equiv \int \mathrm{d}^3\mathbf{v}\, f(\mathbf{x}, \mathbf{v}), \tag{2.2.18}$$

and gives the probability of finding a star in the position $\mathbf{x}$, regardless of its velocity. From $\nu(\mathbf{x})$, we can easily define the luminosity and mass densities of stars as

$$\begin{aligned} j(\mathbf{x}) &= L\nu(\mathbf{x}), \\ \rho(\mathbf{x}) &= \mathrm{M}_\star \nu(\mathbf{x}), \end{aligned} \tag{2.2.19}$$

where L and $\mathrm{M}_\star$ are the total luminosity and total mass of the system, respectively. The stellar number density is $n(\mathbf{x}) = N\nu(\mathbf{x})$, where N is the total number of stars.

The i-th component of the velocity moment of the 1-st order is given by

$$\overline{v_i} \equiv \frac{1}{\nu(\mathbf{x})} \int \mathrm{d}^3\mathbf{v}\, v_i\, f(\mathbf{x}, \mathbf{v}), \qquad \text{with} \quad i = x, y, z, \tag{2.2.20}$$

and, at any fixed position $\mathbf{x}$, it represents i-th component of the mean velocity vector $\mathbf{v}$ at that location.

We also introduce the **velocity dispersion tensor $\boldsymbol{\sigma}$**, whose ij-th component is given by

$$\begin{aligned} \sigma_{ij}^2 &\equiv \int \mathrm{d}^3\mathbf{v}\, (v_i - \overline{v_i})(v_j - \overline{v_j}) f(\mathbf{x}, \mathbf{v}) \\ &= \overline{v_i v_j} - \bar{v}_i \bar{v}_j, \text{ with} \quad i, j = x, y, z, \end{aligned} \tag{2.2.21}$$

where

$$\overline{v_i v_j}(\mathbf{x}) = \frac{1}{\nu(\mathbf{x})} \int \mathrm{d}^3\mathbf{v}\, v_i v_j f(\mathbf{x}, \mathbf{v}) \tag{2.2.22}$$

is the velocity moment of the 2-nd order of f, and $\nu(\mathbf{x})$ is as in equation 2.2.18. We notice that $\boldsymbol{\sigma}$ is a symmetric tensor. In particular, if $i \neq j$, equation 2.2.22 refers to the mixed velocity moments of 2-nd order, whereas if $i = j$ equation 2.2.22 becomes

$$\overline{v_i^2}(\mathbf{x}) = \frac{1}{\nu(\mathbf{x})} \int \mathrm{d}^3\mathbf{v}\, v_i^2 f(\mathbf{x}, \mathbf{v}), \tag{2.2.23}$$

which is usually improperly called velocity moment of the 2-nd order. At any given position $\mathbf{x}$, the velocity dispersion tensor quantifies how much the stellar velocities are spread around their mean velocity.

In most cases, the aforementioned quantities are not directly measurable since the typical observer only looks at systems projected on the plane of the sky. As such, we also introduce some of the most commonly used projected velocity moments of a DF, which will be of the most relevance for this work. Called $\hat{\mathbf{s}}$ the unit vector directed along the line of sight, we define the **line-of-sight velocity distribution** (LOSVD) as

$$F(\mathbf{x}_\perp, v_\parallel) = \frac{\int \mathrm{d}x_\parallel\, \mathrm{d}^2\mathbf{v}_\perp\, f(\mathbf{x}, \mathbf{v})}{\int \mathrm{d}x_\parallel\, \mathrm{d}^3\mathbf{v}\, f(\mathbf{x}, \mathbf{v})}, \tag{2.2.24}$$

where $x_\parallel = \mathbf{x} \cdot \hat{\mathbf{s}}$ and $v_\parallel = \mathbf{v} \cdot \hat{\mathbf{s}}$ are the components of $\mathbf{x}$ and $\mathbf{v}$ along the line of sight, while $x_\perp = \mathbf{x} - x_\parallel\, \hat{\mathbf{s}}$ and $v_\perp = \mathbf{v} - v_\parallel\, \hat{\mathbf{s}}$ are the components of $\mathbf{x}$ and $\mathbf{v}$ parallel to the plane of the sky. The LOSVD gives the probability of finding a star with line-of-sight velocity between

$v_\parallel$ and $v_\parallel + \mathrm{d}v_\parallel$, in the position $\mathbf{x}_\perp$ on the plane of the sky. The 1-st moment of the LOSVD is the mean line-of-sight velocity $v_\parallel$, defined as

$$\begin{aligned}\overline{v_\parallel}(\mathbf{x}_\perp) &\equiv \int \mathrm{d}v_\parallel\, v_\parallel\, F(\mathbf{x}_\perp, v_\parallel) = \frac{\int \mathrm{d}x_\parallel\, \mathrm{d}^3\mathbf{v}\, v_\parallel\, f(\mathbf{x},\mathbf{v})}{\int \mathrm{d}x_\parallel\, \mathrm{d}^3\mathbf{v}\, f(\mathbf{x},\mathbf{v})} \\ &= \frac{N}{N}\frac{\int \mathrm{d}x_\parallel\, \nu(\mathbf{x})\, \hat{\mathbf{s}}\cdot\bar{\mathbf{v}}}{\int \mathrm{d}x_\parallel\, \nu(\mathbf{x})} = \frac{1}{\Sigma(\mathbf{x}_\perp)}\int \mathrm{d}x_\parallel\, n(\mathbf{x})\, \hat{\mathbf{s}}\cdot\bar{\mathbf{v}},\end{aligned} \tag{2.2.25}$$

where $\bar{\mathbf{v}}$ is the mean velocity vector, defined as in equation 2.2.20, and

$$\Sigma(\mathbf{x}_\perp) = \int \mathrm{d}x_\parallel\, n(\mathbf{x}) \tag{2.2.26}$$

is the projected number density. The 2-nd moment of the LOSVD is the line-of-sight velocity dispersion:

$$\begin{aligned}\sigma_\parallel^2(\mathbf{x}_\perp) &\equiv \int \mathrm{d}v_\parallel\, (v_\parallel - \overline{v_\parallel})\, F(v_\parallel; \mathbf{x}_\perp) \\ &= \frac{\int \mathrm{d}x_\parallel\, \mathrm{d}^3\mathbf{v}\, (\hat{\mathbf{s}}\cdot\mathbf{v} - \overline{v_\parallel})^2\, f(\mathbf{x},\mathbf{v})}{\int \mathrm{d}x_\parallel\, \mathrm{d}^3\mathbf{v}\, f(\mathbf{x},\mathbf{v})}.\end{aligned} \tag{2.2.27}$$

$\sigma_\parallel$ is linked to σ_{ij} by

$$\sigma_\parallel^2(\mathbf{x}_\perp) = \frac{1}{\Sigma(\mathbf{x}_\perp)}\int \mathrm{d}x_\parallel\, n(\mathbf{x})\, (\hat{\mathbf{s}}\cdot\boldsymbol{\sigma}^2\cdot\hat{\mathbf{s}} + u^2), \tag{2.2.28}$$

where $\hat{\mathbf{s}}\cdot\boldsymbol{\sigma}^2\cdot\hat{\mathbf{s}} \equiv \sum_{ij} s_i\sigma_{ij}s_j$ and $u(\mathbf{x}) \equiv \hat{\mathbf{s}}\cdot\bar{\mathbf{v}}(\mathbf{x}) - \overline{v_\parallel}$ the difference between the mean velocity component parallel to the line of sight at $\mathbf{x}$ and the mean line-of-sight velocity.

In the case of spherical systems, $\sigma_\parallel$ can be obtained from

$$\sigma_\parallel^2(R) = \frac{2}{\Sigma(R)}\int_R^\infty \mathrm{d}r \frac{\nu(r)}{\sqrt{r^2 - R^2}}\, \overline{v_r^2}\left(1 - \frac{R^2}{r^2}\beta\right), \tag{2.2.29}$$

where $R \equiv ||\mathbf{x}_\perp||$ is the magnitude of the position vector perpendicular to the line of sight, $\overline{v_r^2}$ is the mean squared velocity along the radial direction (equation 2.2.23) and β is the so-called anisotropy parameter (see Section 2.2.4).

2.2.4 Families of DFs for steady-state, collisionless, stellar systems

In this section we explore the properties of two particular families of DFs for systems confined by time-independent potentials, and systems confined by time-independent spherical potentials.

1. In the first case of a system confined by a steady-state gravitational potential $\Phi(\mathbf{x})$, the Hamiltonian (i.e. the total energy per unit mass)

$$H(\mathbf{x},\mathbf{v}) = \frac{||\mathbf{v}||^2}{2} + \Phi(\mathbf{x}) \tag{2.2.30}$$

is an integral of motion. Consequently, applying the first Jeans theorem, the DF of such a system can be taken to be a function $f(H)$ of the Hamiltonian per unit mass in equation 2.2.30. Since the Hamiltonian is an even function of all the velocity components, the DF is even as well. As such, applying equations 2.2.20 and 2.2.22, $\overline{\mathbf{v}}$ and $\overline{v_i v_j}$ are always null for $i, j = x, y, z,\ i \neq j$, while, in equation 2.2.23, $\overline{v_i^2} \neq 0$. Furthermore, since the Hamiltonian has the same dependence on the velocity components,

$$\overline{v_x^2} = \overline{v_y^2} = \overline{v_z^2}. \tag{2.2.31}$$

Thus, the velocity dispersion tensor reduces to

$$\begin{aligned} &\sigma \equiv \sigma_x = \sigma_y = \sigma_z \\ &\sigma_{ij} = 0 \qquad \text{for} \quad i, j = x, y, z,\ i \neq j. \end{aligned} \tag{2.2.32}$$

2. If the potential is spherical, the angular momentum magnitude L is another integral of motion, and the system can be described in general by a DF of the form $f(H, L)$ by means of the strong Jeans theorem. In spherical coordinates (r, ϕ, θ) the Hamiltonian becomes

$$H(r, \mathbf{v}) = \frac{1}{2}(v_r^2 + v_\phi^2 + v_\theta^2) + \Phi(r), \tag{2.2.33}$$

where v_r, v_ϕ, v_θ are the components of the velocity vector $\mathbf{v}$ along the radial, azimuthal and latitudinal directions, respectively. The angular momentum magnitude is $L = r(v_\phi^2 + v_\theta^2)^{1/2}$. As in the previous case, these DFs are even functions of all the velocity components, so $\overline{\mathbf{v}} = 0$ and $\overline{v_i v_j} = 0$ for $i, j = r, \phi, \theta,\ i \neq j$, while $\overline{v_i^2} \neq 0$, as in the previous DF family. However, since the dependence on v_θ and v_ϕ is different from the dependence on v_r, which does not appear in L, the velocity dispersion tensor is

$$\begin{aligned} &\sigma_r \neq \sigma_\phi = \sigma_\theta \\ &\sigma_{ij} = 0 \qquad \text{for} \quad i, j = r, \phi, \theta,\ i \neq j. \end{aligned} \tag{2.2.34}$$

We define

$$\beta(r) = 1 - \frac{\sigma_\theta^2 + \sigma_\varphi^2}{2\sigma_r^2} = 1 - \frac{\sigma_\theta^2}{\sigma_r^2}, \tag{2.2.35}$$

as the **anisotropy parameter**, which is in the range $-\infty < \beta \leqslant 1$. Depending on the value of $\beta(r)$, the velocity distribution of the system at r can be

- **radially biased** ($0 < \beta(r) \leqslant 1$): the radial velocity distribution at r is wider than the velocity distribution along the tangential direction, meaning that, at that radius, the system is more populated by stars performing large radial excursions rather than stars with large angular momentum;
- **tangentially biased** ($\beta(r) < 0$): the velocity distribution along the tangential direction is wider than the velocity distribution along the radial direction, therefore the stars tend to avoid eccentric orbits;
- **isotropic** ($\beta(r) = 0$): the velocity distribution in r is independent on the direction.

In the special case of spherical systems with known density ν and total potential Φ, it is possible to obtain the ergodic DF of the tracer by means of the Eddington's inversion formula

$$f(\mathcal{E}) = \frac{1}{\sqrt{8}\pi^2} \frac{\mathrm{d}}{\mathrm{d}\mathcal{E}} \int_0^{\mathcal{E}} \frac{\mathrm{d}\Psi}{\sqrt{\mathcal{E} - \Psi}} \frac{\mathrm{d}\nu}{\mathrm{d}\Psi}, \tag{2.2.36}$$

where $\Psi \equiv -\Phi + \Phi_0$ is the relative potential, $\mathcal{E} \equiv -H + \Phi_0 = \Psi - v^2/2$ is the relative energy.

Obtaining an analog of the Eddington's inversion formula 2.2.36 for DFs in the form $f(E, L)$ is possible only in some particular cases, for example for **Osipkov-Merritt models** (Osipkov, 1979; Merritt, 1985). Such models are described by DFs in the form $f(Q)$, with $Q \equiv \mathcal{E} - L^2/(2r_a^2)$, where r_a is the so-called **anisotropy radius**. The anisotropy parameter (equation 2.2.35) of these systems is

$$\beta(r) = \frac{r^2}{r^2 + r_a^2}. \tag{2.2.37}$$

The analogous of the Eddington's inversion formula for this family of DFs is

$$f(Q) = \frac{1}{\sqrt{8}\pi^2} \left[\int_0^Q \frac{\mathrm{d}\Psi}{\sqrt{Q - \Psi}} \frac{\mathrm{d}^2\nu_Q}{\mathrm{d}\Psi^2} + \frac{1}{\sqrt{Q}} \left(\frac{\mathrm{d}\nu_Q}{\mathrm{d}\Psi} \right)_{\Psi=0} \right]. \tag{2.2.38}$$

Any system that does not feel any external gravitational field, but only the mutual gravitational interactions of its own N components (for example multiple stellar populations, or stars and dark matter), is called **self-consistent**. The density ρ and gravitational potential Φ of each component are related by **Poisson's Equation**

$$\nabla^2\Phi(\mathbf{x}) = 4\pi G\rho = 4\pi G\,\mathrm{M} \int \mathrm{d}^3\mathbf{v}\, f(\mathbf{x}, \mathbf{v}), \tag{2.2.39}$$

where M and $f(\mathbf{x}, \mathbf{v})$ are the total mass and the DF of the component, respectively.

2.2.5 Examples of DFs applied to GCs

As we have shown in Sections 1.1.2 2.1, in GCs the two-body encounters can be sufficiently efficient to equally diffuse the stellar velocity along all the directions over relatively short timescales. From a theoretical point of view, the velocity distribution tends to be Maxwellian and the system, if assumed spherical and non-core collapsed (see Section 1.1.2), can be modelled as an isothermal sphere. A realistic DF for a GC should resemble an isothermal sphere in the inner regions, but it should also tend to zero when approaching the system truncation radius due, for instance, to the Galactic tidal field, as we discussed in Section 1.1.2. Hence, the DF should tend to zero for velocities close to the system escape velocity as well. Models that satisfy these properties are called **King models** (King, 1966), whose ergodic DF (Section 2.2.4) is

$$f(E) = \begin{cases} C(e^{-E/\sigma^2} - 1), & \text{if } E < 0, \\ 0, & \text{if } E \geq 0, \end{cases} \tag{2.2.40}$$

where $E = v^2/2 + \Psi(r)$ is the energy per unit mass, $\Psi(r) = \Phi(r) - \Phi(r_t)$ with r_t the system truncation radius. C is a normalization factor and σ is the velocity dispersion of the model (here we used the formalism of Miocchi 2006). Since the DF depends only on the energy, it has all the properties described Section 2.2.4. The density profile generated by this family of DFs, when requiring self-consistency, is characterized by a central flat core extending out r_0, the so-called King radius, with a drop in the outer regions. The structural properties of the model depend only on one parameter, the concentration $c = \log(r_t/r_0)$.

Slightly different than the King models, the Wilson DFs (Wilson, 1975) are

$$f(E) = \begin{cases} C[e^{-E/\sigma^2} - 1 + (E/\sigma^2)], & \text{if } E < 0, \\ 0, & \text{if } E \geq 0. \end{cases} \tag{2.2.41}$$

The Wilson DFs produce, in isolation, a density distribution which behaves similarly to King models in the central parts, with a gentler decrease in the outer parts. However, neither the King models nor the Wilson models include a central IMBH. Bahcall & Wolf (1976) introduced a new family of DFs which are essentially King models modified by the gravity of a central BH. In the formalism of Miocchi 2007, the DF is

$$f(E) = \begin{cases} C(-E)^{1/4}, & \text{if } E < -W_{\rm BH}, \\ (2\pi)^{-3/2}(e^{-E} - 1), & \text{if } -W_{\rm BH} \leq E < 0, \\ 0, & \text{if } E \geq 0, \end{cases} \tag{2.2.42}$$

where $W_{\rm BH}$ is the potential at the IMBH radius of influence (equation 1.2.3) and $C \equiv (2\pi)^{-3/2}(e^{W_{\rm BH}} - 1)W_{\rm BH}^{-1/4}$.

The so-called **Michie models**[1] are another extension of the King models. These models can be anisotropic and are defined by the DF

$$f(E, L) = \begin{cases} Ce^{-L^2/(2r_a^2\sigma^2)}(e^{-E/\sigma^2} - 1), & \text{if } E < 0, \\ 0, & \text{if } E \geq 0. \end{cases} \tag{2.2.43}$$

The DF 2.2.43 depends on the energy E and the angular momentum magnitude L, so it has all the properties listed in Section 2.2.4. Michie models are isotropic at the center and nearly radially biased in the outer regions, with r_a as a transition radius. Moreover, this DF reduces to King's DF (equation 2.2.40) for $r_a \to \infty$.

All the models presented above (excluding the Bahcall and Wolf models, equation 2.2.42) can be generalized by a single, parametric DF (**limepy models**; Gieles & Zocchi 2015):

$$f(E, L^2) = \begin{cases} A\, e^{-L^2/(2r_a^2 s^2)} E_\gamma\left(g, -\frac{E - \Phi(r_t)}{s^2}\right), & \text{if } E \leq \Phi(r_t), \\ 0, & \text{if } E > \Phi(r_t), \end{cases} \tag{2.2.44}$$

where r_t is the truncation radius and

$$E_\gamma(g, x) \equiv \begin{cases} e^x, & \text{if } g = 0, \\ e^x P(g, x), & \text{if } g > 0, \end{cases} \tag{2.2.45}$$

---

[1] For further details see Michie & Bodenheimer (1963)

where $P(g,x) \equiv \gamma(g,x)/\Gamma(x)$ is the regularized lower incomplete gamma function. The free parameters are: the central potential, which influences the concentration of the model; the anisotropy radius r_a and the truncation parameter $g \in R$, which determines the sharpness of the truncation. A and s are normalization constants, which determine the mass of the system, and the velocity scale, respectively. For example, when $g = 1$ we find the Michie models, when $g = 1$ and $r_a \to \infty$ the King models, while when $g = 2$ and $r_a \to \infty$ the Wilson models.

2.3 Dynamical models of GCs by means of action-based DFs

2.3.1 Action-angle coordinates

Action-angle variables $(\mathbf{J}, \boldsymbol{\theta})$ are a special set of canonical coordinates of the phase space. The actions $\mathbf{J}$ are integrals of motion, and they are conjugated to the angles $\boldsymbol{\theta}$, therefore

$$\dot{J}_i = -\frac{\partial H}{\partial \theta_i} = 0, \qquad \dot{\theta}_i = \frac{\partial H}{\partial J_i} = \Omega_i(\mathbf{J}), \tag{2.3.1}$$

where H is the Hamiltonian of the system and $\Omega_i(\mathbf{J})$ is the so-called i-th fundamental frequency. The above relations imply

$$H = H(\mathbf{J}), \qquad \theta_i(t) = \theta_i(0) + \Omega_i(\mathbf{J})t. \tag{2.3.2}$$

Thus, the Hamiltonian is independent on the i-th angle θ_i, which evolves linearly with time to a rate given by $\Omega_i(\mathbf{J})$.

Formally, the actions are defined through the integral invariant of Poincaré

$$\oint_\gamma \mathbf{p} \cdot \mathrm{d}\mathbf{q}, \tag{2.3.3}$$

where $(\mathbf{p}, \mathbf{q})$ is a set of canonical coordinates (Section 2.2.1) and γ is a close path in the phase space. It can be shown that, for any time t,

$$\oint_{\gamma(t)} \mathbf{p} \cdot \mathrm{d}\mathbf{q} = \oint_{\gamma(0)} \mathbf{p} \cdot \mathrm{d}\mathbf{q}, \tag{2.3.4}$$

where $\gamma(0)$ is $\gamma(t)$ evaluated in $t = 0$. In addition, the integral invariants of Poincaré are invariant under canonical transformation, therefore, called $(\mathbf{P}, \mathbf{Q})$ a new set of canonical coordinates,

$$\oint_\gamma \mathbf{p} \cdot \mathrm{d}\mathbf{q} = \oint_\gamma \mathbf{P} \cdot \mathrm{d}\mathbf{Q}. \tag{2.3.5}$$

Let us assume $(\mathbf{P}, \mathbf{Q}) = (\mathbf{J}, \boldsymbol{\theta})$. Since the actions $\mathbf{J}$ are integrals of motion, when the integral of Poincaré is evaluated along a close path $\gamma_i(t)$ over which the variable θ_i completes a full oscillation and the overall variations of the other angles are null, equation 2.3.5 can be written as

$$\oint_{\gamma_i} \mathbf{J} \cdot \mathrm{d}\boldsymbol{\theta} = 2\pi J_i. \tag{2.3.6}$$

By means of the above relation, equation 2.3.5 can be rearranged to define the i-th action as

$$J_i = \frac{1}{2\pi} \oint_{\gamma_i} \mathbf{p} \cdot \mathrm{d}\mathbf{q}. \tag{2.3.7}$$

Here we report the case of a spherical potential $\Phi(r)$, where we define the radial, azimuthal and latitudinal actions (J_r, J_ϕ, J_θ) as the actions associated to the radial, azimuthal and latitudinal directions r, ϕ, θ. In particular, it can be shown (Binney & Tremaine, 2008), that

$$\begin{aligned} J_\phi &= L_z, \qquad J_\theta = L - |L_z| = L - |J_\phi| \\ J_r &= \frac{1}{\pi} \int_{r_{\min}}^{r_{\max}} \mathrm{d}r \sqrt{2E - 2\Phi(r) - \frac{L^2}{r^2}}, \end{aligned} \tag{2.3.8}$$

where L is the angular momentum magnitude, L_z is the z-component of the angular momentum, E is the energy of the system, and $r_{\min}$ and $r_{\max}$ are the orbit pericentre and apocentre, respectively. Notice that actions have the same physical dimension of the angular momentum. To give a physical meaning to the actions, J_ϕ measures the degree of circular motion, while J_r and J_θ measure, respectively, the radial and latitudinal excursion of an orbit.

2.3.2 Action-based DFs

As stated in the previous section, the orbit of a star, if regular, is univoquely labelled by its actions. A DF depending on the actions $\mathbf{J}$ quantifies the probability of finding an orbit whose actions $\mathbf{J}$ are between $\mathbf{J}$ and $\mathbf{J} + \mathrm{d}\mathbf{J}$. Such a DF will be of the form (Binney, 2010, 2012)

$$f = f(\mathbf{J}). \tag{2.3.9}$$

The advantages of using action-based DFs are:

1. according to equation 2.3.2, the actions $\mathbf{J}$ make the ordinary phase-space coordinates periodic ($\mathbf{w} = \mathbf{w}(\boldsymbol{\theta} + 2\pi\mathbf{m}, \mathbf{J})$);

2. the actions span the entire action space. For instance, in a spherical system J_r and J_θ are always in $[0, +\infty)$, while J_ϕ is in $(-\infty, +\infty)$, independently on the values of the other actions. This is not true, for instance, for E and L: for instance, for given E in a spherical potential, the angular momentum magnitude range is from 0 to L_c, where L_c is the angular momentum magnitude of the circular orbit with energy E;

3. the number of orbits in a phase-space volume $\mathrm{d}^3\mathbf{J}$ is given by $(2\pi)^3\mathrm{d}^3\mathbf{J}$. If instead one assumes f in units of mass per unit phase-space volume (Section 2.2) the total mass is

$$\mathrm{M}_{\mathrm{tot}} = (2\pi)^3 \int \mathrm{d}^3\mathbf{J}\, f(\mathbf{J}) \tag{2.3.10}$$

Since the integral is independent on the system potential it can be computed a priori;

4. actions are adiabatic invariants, meaning that they remain unchanged under slow changes of the potential. This is an essential property when building a multi-component self-consistent model: for instance the slow accretion of a baryonic component to a dark-matter (DM) halo does changes the DM density distribution, but not the DF $f(\mathbf{J})$ of the halo (because the actions of the DM particle orbits are invariant);

5. Action-based DFs can be extended to deal with rotation and flattening in a relatively easy way.

While the existence of the actions is always guaranteed in a spherical potential and their evaluation is straightforward (equation 2.3.8), the numerical computation of $(\boldsymbol{\theta}, \mathbf{J})$ from $(\mathbf{x}, \mathbf{v})$ and vice versa in the case of a flattened potential is, in general, much more complicated (Sanders & Binney, 2014, 2016; Vasiliev, 2019).

2.3.3 DFs for GCs

Throughout this Thesis, the dynamical and structural properties of a GC will be modelled by the DF for GCs and dSphs illustrated by Pascale et al. (2019). Such DF was introduced and applied successfully to model the Fornax dSph (Pascale et al., 2018). We assume spherical symmetry, no dark matter and only one stellar population for the mock GCs. The expression of the DF is

$$f(\mathbf{J}) = \mathrm{M}_\star f_0 \exp\left[-\left(\frac{k(\mathbf{J})}{J_0}\right)^{\alpha}\right], \tag{2.3.11}$$

where $k(\mathbf{J})$ is defined as

$$k(\mathbf{J}) \equiv J_r + \eta(|J_\phi| + J_\theta) = J_r + \eta L, \tag{2.3.12}$$

with J_r, J_ϕ and J_θ the radial, azmuthal and vertical actions, L the angular momentum magnitude, and f_0 the normalization factor

$$f_0 = \frac{\eta^2 \alpha}{(2\pi J_0)^3 \Gamma(3/\alpha)}, \tag{2.3.13}$$

where Γ is the gamma function. The DF free parameters are:

1. the total GC stellar mass $\mathrm{M}_\star$;

2. the characteristic action J_0. The natural characteristic length and velocity scales are, respectively,

$$\begin{aligned} r_0 &\equiv \frac{J_0^2}{G\mathrm{M}_\star} \quad \text{and} \\ v_0 &\equiv \frac{G\mathrm{M}_\star}{J_0}. \end{aligned} \tag{2.3.14}$$

   By means of the above relations, any pair among the set $(J_0, \mathrm{M}_\star, r_0, v_0)$ determines the physical scales of the model;

3. the dimensionless, non-negative parameter η, which mainly determines the model velocity distribution;
4. the dimensionless, non-negative parameter α, which mainly determines the strength of the exponential cut-off in equation 2.3.11. Note, however, that there is a degeneracy between η and α, and different combinations of them may produce the same density profile (Pascale et al., 2019).

2.3.4 Adding an IMBH to the model

The stellar potential $\Phi_\star(r)$ and density distribution $\rho_\star(r)$ are related from the Poisson's equation

$$\nabla^2\Phi_\star = 4\pi G\rho_\star. \tag{2.3.15}$$

The stellar density is given by equations 2.2.18 and 2.2.19, which become

$$\rho_\star = \mathrm{M}_\star \int \mathrm{d}^3\mathbf{v}\, f(\mathbf{J}), \tag{2.3.16}$$

where $f(\mathbf{J})$ is the DF described in Section 2.3.3. When an IMBH is added at the center of the system, since the actions depend on the total gravitational potential $\Phi_{\mathrm{tot}}(r) = \Phi_{\mathrm{BH}}(r) + \Phi_\star(r)$, where Φ_{BH} is the potential of the BH, which, in the limit of Newtonian gravity, can be modelled as a Keplerian potential. However, the Keplerian potential diverges for $r = 0$, which can give rise to numerical problems for radial orbits, thus we modelled it as a Plummer sphere (Plummer, 1911)

$$\Phi_{\mathrm{BH}}(r) = -\frac{G\mathrm{M}_{\mathrm{BH}}}{\sqrt{r^2 + a^2}}, \tag{2.3.17}$$

where G is the gravitational constant, M_{BH} is the mass of the IMBH and a is a characteristic radius chosen to be much smaller than the radial distance of the innermost star of each mock. Therefore, for $r \gg a$, equation 2.3.17 tends to the Keplerian potential $-G\mathrm{M}_{\mathrm{BH}}/r$.

For what concerns the stellar density $\rho_\star$ and the gravitational potential $\Phi_\star$, the problem is non linear, and equations 2.3.15 and 2.3.16 must be solved numerically and iteratively, following the procedure by Binney (2014). Starting from an initial guess for the stellar potential $\Phi_\star$:

1. actions $\mathbf{J}(\mathbf{x}, \mathbf{v}; \Phi_{\mathrm{tot}})$ are computed by means of equations 2.3.8;
2. the stellar density distribution $\rho_\star$ is computed from equation 2.3.16;
3. using the stellar density distribution computed in the previous step, a new value for the stellar potential is given by equation 2.3.15.

After ~ 10 iterations, the total potential and the stellar density distribution converge to the self-consistent solution. Such a technique is based on the fact that the DF is conserved under slow changes of the potential, due to the adiabatic invariance of the actions (Section 2.3.2). The conservation of the DF implies that, if the gravitational potential changes, the density distribution will change, too. On the contrary, when the DF is built by means of Eddington's inversion (equation 2.2.36), the density is assumed constant, thus changes of the gravitational potential change the DF.

Chapter 3

Mock globular clusters

The 5th Gaia Challenge[1] consists of a collection of simulated observations of systems (mocks) resembling the properties of typical GCs and dwarf spheroidal galaxies (dSphs). Such mocks are samples of N identical stars, with known phase-space coordinates, extracted from a DF. Applying our models on mocks rather than real observational data allows us to avoid many of the issues discussed in Section 1.1.4 (field stars, multiple stellar population, mass segregation). Moreover, knowing a priori the properties of the system allows us to to test the inference power of our method. In Section 3.1 we introduce the most relevant properties of the mock GCs developed by E. Vasiliev, and we briefly describe the procedure used to generate such mocks (Sections 3.1.1, 3.1.2 and 3.1.3). In Section 3.2 we discuss the binning technique used to generate the projected number density $\Sigma_\star(R)$ and the line-of-sight velocity dispersion $\sigma_{\rm los}(R)$ profiles from the chosen mocks (Sections 3.2.1, 3.2.2, 3.2.3 and 3.2.4). In Section 3.3 we describe the method used to constrain our models based on DFs when applied to a selection of mock GCs. We analyze the properties of the parameter space defined by the DF (Section 3.3.1) and the approach used to find the best fit model (Section 3.3.3 and 3.3.4).

---

[1] `http://astrowiki.ph.surrey.ac.uk/dokuwiki/doku.php?id=gc5_mocks`

3.1 Mock generation

The mock GCs of the 5th Gaia Challenge are non-rotating spherically symmetric systems, they have no dark matter, may differ in the velocity distribution (isotropic or radially biased), in the mass of the IMBH in the center of their density distribution and in the number of particles. The stellar density distribution is

$$\rho_\star(r) = \rho_{\star,0}\left(\frac{r}{a}\right)^{-\gamma}\left[1+\left(\frac{r}{a}\right)^{\alpha}\right]^{(\gamma-\beta)/\alpha}, \tag{3.1.1}$$

where a is the scale radius, $\rho_{\star,0}$ is a reference density, γ, β and α are dimensionless parameters controlling the asymptotic central slope ($\rho_\star \to r^{-\gamma}$ for $r \to 0$), the outer slope ($\rho_\star \to r^{-\beta}$ for $r \to \infty$) and the sharpness of the transition between the two regimes, respectively. When $\gamma = 0$, $\beta = 5$ and $\alpha = 2$ the density profile is that of a Plummer sphere (Plummer, 1911). The profile used to generate these mocks has $\gamma = 0.1$, $\beta = 5$ and $\alpha = 2$, so it can be considered a modified Plummer sphere. The stellar gravitational potential $\Phi_\star(r)$ satisfies the Poisson equation $\nabla^2\Phi_\star = 4\pi G\rho_\star$, with G the gravitational constant and $\rho_\star$ given by equation 3.1.1. The total stellar mass of the mock is

$$\mathrm{M}_\star = 4\pi\int_0^{+\infty}\rho_\star(r)\,r^2\,\mathrm{d}r. \tag{3.1.2}$$

When present, the IMBH at the center of a mock GC is modelled as the Keplerian potential

$$\Phi_{\mathrm{BH}}(r) = -\frac{G\mu_{\mathrm{BH}}\mathrm{M}_\star}{r}, \tag{3.1.3}$$

where r is the distance from the BH, $\mu_{\mathrm{BH}} \equiv \mathrm{M}_{\mathrm{BH}}/\mathrm{M}_\star$ is the BH-to-stellar mass fraction, with M_{BH} the mass of the IMBH. In this case, the total potential is $\Phi_{\mathrm{tot}}(r) = \Phi_\star(r)+\Phi_{\mathrm{BH}}(r)$. The values of the parameters used to build the mocks are listed in Table 3.1.

3.1.1 Setting the DF

Given the density profile $\rho_\star$ (equation 3.1.1) and the total gravitational potential Φ_{tot}, the DF of the system is obtained via the Eddington's inversion 2.2.36 (see also Binney & Tremaine 2008). The resulting DF will depend on the chosen velocity distribution, which can be either

i) isotropic with an ergodic DF $f(E)$, depending on the energy of the stars E (Section 2.2.4);

ii) radially biased with a DF $f(E, L)$, with L the angular momentum magnitude, of the form of Osipkov-Merrit (Section 2.2.4).

Once the DF is known, N phase-space coordinates $w_i = (x_i,y_i,z_i,v_{x,i},v_{y,i},v_{z,i})$, with $i = 1$, ..., N are extracted from the DF exploiting the von Neumann's algorithm for extracting random samples of variables from a given probabity density function.

Parameter	Value
a (pc)	3.13
$\rho_{\star,0}$ ($\mathrm{M}_\odot/\mathrm{pc}^3$)	7526
γ	0.1
β	5
α	2
$M_\star$ ($\mathrm{M}_\odot$)	10^6
μ_{BH}	0, 0.01 or 0.001
r_a/a	1 (OM), ∞ (Iso)
N	10^3, 10^4 or 10^5

Table 3.1: Parameters used to generate the GC mocks. a: scale radius of the GC (equation 3.1.1); $\rho_{\star,0}$: reference density of the GC (equation 3.1.1); γ, β and α: dimensionless parameters regulating the inner slope, the outer slope and the sharpness of transition between the two, respectively (equation 3.1.1); $\mathrm{M}_\star$: stellar mass of the GC; μ_{BH}: IMBH-to-stellar mass fraction; r_a/a: anisotropy scale radius-to-Plummer sphere characteristic radius ratio (equations 2.2.37 and 3.1.1); N: number of particles sampled from the DF.

3.1.2 Gaia-like coordinate conversion

Assuming to observe a 47 Tucanae-like GC, with an heliocentric distance $D = 5$ kpc (Harris, 1996), in order to mimic a typical GC, the N phase-space coordinates w_i of each mock are modified to deal with projection effects and observational errors.

1. The line of sight is the z-axis and, called the (X,Y)-plane the plane of the sky, the sky positions X_i and Y_i (in radiants) are computed as

$$\begin{aligned} X_i &= -\frac{x_i}{D}, \\ Y_i &= \frac{y_i}{D}. \end{aligned} \tag{3.1.4}$$

   The sky positions are then converted in degrees. Also, $v_{\mathrm{los},i} \equiv v_{z,i}$, where $v_{\mathrm{los},i}$ is the line-of-sight velocity of the i-th star.

2. The proper motion angular velocities $\mathrm{PM}_{X,i}$ (along the X-axis) and $\mathrm{PM}_{Y,i}$ (along the Y-axis), in mas/yr, follow from

$$\begin{aligned} \mathrm{PM}_{X,i} &= -\frac{v_{x,i}}{\eta}, \\ \mathrm{PM}_{Y,i} &= \frac{v_{y,i}}{\eta}, \end{aligned} \tag{3.1.5}$$

   for $i = 1, ..., N$, where $\eta = 4.74$ km/s[PM/(mas/yr)](D/kpc) is the conversion factor from km/s to mas/yr.

3. Stars with an angular separation $\theta > 1°$ from the center of the system are removed: this feature causes the total number of particles per mock to be, in most cases, slightly less than N (see Table 3.3).

3.1.3 Velocity uncertainties

The errors over the PM velocities PM_X and PM_Y are assigned in order to be consistent with the ones expected from the Gaia data release 2 (Gaia DR2; Gaia Collaboration et al. 2018), or the future 5 (Gaia DR4) and 10 years data releases after the beginning of the Gaia mission. Since the mocks studied throughout this Thesis have PMs errors chosen to mimic Gaia DR2, we will refer to this release from now on.

The PMs errors are computed according to the analytic $\delta\mathrm{PM} - \mathrm{mag}$ relation, obtained fitting the PM errors $\delta\mathrm{PM}$ and V band apparent magnitudes of stars m_V from the Gaia DR2 release through the function

$$\delta\mathrm{PM} = \delta\mathrm{PM}_{20}\, 10^{[0.352(m_V-20)+0.021(m_V-20)^2]}, \tag{3.1.6}$$

where $\delta\mathrm{PM}_{20}$ is a normalization, defined as the uncertainty of a star with apparent magnitude $m_V = 20$. In Figure 3.1 we show the best fitting relation 3.1.6 alongside the observational data from the Gaia DR2, while the values of $\delta\mathrm{PM}_{20}$ are reported in Table 3.2.

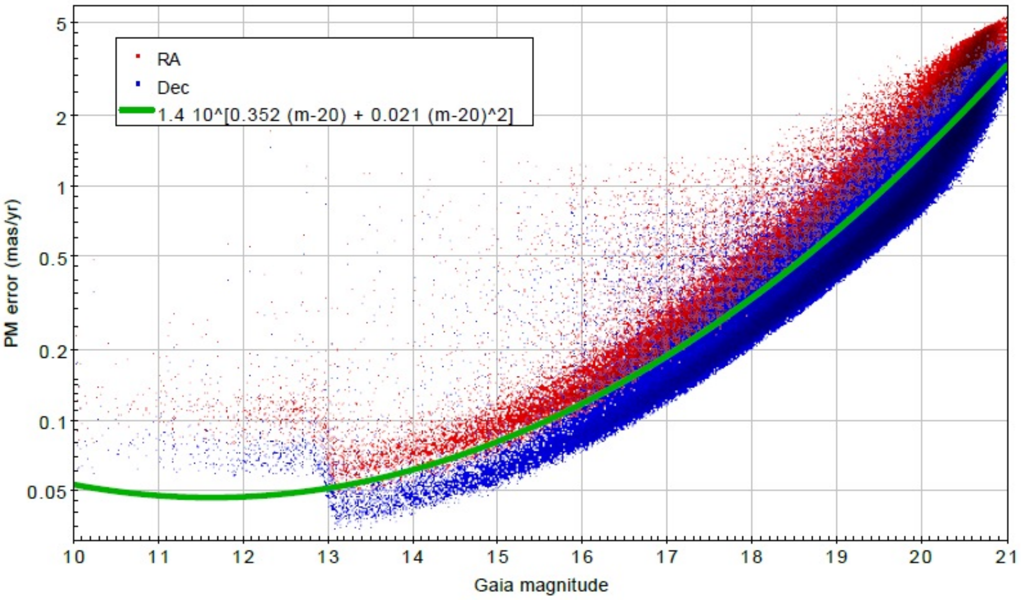

Figure 3.1: PM uncertainties of the stars from the Gaia DR2 release as a function of the star apparent magnitude, in the field of Messier 4. Green line: best fit relation (equation 3.1.6); red points: RA errors; blue points: Dec errors. Credits Gaia Challenge website.

While the data in Figure 3.1 scatter above and below the analytic relation 3.1.6, the PM errors on the stars of the mocks are generated assuming no intrinsic scatter. To compute the uncertainties on the PMs of the stars using equation 3.1.6 it is necessary to assign them an apparent magnitude. The number of stars with V band apparent magnitude between m_V and $m_V + \mathrm{d}m_V$ is

$$\frac{\mathrm{d}N}{\mathrm{d}m_V} = \begin{cases} N_{14}\, 10^{[\xi(m_V-14)]}, & \text{if } m_V < m_{\mathrm{sat}}, \\ N_{14}\, 10^{[\xi(m_{\mathrm{sat}}-14)]}, & \text{if } m_V > m_{\mathrm{sat}}, \end{cases} \tag{3.1.7}$$

Survey	$\delta\mathrm{PM}_{20}$ (mas/yr)
Gaia-DR2	1.4
Gaia-DR4	0.32
Gaia-10 years	0.112

Table 3.2: Values of the normalization $\delta\mathrm{PM}_{20}$ (i.e. the uncertainty on PM of a star with V-band apparent magnitude $m_V = 20$, equation 3.1.6) expected for different Gaia releases (Survey). Credits Gaia Challenge website.

where m_{sat} is the magnitude at which Gaia saturates (both for high crowding and high flux) and N_{14} is the value of the distribution at $m_V = 14$. The relation 3.1.7 is inferred fitting the observed magnitude distribution from the Gaia DR2 data of Figure 3.2, showing the magnitude distributions of field stars (red histogram) and GC candidate members (blue histogram). The plateu in GC star counts at high magnitudes implies $m_{\mathrm{sat}} \simeq 17$. This is due to the fact that GC stars are more crowded than field stars. Indeed, the red histogram does not show a plateu and declines only at much fainter magnitudes ($m_V \gtrsim 20$). The best fit parameters of the GC members distribution are $\xi = 0.4$, and $N_{14} = 120$.

To summarize, to each star of the mock GCs an apparent magnitude is assigned by means of equation 3.1.7; once the magnitude is known, the PM errors can be computed using the formula 3.1.6.

The error on the line-of-sight velocities is 2 km/s for all the stars in any of the mocks, which is optimisic since fainter stars or stars located in the central crowded regions of a GC would have higher uncertainties. Once the uncertanties on the i-th velocity is assigned, all the velocity components are re-extracted from a multivariate Gaussian distribution with mean vector $\boldsymbol{\mu}_i = (v_{\mathrm{los},i}, \mathrm{PM}_{X,i}, \mathrm{PM}_{Y,i})$ and with diagonal covariance matrix whose diagonal elements are the errors on the velocities.

Considering all the combinations of the mock parameters (see Table 3.1), the optional presence of field stars, the different ways in which the uncertainties on the PMs are assigned, together with the fact that there are up to 4 different realizations for the same mock, 378 mocks are distributed by the 5-th Gaia Challenge.

3.2 Characteristics of the considered mocks and data sets

Throughout this Thesis we have studied four isotropic mocks, with varying total number of stars N and different IMBH-to-stellar mass fraction μ_{BH} (see Table 3.3). Also, we focused on mocks with PM errors similar to those obtained by the Gaia DR2.

Extrapolating the Magorrian relation (see Section 1.2) at low-mass stellar systems, GCs are likely to host IMBHs with mass fraction $\mu_{\mathrm{BH}} \simeq 0.001$. Nonetheless we try to test the perfomances of our method and the ability to infer the presence of an IMBH also in the more favorable scenario of a more massive IMBH, where we may expect stronger features caused by the IMBH gravity in the GC center. Also, we take into account mocks with same

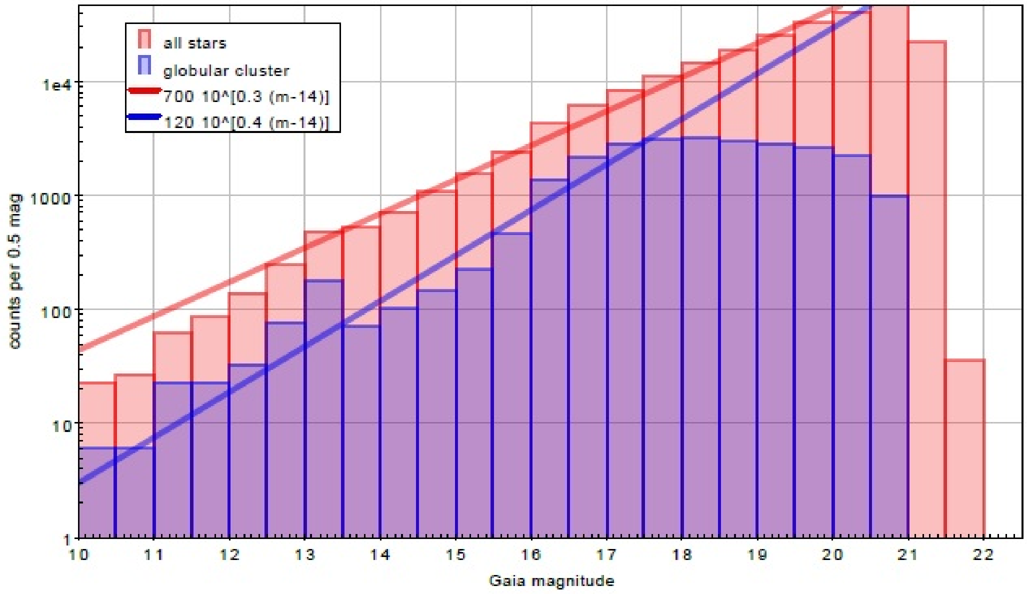

Figure 3.2: Star counts as a function of the apparent magnitudes. The values are referred to the region of Messier 4, the red histogram represents field stars, while the blue histogram represents GC candidate members. Credits Gaia Challenge website.

$\mu_{\rm BH}$ and same structural and kinematic properties, but having different numbers of stars : the case of $\sim 10^3$ stars represents the typical number of stars expected in a realistic data set of a GC; the case of $\sim 10^4$ stars represents an optimistic case mimicing future spectoscopic surveys. The specific values of $\mu_{\rm BH}$ and N of the mocks we analyzed are listed in Table 3.3, together with their effective radii $R_{\rm eff}$ (i.e. the projected distance on the plane of the sky within which half of the total projected mass is contained).

Mock	N	$\mu_{\rm BH}$	$R_{\rm eff}$ (pc)
N1e4_mu1e-2	9986	0.01	3.063
N1e3_mu1e-2	999	0.01	2.919
N1e4_mu1e-3	9986	0.001	3.018
N1e3_mu1e-3	998	0.001	3.107

Table 3.3: Properties of the mocks analyzed in this Thesis. From the left-hand to the right-hand column; name of the mock (Mock); number of selected stars (N); IMBH-to-stellar mass fraction ($\mu_{\rm BH}$); effective radius ($R_{\rm eff}$).

3.2.1 Data set

As the study of observational data is usually performed via projected number density and line-of-sight velocity dispersion profiles, in this Section we describe the binning technique adopted to build such profiles from the mock discussed in Section 3.1. We assume to have no field stars, no uncertainty on the identification of the center of the system, a population of identical stars and that the mass-to-light ratio of the mock GCs is constant, which implies that the surface brightness is related to the projected number density profile by an arbitrary constant.

3.2.2 Projected number density profile

We compute the projected number density profile $\Sigma_\star$ of a given mock as follows. The (X, Y)-plane of the sky is divided into $N_{\rm bin}$ spherical shells. The projected distance of the i-th star is computed as $(X_i^2+Y_i^2)^{1/2}$ and the radii R_j of the edges of the shells are such that $\log R_{j+1} - \log R_j = \Delta \, \forall j = 1, .., N_{\rm bin}$, and Δ chosen accordingly to the requested number of bins $N_{\rm bin}$. For the j-th bin we compute

$$\Sigma_{\star,j} = \frac{n_j}{\pi(R_{j+1}^2 - R_j^2)}, \quad \text{with}\, j = 1,\, ...,\, N_{\rm bin}, \tag{3.2.1}$$

as the projected number density of the j-th bin. In the above equation, n_j is the total number of stars in the j-th bin, whose edges are R_j and R_{j+1}. The j-th bin is labeled with the distance from the center of the mock GC obtained avereging the distances of the stars of that bin.

The uncertainties on the projected number density profile are computed considering two factors: deviation from circular symmetry (1), statistics (2).

1. As shown in Figure 3.3 in the case of mock N1e4_mu1e-2, the system is divided into 4 identical quadrants, and in each quadrant we compute the projected number density profile using the same radial bins as in the main profile. The error on the projected number density $\Sigma_{\star,j}$ of the j-th bin is

$$\delta\Sigma_{\star,j}^{\rm asymm} = \frac{1}{A_j/4}\left[\frac{1}{4}\sum_{k=1}^{4}(n_{jk} - \bar{n}_{{\rm quad},j})^2\right]^{1/2}, \tag{3.2.2}$$

   where n_{jk} is the number of stars of the j-th bin in the k-th quadrant, $\bar{n}_{{\rm quad},j}$ is the mean number of stars of the j-th bin between the quadrants and A_j is the area of the j-th spherical shell.

2. The number of counts n_j of the j-th bin follows a Poisson distribution, so the contribution to the total error is $\delta\Sigma_{\star,j}^{\rm P} = \Sigma_{\star,j}/n_j^{1/2}$.

The total uncertainty $\delta\Sigma_{\star,j}$ over the j-th bin is then given by

$$\delta\Sigma_{\star,j} = \sqrt{(\delta\Sigma_{\star,j}^{\rm asymm})^2 + (\delta\Sigma_{\star,j}^{\rm P})^2}, \tag{3.2.3}$$

which allows us to consider both possible deviations from circular symmetry and bin statistics.

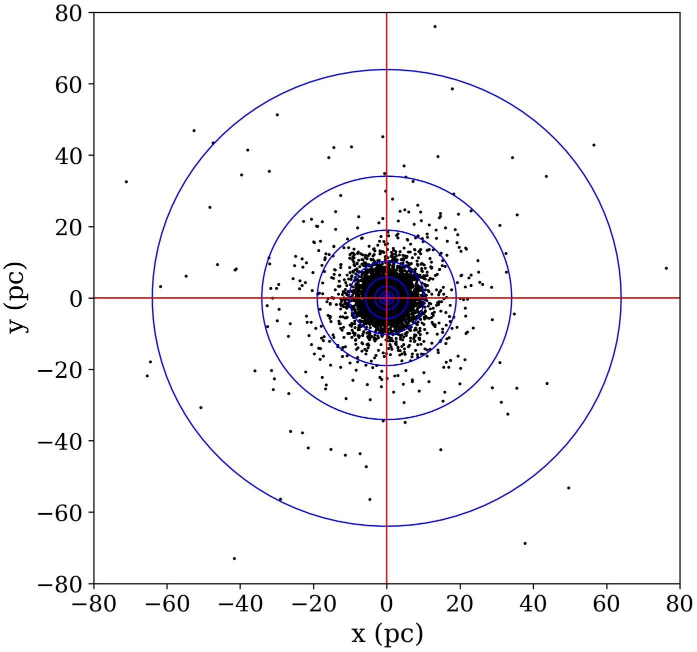

Figure 3.3: Projected spatial distribution of the stars (black points) of mock N1e4_mu1e-2. The line-of-sight is the z-axis, so the plane of the sky is the xy plane. The blue circles represent the edges of the radial bins, while the red lines divide the plane into the 4 quadrants. For details on how the profile is built see Section 3.2.2.

3.2.3 Line-of-sight velocity dispersion profile

We compute the line-of-sight velocity dispersion profile of the mock GCs as follows. Differently from the case of the projected number density profile, each radial bin of the $\sigma_{\rm los}$ profile is built such to contain the same number of stars, apart for the central bin which will have, in general, fewer number of stars. Indeed, we adopt the same binning as in van der Marel & Anderson (2010), where the central bin has less stars to achieve both high resolution in a small region and to isolate the stars affected the most by the gravity of the IMBH.

For each bin, the line-of-sight velocity dispersion $\sigma_{{\rm los},j}$ is calculated as (Pryor & Meylan, 1993)

$$\sigma^2_{{\rm los},j} = \frac{1}{n_j}\sum_{i=1}^{n_j}(v_i - \bar{v}_j)^2 - \sigma_e^2, \tag{3.2.4}$$

where n_j is the number of stars in the j-th bin, $\bar{v}_j$ is the bin's average line-of-sight velocity, σ_e is the error on the line-of-sight velocity measurement, and the sum extends over the line-of-sight velocities v_i of the stars of that bin. We recall that, in our case, $\sigma_e = 2$ km/s for all the stars of each mock (Section 3.1.3). Equation 3.2.4 corrects $\sigma_{\rm los}$ for the spurious contribution given by the observational measurement uncertainty. The error on the line-of-sight velocity of the j-th bin is defined as (Pryor & Meylan, 1993)

$$\delta\sigma^2_{\mathrm{los},j} = \frac{(\sigma^2_{\mathrm{los},j} + \sigma^2_e)^2}{2n_j\sigma^2_{\mathrm{los},j}}. \tag{3.2.5}$$

The j-th bin is labeled with the average distance of all the stars falling in that bin, as we did in Section 3.2.2 for the projected number density profile.

3.2.4 Dependence of σ_{los} on the binning

An IMBH in the center of a stellar system dominates the gravity at radii smaller than the IMBH radius of influence R_{infl} (see equation 1.2.3). Since we compute the value of each bin of the line-of-sight velocity dispersion $\sigma_{\mathrm{los},j}$ through equation 3.2.4, if the majority of the stars within the first bin are far from the sphere of influence of the IMBH, then the central cusp in the σ_{los} profile is erased.

In Figure 3.4 we show two line-of-sight velocity disperion profiles computed from the mock N1e4_mu1e-2, which has an IMBH with $\mu_{\mathrm{BH}} = 0.01$ and a total number of stars $N = 9986$ (Table 3.3). The profile in the left-hand panel is built with a central bin with 25 stars while the other bins with 500 stars (as listed in Table 3.4). The profile in the right-hand panel has, instead, bins with the same number of stars (approximately 500). Since in the first case the first bin is mainly populated by stars within the IMBH sphere of influence, the line-of-sight velocity dispersion profile in the left-hand panel shows the expected central cusp. On the contrary, the uniformly binned profile in the right-hand panel is flat in the inner regions, meaning that the majority of the stars in the first bin are far from the IMBH. Figure 3.4 also shows the position of R_{infl}, computed as in equation 1.2.3, using the line-of-sight velocity dispersion of the second bin as a measure of $\sigma(R_{\mathrm{infl}})$ and exploiting our prior knowledge of $\mathrm{M}_\star$ and μ_{BH} (see Table 3.3), which resemble the average GC mass and the expected value of IMBH on the basis of the Magorrian relation (see Section 1.2).

In conclusion, given the line-of-sight velocities of N GC member stars uniformly distributed in the plane of the sky, and assuming $\mu_{\mathrm{BH}} = 0.01$ as upper limit for the IMBH-to-stellar mass fraction, we estimate that building the first bin with at least $2.5 \times 10^{-3} N$ stars, assuming N sufficiently large, allows one, in principle, to disantangle the IMBH signature in the center of the GC, if present, keeping the errorbar sufficiently small.

3.3 Model-data comparison

As described in Section 3.2.1, starting from any of the selected mocks of Section 3.2, we compute the projected number density (Section 3.2.2) and the line-of-sight velocity dispersion profiles (Section 3.2.3). The resulting data set consists of the two triplets of vectors:

- $(R_j, \Sigma_{\star,j}, \delta\Sigma_{\star,j})$ with $j = 1, ..., N_{\mathrm{bin}}$, where R_j is the radial distance of the j-th bin from the center of the mock GC, $\Sigma_{\star,j}$ is the corresponding projected number density, $\delta\Sigma_{\star,j}$ is the projected number density error and N_{bin} is total number of bins;

Mock	First bin	Other bins	$R_{\rm infl}$ (pc)	$N_\star(< R_{\rm infl})$
N1e4_mu1e-2	25	500	$1.97 \cdot 10^{-1}$	50
N1e3_mu1e-2	25	120	$2.20 \cdot 10^{-1}$	6
N1e4_mu1e-3	25	500	$2.01 \cdot 10^{-2}$	2
N1e3_mu1e-3	25	120	$2.58 \cdot 10^{-2}$	0

Table 3.4: From left-hand to right-hand columns: name of the mock (Mock); number of stars within the central bin (First bin); number of stars in each of the other bins except the first bin (Other bins); IMBH radius of influence ($R_{\rm infl}$); number of stars within $R_{\rm infl}$ ($N_\star(< R_{\rm infl})$).

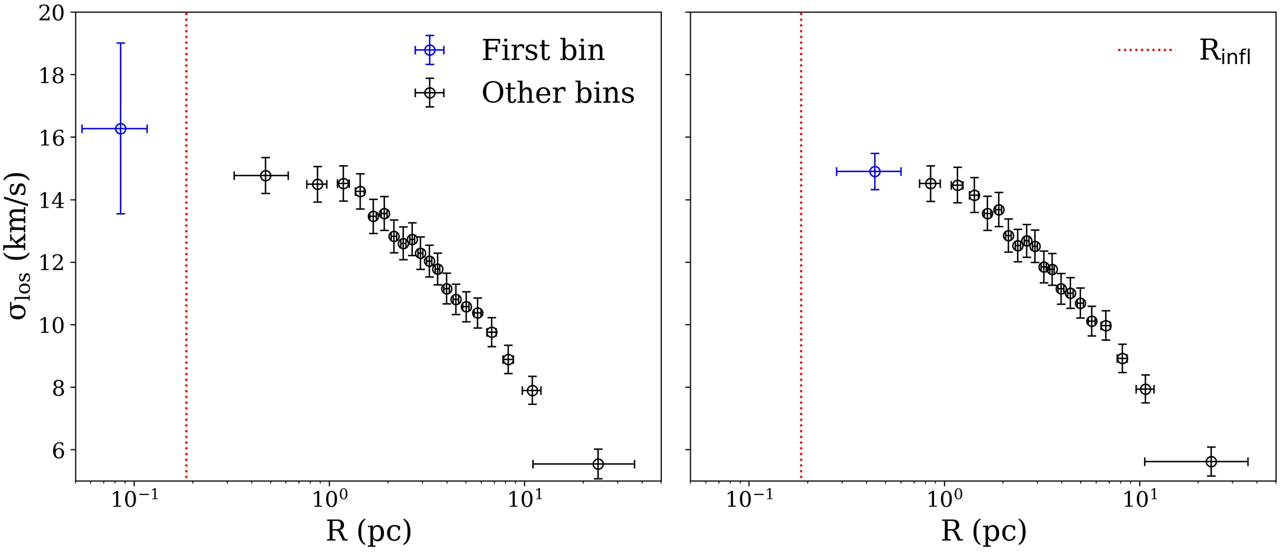

Figure 3.4: Left-hand panel: line-of-sight velocity dispersion profile of mock N1e4_mu1e-2 (Table 3.3). The first bin has 25 stars while the other bins have approximately 500 (Table 3.4). Right-hand panel: line-of-sight velocity dispersion profile of mock N1e4_mu1e-2. The vertical dashed line shows the position of the radius on influence of the IMBH (equation 1.2.3). All the bins have approximately 500 stars. In both the panels the red vertical curve shows the position of the radius of influence (Table 3.4).

- $(R_k, \sigma_{{\rm los},k}, \delta\sigma_{{\rm los},k})$ with $k = 1, ..., M_{\rm bin}$, where R_k is the radial distance of the k-th bin from the center of the mock, $\sigma_{{\rm los},k}$ is the corresponding line-of-sight velocity dispersion, $\delta\sigma_{{\rm los},k}$ is the line-of-sight velocity dispersion error and $M_{\rm bin}$ is total number of bins.

We note that, in general, $N_{\rm bin} \neq M_{\rm bin}$. Moreover, even if $N_{\rm bin} = M_{\rm bin}$, due to the very different binning technique adopted to build the projected number density and the line-of-sight velocity dispersion profiles, the profiles will not be evaluated at the same radii anyway.

3.3.1 Model fitting

We compare the data sets we built from the target mocks and the DF-based models (Section 2.3.3) by means of a χ^2 fitting approach. The χ^2 of a model, given the data, is

$$\chi^2 = \chi^2_{\Sigma_\star} + \chi^2_{\sigma_{\rm los}}, \tag{3.3.1}$$

where the first term in the r.h.s. is

$$\chi^2_{\Sigma_\star}(\mathbf{p}) = \sum_{i=1}^{N_{\rm bin}} \left(\frac{\Sigma_\star(R_i;\mathbf{p}) - \Sigma_{\star,i}}{\delta\Sigma_{\star,i}} \right)^2, \tag{3.3.2}$$

where $\Sigma_\star(R_i;\mathbf{p})$ is the model projected number density computed at R_i, depending on the set of free parameters $\mathbf{p} = (\alpha, \eta, \mu_{\rm BH}, {\rm M}_\star, J_0)$, as stated in Section 2.3.3.

Similarly, the second term of the r.h.s. of equation 3.3.1 is

$$\chi^2_{\sigma_{\rm los}}(\mathbf{p}) = \sum_{k=1}^{M_{\rm bin}} \left(\frac{\sigma_{\rm los}(R_k;\mathbf{p}) - \sigma_{{\rm los},k}}{\delta\sigma_{{\rm los},k}} \right)^2, \tag{3.3.3}$$

where $\sigma_{\rm los}(R_k;\mathbf{p})$ is the model line-of-sight velocity dispersion computed at R_k, depending on $\mathbf{p}$.

We model the mock GCs as described in Section 2.3.4: the stellar component of the mock GC is described by means of the action-based DF 2.3.11, while the BH contribution through the Plummer potential 2.3.17. The best fit model is the one corresponding to a set of parameters that minimizes equation 3.3.1. We briefly summarize the free parameters of the model:

1. the total GC stellar mass ${\rm M}_\star$;
2. the characteristic action J_0;
3. the dimensionless, non-negative parameter η, which mainly determines the model velocity distribution;
4. the dimensionless, non-negative parameter α, which mainly determines the strength of the exponential cut-off in equation 2.3.11;
5. the IMBH-to-stellar mass fraction $\mu_{\rm BH} \equiv {\rm M}_{\rm BH}/{\rm M}_\star$.

Once ${\rm M}_\star$ and J_0 are fixed, the characteristic length and velocity scales r_0 and v_0 can be computed as in equation 2.3.14. Models that share the dimensionless parameters $(\alpha, \eta, \mu_{\rm BH})$ are homologous, meaning that they can be scaled on each other only changing the physical scales of a model (${\rm M}_\star$ and J_0).

As we have seen in Section 1.1.4, the issues that may arise in deriving a high-quality binned dataset of GC are varius. Here we consider our mocks as a best case scenario since:

- both the projected number density and the line-of-sight velocity dispersion profiles have been constructed knowing the center of the GC;

- there is no contamination by field stars;
- the mocks have stars of the same mass, are not affected by mass segregation and we assume a constant mass-to-total particles ratio $\mathrm{M}_\star/N$ or mass-to-light ratio $\mathrm{M}_\star/L$ over the full GC radial extent. This choice allows us to unanbigously switch from particle density to mass density or luminosity.

3.3.2 Physical scaling of a model

After the projected number density and line-of-sight velocity dispersion profiles of both the mock and the model are built, we are able to compute the χ^2 of the model and to find the best fit values of the triplet $(\alpha, \eta, \mu_{\mathrm{BH}})$ performing the gradient descent (Section 3.3.3). We exploit the system homology to save computational time and reduce the dimensionality of the parameter space to obtain the best fit values of J_0 and $\mathrm{M}_\star$. For any given triplet $(\alpha, \eta, \mu_{\mathrm{BH}})$

1. we fix J_0 and $\mathrm{M}_\star$ to the initial guess values
$$J_{0,0} = 0.01\,\mathrm{kpc\,km/s}; \quad \mathrm{M}_{\star,0} = 10^6\,\mathrm{M}_\odot. \tag{3.3.4}$$
2. Given a triplet $(\alpha, \eta, \mu_{\mathrm{BH}})$ and the pair $(J_{0,0}, \mathrm{M}_{\star,0})$, a model in physical scales is univoquely determined and its projected number density profile $\Sigma_{\star,i}$ and line-of-sight velocity dispersion $\sigma_{\mathrm{los},i}$ profiles are computed. We further compute the model and the mock effective radii R_{eff} and $R_{\mathrm{eff,mock}}$, respectively.
3. Exploiting the system homology we rescale the model onto the physical scale of the mock requiring
$$\frac{r_{0,f}}{R_{\mathrm{eff,mock}}} = \frac{r_{0,0}}{R_{\mathrm{eff}}} \Longrightarrow r_{0,f} = r_{0,0}\left(\frac{R_{\mathrm{eff,mock}}}{R_{\mathrm{eff}}}\right). \tag{3.3.5}$$
This allows us to find the new model scale length $r_{0,f}$ (see equation 2.3.14) that makes the model effective radius equal to the one inferred from the mock. As a consequence, the projected number density $\Sigma_{\star,f}$ is re-scaled as
$$\Sigma_{\star,f} \equiv \left(\frac{r_{0,0}}{r_{0,\mathrm{mock}}}\right)^2 \Sigma_{\star,i}, \tag{3.3.6}$$
where $\Sigma_{\star,i}$ is the initial projected number density.
4. After rescaling the model on the correct physical scale, we further require
$$v_{0,f} = \left(\frac{\sigma_{\mathrm{eff,mock}}}{\sigma_{\mathrm{los,eff}}}\right) v_{0,0}, \tag{3.3.7}$$
where $v_{0,f}$ and $v_{0,0}$ are the final and initial characteristic scale velocities of the model (equation 2.3.14), and $\sigma_{\mathrm{eff,mock}} \equiv \sigma_{\mathrm{los,mock}}(R_{\mathrm{eff,mock}})$ and $\sigma_{\mathrm{los,eff}} \equiv \sigma_{\mathrm{los},0}(R_{\mathrm{eff}})$ are the line-of-sight velocity dispersions at the effective radii of the mock and the model,

respectively. The line-of-sight velocity dispersion profile of the model is then rescaled according to

$$\sigma_{\mathrm{los},f} \equiv \left(\frac{v_{0,f}}{v_{0,i}}\right)\sigma_{\mathrm{los},0}, \tag{3.3.8}$$

where $\sigma_{\mathrm{los},f}$ is the rescaled line-of-sight velocity dispersion profile. In order to better constrain the characteristic velocity scale, we evaluate $\chi^2_{\sigma_{\mathrm{los}}}$ ($\chi^2_{\Sigma_\star}$ is independent on v_0) changing $v_{0,f}$ up to the 10% of the value obtained from equation 3.3.7 and keeping the value that minimizes $\chi^2_{\sigma_{\mathrm{los}}}$.

5. The final values of the characteristic scale action $J_{0,f}$ and the total mass of the system $\mathrm{M}_{\star,f}$ are computed from $r_{0,f}$ and $v_{0,f}$ by means of equation 2.3.14.

3.3.3 Gradient descent

The *gradient descent* is a set of techniques that allows one to compute iteratively the minimum of a given function. Among the gradient descent techniques, the algorithm that adopted in this Thesis is called *Gauss-Newton method.* In our case, we aim to minimize equation 3.3.1 with respect to the m-dimensional free parameter vector $\mathbf{p}$. We exploit the system homology as described in the previous section, so we use the gradient descent to minimize equation 3.3.1 with respect to the 3 dimensional free parameter vector $\mathbf{p} = (\alpha, \eta, \mu_{\mathrm{BH}})$. We rearrange equation 3.3.1 as

$$\chi^2(\mathbf{p}) = \sum_{i=1}^{n} r_i^2(\mathbf{p}), \tag{3.3.9}$$

where the first N_{bin} terms r_i^2 are the terms of equation 3.3.2, while the latter M_{bin} terms are the terms of equation 3.3.3, so $n \equiv N_{\mathrm{bin}} + M_{\mathrm{bin}}$. We further define the array $\mathbf{r}(\mathbf{p}) \equiv (r_1, ..., r_n)$, as the n-dimensional vector with elements r_i.

Now let $J(\mathbf{p}) \in R^{n\times m}$ be the Jacobian matrix of $\mathbf{r}(\mathbf{p})$, whose ij-th component is given by

$$J(\mathbf{p})_{ij} = \frac{\partial r_i(\mathbf{p})}{\partial p_j}. \tag{3.3.10}$$

Using equations 3.3.9 and 3.3.10, the j-th component of the gradient $\nabla\chi^2(\mathbf{p}) \in R^m$ can be written as

$$[\nabla\chi^2(\mathbf{p})]_j = [2J(\mathbf{p})^T\mathbf{r}(\mathbf{p})]_j = \left[2\sum_{i=1}^{n} r_i(\mathbf{p})\nabla r_i(\mathbf{p})\right]_j, \quad j = 1, ..., m. \tag{3.3.11}$$

Consequently, the jk-th component of the Hessian matrix $\mathcal{M}_{\chi^2}(\mathbf{p}) \in R^{m\times m}$ of $\chi^2(\mathbf{p})$ can be computed as

$$\begin{aligned}[\mathcal{M}_{\chi^2}(\mathbf{p})]_{jk} &= [2J(\mathbf{p})^T J(\mathbf{p}) + 2\nabla J(\mathbf{p})^T\mathbf{r}(\mathbf{p})]_{jk}, \\ &= \left\{2\sum_{i=1}^{n} \nabla r_i(\mathbf{p})\nabla r_i(\mathbf{p})^T + 2\sum_{i=1}^{n} r_i(\mathbf{p})\mathcal{M}_{r_i}(\mathbf{p})\right\}_{jk}, \\ & j, k = 1, ..., m.\end{aligned} \tag{3.3.12}$$

The necessary condition to have a minimum is that all the components of $\nabla\chi^2(\mathbf{p})$ are null (Fermat's theorem), so, applying this condition to equation 3.3.11, we get

$$\nabla\chi^2(\mathbf{p}) = 0 \quad \Longrightarrow \quad 2J(\mathbf{p})^T\mathbf{r}(\mathbf{p}) = 0. \tag{3.3.13}$$

This non-linear system can be solved iteratively using, for instance, the Newton's method. Starting from the k-th iteration, we evaluate p_{k+1}, i.e. the free parameters at the $(k+1)$-th iteration, solving

$$\begin{aligned} \mathcal{M}_{\chi^2}(\mathbf{p}_k)\,\mathbf{s}_k &= -\nabla\chi^2(\mathbf{p}_k), \\ (J^TJ + \nabla J^T\mathbf{r})\mathbf{s}_k &= -J^T\mathbf{r}. \end{aligned} \tag{3.3.14}$$

where we have called $\mathbf{s}_k = \mathbf{p}_{k+1} - \mathbf{p}_k \in R^m$ the step vector in the parameter space at the k-th iteration.

In the special case of $r_i \ll 1$ for each $i = 1, ..., N$, the second term in the l.h.s. of the second equations 3.3.14, which can be quite expensive to compute since it requires the numerical evaluation of second derivatives, can be neglected. Equation 3.3.14 then becomes

$$(J^TJ)\mathbf{s}_k = -J^T\mathbf{r}, \tag{3.3.15}$$

Solving equation 3.3.15 for $\mathbf{s}_k$, the method converges to the set of parameters corresponding to the minimum of the function after few iterations.

As a criteria to check whether the algorithm has reached the minimum of χ^2, at each iteration we check

$$\begin{aligned} &1) \quad \left[\nabla\chi^2(\mathbf{p}_k)\right]_j < 10^{-d}, \quad \text{for each } j = 1, ..., m;\ d \in N, \\ &2) \quad [\mathbf{s}_k]_j < 10^{-d}. \end{aligned} \tag{3.3.16}$$

If any of the above conditions is satisfied, the algorithm stops and we define the latest $\chi^2(\mathbf{p}_k)$ as the minimum of χ^2, to a precision of 10^{-d} for each parameter.

In this project, the gradient descent technique has been numerically implemented requiring in equation 3.3.16 that $d = 2$ for α and η, $d = 1$ for $\log\mu_{\mathrm{BH}}$. We tested the algorithm assuming higher values of d and we did not find any appreciable change in the physical properties of the best model. Since a higher precision for these parameters (in particular α, η and $\log\mu_{\mathrm{BH}}$) would increase the computational time needed to converge to the best fit model, we standardize to the values listed above.

3.3.4 Exploration of the parameter space

Once the algorithm has converged to the best fitting model using the gradient descent described in Section 3.3.3, we compute the uncertainties on the models' free parameters $\mathbf{p}$ as follows. Let $\chi^2_{\min}$ be the lowest χ^2 among the models explored, and let $\mathbf{p}_{\min}$ be the corresponding set of free parameters ($\chi^2_{\min} \equiv \chi^2(\mathbf{p}_{\min})$), we define the $K\sigma$ model as those

$$\chi^2(\mathbf{p}_j) - \chi^2_{\min} < \Delta\,\chi^2_{m,K} \tag{3.3.17}$$

where $\chi^2(\mathbf{p}_j)$ is the chi-squared evaluation for a model defined by a set of parameters $\mathbf{p}_j$ and $\Delta\,\chi^2_{m,K}$ is a threshold depending on the number of free parameters m and on the required K-th confidence level (see Table 3.5, taken from Press et al. 1992).

$\Delta\,\chi^2_{m,K}$	$m = 1$	$m = 2$	$m = 3$	$m = 4$	$m = 5$	$m = 6$
$K = 1$	1.00	2.30	3.53	4.72	5.89	7.04
$K = 2$	4.00	6.17	8.02	9.70	11.3	12.8
$K = 3$	9.00	11.8	14.2	16.3	18.2	20.1

Table 3.5: Values of $\Delta\,\chi^2_{m,K}$ (equation 3.3.17) corresponding to $K\sigma$ confidence levels for a total number of free parameters m (Press et al., 1992).

Since the quality of the fit (i.e. the value of $\chi^2_{\rm tot}$, equation 3.3.1) is highly sensitive to variations of the characteristic scale length r_0, we fix it to the value $r_{0,f}$. We will discuss and motivate this choice in Section 4.1.1 showing some specific examples.

3.3.5 Building self-consistent models and extracting models' observables with AGAMA

Model building and DF moments computation have been performed using AGAMA[2] (Action-based Galaxy Models Architecture). AGAMA is a publicly available software library for a broad range of applications in stellar dynamics, developed by E. Vasiliev and described in Vasiliev (2019). It provides methods and routines to compute the gravitational potential of arbitrary analytic density profiles or N-body snapshots; it performs transformations between position-velocity $(\mathbf{x}, \mathbf{v})$ and action-angle $(\mathbf{J}, \boldsymbol{\theta})$ variables both in spherical systems, numerically solving equation 2.3.8, and non-spherical systems, adopting a technique called Stäckel-Fudge (Sanders & Binney, 2016); it builds self-consistent multi-component dynamical models; it stores a collection of analytic action-based DFs and of the most commonly used analytic potential-density pairs, together with two versatile potential expansions that can be constructed from any density distribution or from an N-body model; it provides the moments of a DF integrating along the phase-space coordinates, according to the equations listed Section 2.2.3; it performs also orbit integration and analysis. The library is written in C++, but provides also a Python adn Fortran interface, and can be coupled to other stellar-dynamical software: AMUSE, GALPY and NEMO. We briefly comment on the procedure used by AGAMA to find the self-consistent stellar density potential pair $(\rho_\star, \Phi_\star)$ generated by the DF 2.3.11 when an IMBH potential is added to the total potential. Starting from an initial guess for the stellar gravitational potential:

1. it first evaluate the actions $\mathbf{J}(\mathbf{x}, \mathbf{v}; \Phi_{\rm tot})$ by means of equations 2.3.8;
2. it computes the stellar density distribution $\rho_\star$ from equation 2.3.16;
3. it computes the stellar potential by means of equation 2.3.15;
4. it starts again from step 1 using the new value of the stellar potential.

The algorithm converges fast, after a total of approximately 10 iterations.

---

[2] `https://github.com/GalacticDynamics-Oxford/Agama`

Chapter 4

Results

In this Chapter we present the results obtained fitting the projected number density and line-of-sight velocity dispersion profiles of the selection of mock GCs presented in Section 3.2 with the dynamical models based on analytic DFs depending on the actions of Sections 2.3.3 and 2.3.4. The projected number density profiles of the mocks are built as described in Section 3.2.2, with a total number of bin $N_{\rm bin} = 15$, while the line-of-sight velocity dispersione profiles are built according to Sections 3.2.3 and 3.2.4, so that they contain 50 particles in the first bin and 500 or 120 in the other bins, depending on the total number of stars $N \simeq 10^4$ or $N \simeq 10^3$, respectively. In Sections 4.1 and 4.2 we show the results obtained for the mocks with $\mu_{\rm BH} = 10^{-2}$ and $\mu_{\rm BH} = 10^{-3}$, respectively. Also, in Section 4.1.1 we explore the dependence of the models on the parameter J_0.

4.1 Mock GCs with $\mu_{\rm BH} = 0.01$

In this Section we present the results obtained fitting the mock GCs with $\mu_{\rm BH} = 0.01$ with the action-based models of Section 2.3.3. We check if our models are able to infer the presence of the IMBH and the correct stellar velocity distribution, and we explore how our results depend on the number of particles of the mocks, which can be either $N \simeq 10^3$ (N1e3_mu1e-2) or $N \simeq 10^4$ (N1e4_mu1e-2). As we pointed out in Section 1.2, we explore the case of $\mu_{\rm BH} = 0.01$, which is an upper limit to the IMBH-to-stellar mass fraction expected extrapolating the Magorrian relation at the GC masses.

The model fitting is performed using the scheme described in Section 3.3.3: given the free parameter vector $\mathbf{p} = (\alpha, \eta, {\rm M}_\star, \mu_{\rm BH})$, we start from a guess $\mathbf{p_0}$ and use the gradient descent to find the best fitting model. Once we have found the best fitting model we further explore the parameter space with a uniform grid search, as described in Section 3.3.4, to find the models within 1σ and 3σ uncertainties (hereafter 1σ models and 3σ models).

Figures 4.1 and 4.2 show the projected number density profiles of the mocks N1e4_mu1e-2 and N1e3_mu1e-2 superimposed to the best fitting models and the 1σ models. In both cases, the core of constant density in the center of the projected number density profiles is well reproduced. Also, at least up to $R \simeq 5R_{\rm eff}$ the DF-based models provide an extremely accurate fit to the observed profiles, apart for the outermorst regions, where the best models have a steeper decrease than the observed profiles. This slight discrepancy is caused by the specific choice of the DF: while the density profiles generated by the family of DFs 2.3.11 are, in isolation, characterized by a flat core in the inner regions and an exponential cut-off in the outer regions, the mocks have intrinsic and projected density distributions that fall off as power laws[1] in the outskirts (equation 3.1.1). However, apart for the last bin, the models nicely reproduce the overall projected number density profile, so we consider the slight misfit with the last bin of little significance. In fact, more quantitatively, we notice that the mass enclosed within $R = 63.98\,{\rm pc} \simeq 20R_{\rm eff}$ (corresponding to the last point of the projected density profile still in agreement with the best fit models) is 99.73% of the total number of stars. In other words, the best models well reproduce the behavior of the projected number density profiles of the mocks over the full radial extent of the mock, almost over 5 orders of magnitude in projected density, apart for the very outermost regions, where the contribution to the total number of particles (and thus the total mass or the total luminosity) is negligble and the number density of the tracer has almost dropped to zero. Also, one should consider that, when dealing with real observational data, at these distances the contamination by field stars is dominant.

By construction, the density distribution of the mocks has a mild cusp $\rho_\star \to r^{-0.1}$ for $r \to 0$ (equation 3.1.1), which becomes almost flat in case of the corresponding projected number density. To quantify the steepness of the cusp in the projected number density profiles, we evaluted the logarithmic slope $\gamma_{\Sigma_\star} \equiv {\rm d}\log\Sigma_\star/{\rm d}\log R$. The log-slope of the mock GCs is $\gamma_{\Sigma_\star}(r \to 0) \simeq -0.0001 \sim 0$. In case of the 1σ models of mock N1e4_mu1e-2, $\gamma_{\Sigma_\star}(r \to 0) = -0.292^{+0.044}_{-0.045}$, higher then the expected value for the mocks. This is a consequence of the fact that in self-consistent multi-component models based on $f(\mathbf{J})$ DF,

---

[1] The power law density profile at large radii is not typical of real GCs, which might be better represented by our models.

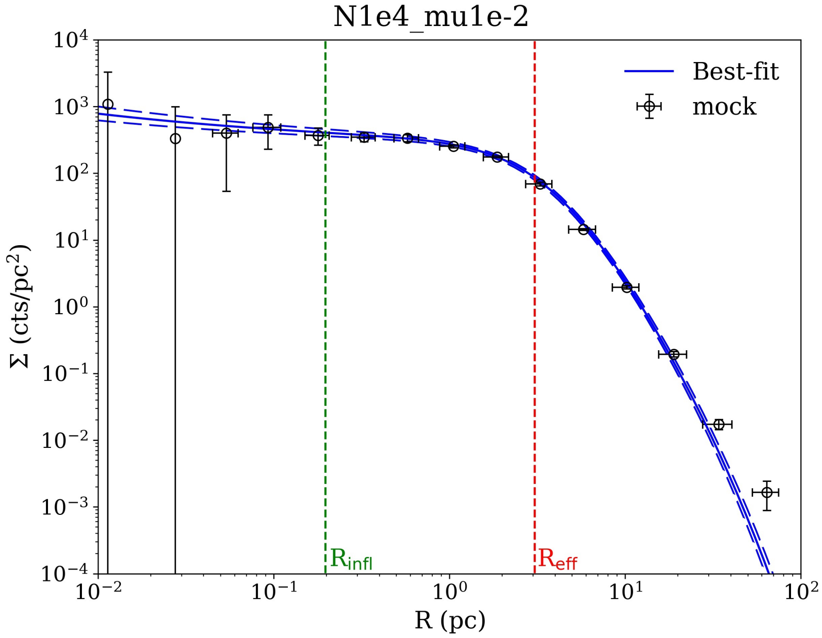

Figure 4.1: Projected number density profiles of the mock N1e4_mu1e-2 (black open dots with errorbars), superimposed to the best fitting model (blue solid line) and the 1σ models (blue dashed line; see Table 4.1). We also show the radius of influence of the IMBH ($R_{\rm infl}$, vertical green dashed line; Table 3.4) and the effective radius of the mock ($R_{\rm eff}$, vertical red dashed line; Table 3.3).

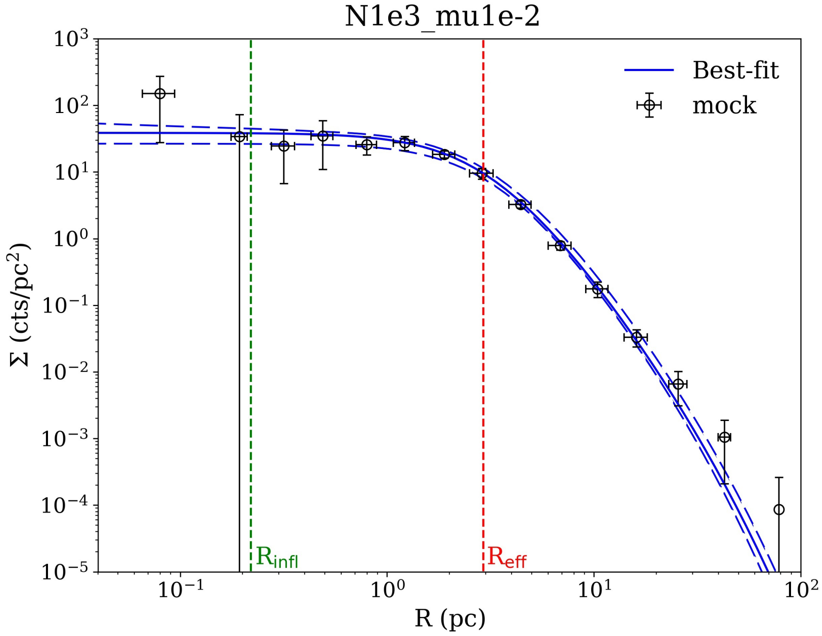

Figure 4.2: Same as Figure 4.1, but for mock N1e3_mu1e-2.

the density distribution of each component is modified by the presence of other components, so the central IMBH tends to steepen the central density distribution (see figure 9 in Pascale et al. (2019)). In case of the 1σ models of mock N1e3_mu1e-2, where we measure a log-slope $\gamma_{\Sigma_\star}(r \to 0) = -0.005^{+0.002}_{-0.097}$, almost consistent with $\gamma \simeq 0$. Table 4.1 lists the values of the parameters of the best fit models of mocks N1e4_mu1e-2 and N1e3_mu1e-2, together with the uncertainties given at a confidence levels of 1σ and 3σ.

Figures 4.3 and 4.4 show the line-of-sight velocity dispersion profiles of the mocks N1e4_mu1e-2 e N1e3_mu1e-2 superimposed to the best fitting models and the 1σ models. As we saw in Section 3.2.4, the adopted binning techinque allows us to isolate the region within the BH radius of influence and to highlight in both profiles the cusps due to the IMBH expected in their centers. Also in these cases the models well reproduce the line-of-sight velocity dispersion profiles of the mocks. In case of mock N1e3_mu1e-2, the region marked by the 1σ models is wider than in mock N1e4_mu1e-2. The profile of N1e3_mu1e-2 has both less bins (thus poorer statistics) and fewer particles per bin (thus larger errorbars) with respect to N1e4_mu1e-2, which lowers inevitably the inference power of the models. The fit with the line-of-sight velocity dispersion profiles strongly depends on the number of particles of the mocks. When using $N \simeq 10^4$ stars (N1e4_mu1e-2) the models not only reproduce the cusp at the center, but also the 1σ models are consistent with $\mu_{\rm BH} \neq 0$. For mock N1e3_mu1e-2, on the contrary, we put an upper limit on $\mu_{\rm BH}$ of 3.18×10^{-2} (1σ uncertainties), meaning that, within 1σ, it is consistent with both $\mu_{\rm BH} = 0.03$ and no BH (for further details see Table 4.1). This is a first indication that in our best case scenario (no contamination by field stars, correct evaluation of the GC center, constant M/L, a large BH-to-stellar mass fraction) any method relying on the fit with binned projected number density and line-of-sight velocity dispersion profiles requires $\sim 10^4$ stars with known line-of-sight velocity.

In Figures 4.5 and 4.6 we show the anisotropy parameter β (equation 2.2.35) profiles of the best fit models and the 1σ models for mocks N1e4_mu1e-2 and N1e3_mu1e-2. In both cases the velocity distributions of the best models are mainly tangentially biased within 1σ, apart from the innermost regions, where the models tend to isotropy by construction. The mocks have isotropic velocity distribution (see Section 3.2), thus $\beta \equiv 0$ independent of radius. Our models, at least in the case of these first two mocks, are able to recover the mock velocity distribution only within 3σ. As representative values of the anisotropy parameter of the models, we evaluate $\beta(R_{\rm eff})$, i.e. the anisotropy parameter profile at $R_{\rm eff}$, finding $\beta(R_{\rm eff}) = -0.164^{+0.023}_{-0.024}$ for N1e4_mu1e-2 and $\beta(R_{\rm eff}) = -0.177^{+0.098}_{-0.057}$ for N1e3_mu1e-2.

We stress, however, that even if the correct value of the anisotropy parameter of the mocks are recovered only within 3σ, this does not affect the ability of the models to infer the correct BH-to-stellar mass fraction. Also, we point out that the DF 2.3.11, by construction, does not allow to produce models that are everywhere isotropic (for details see Pascale et al. 2019) and that the discrepancy between the mock and models velocity distribution may be, probably, an indication that the DF 2.3.11 is not be flexible enough.

To show the effects of the IMBH on the velocity distribution of the stars, in Figures 4.7 and 4.8 we show the LOSVDs (equation 2.2.24) of the best fit models of N1e4_mu1e-2 and N1e3_mu1e-2 (black line), evaluated at the radii of influence of the corresponding mocks (see Table 3.4). To show the effects of the IMBH, we also show the LOSVD at $R_{\rm infl}$

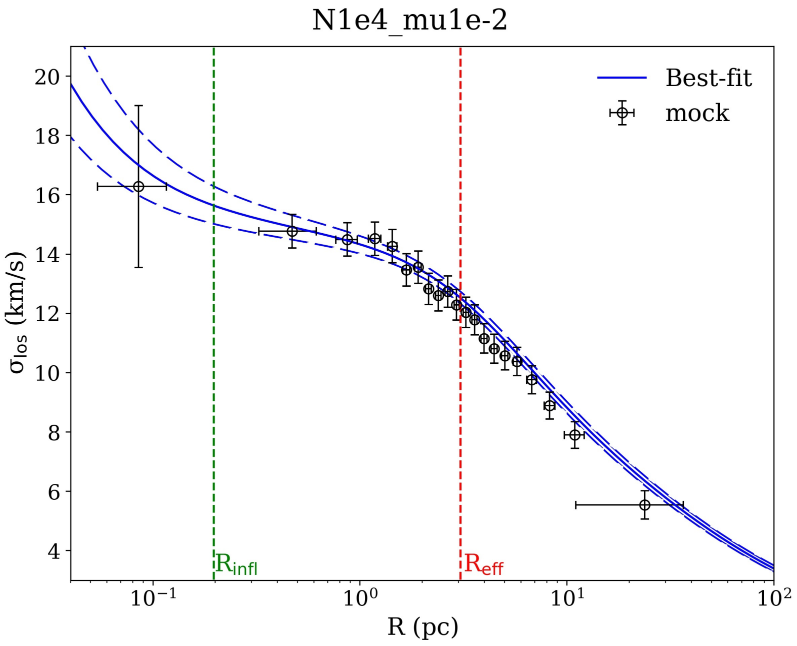

Figure 4.3: Line-of-sight velocity dispersion profiles of the mocks N1e4_mu1e-2 (black open dots with errorbars), superimposed to the best fitting model (blue solid line) and the 1σ models (blue dashed line; see Table 4.1). We also show the radius of influence of the IMBH ($R_{\rm infl}$, vertical green dashed line; see Table 3.4) and the effective radius of the mock ($R_{\rm eff}$, vertical red dashed line; see Table 3.3).

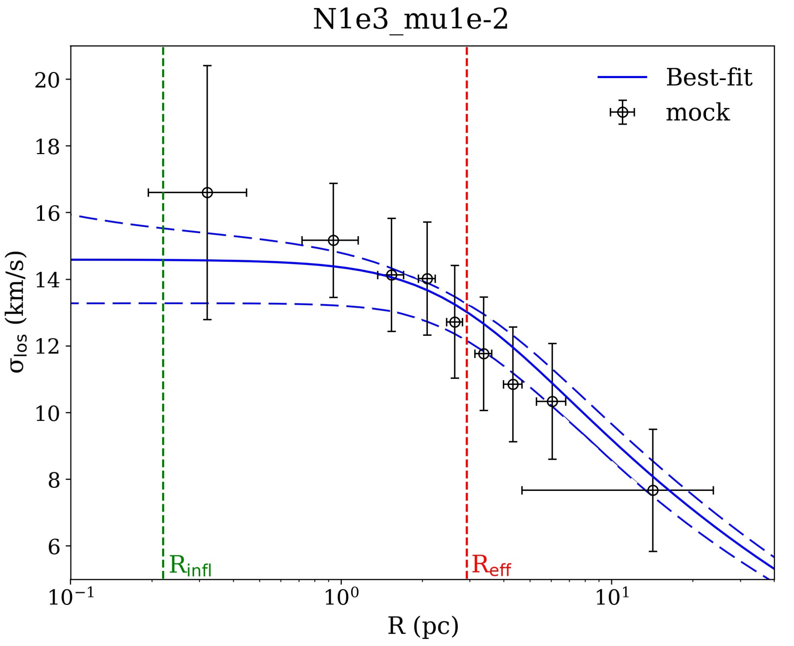

Figure 4.4: Same as Figure 4.3, but for mock N1e3_mu1e-2.

of a model with the same η, α, $\mathrm{M}_\star$ and J_0 but without the BH ($\mu_{\rm BH} = 0$, orange line). As a consequence of the gravitational effects of the IMBH, the stars are allowed to have higher velocities in order not to fall onto the BH. Thus, the LOSVD of the best model is sistematically wider than the model without BH (Figure 4.7). The spread of the LOSVD is the line-of-sight velocity dispersion at the considered radius (equation 2.2.27), so, while in the case of mock N1e4_mu1e-2, the model without IMBH has $\sigma_{\rm los}(R_{\rm infl}) \simeq 13.40$ km/s, the best fit model (which includes an IMBH of $\mu_{\rm BH} = 0.02$) has $\sigma_{\rm los}(R_{\rm infl}) \simeq 15.63$ km/s. Indeed, as we explained in Section 1.2.1 and as it can be noted also in Figure 4.3, a cusp in the central parts of the line-of-sight velocity dispersion profiles of a stellar system can be an indication of the presence a central IMBH have. In case of mock N1e3_mu1e-2, such difference is not appreciable, and both the models have $\sigma_{\rm los}(R_{\rm infl}) \simeq 14.56$ km/s.

We also compare such LOSVDs with the true LOSVD, at $R_{\rm infl}$, of the mock (green line) and the LOSVD of the best fit model with $\mu_{\rm BH} = \mu_{\rm BH,true} = 0.01$ (red line). From a qualitative analysis of such velocity distributions, we can notice that the best model with $\mu_{\rm BH} = \mu_{\rm BH,true} = 0.01$ better reproduces the LOSVD of the mock. This suggests that using individual stellar velocities to fully exploit the kinematic information contained in the DF (for instance the LOSVD) can allow one to put tighter constraints on the dynamical properties of the system (in this case $\mu_{\rm BH}$). We note that here, in all cases, with $R_{\rm infl}$ we mean the radius of influence of the mock, thus calculated with the true value of $\mu_{\rm BH}$.

A different insight is given by Figures 4.9 and 4.10, where we show the two dimensional confidence levels on the free parameters of mocks N1e4_mu1e-2 and N1e3_mu1e-2, respectively. In both cases the true value of $\mu_{\rm BH} = 0.01$ falls within at least 3σ, even though, as previously mentioned, in N1e3_mu1e-2 it is also consistent with no BH even at 1σ. The total stellar mass of the mock GCs is always tigthly recovered and, as discussed in Section 2.3.3, the parameters α and η are slightly degenerate (top left panel of Figures 4.9 and 4.10): an increase of α can be compensated, in terms of quality of the fit, by an increase of η, and vice versa. While α and η are degenerate in determining the structural properties of a model, η controls almost completely the anisotropy distribution of a model. As η incrases also the radial bias of a model increases. In the middle left panels of Figures 4.9 and 4.10 we also notice that η is degenerate with $\mu_{\rm BH}$. This is the known mass-anisotropy degeneracy (see Section 1.2.2): the trade off between radial bias and mass of the IMBH is such that a model with a high value of η (radially biased) can be consistent with no BH.

4.1.1 $\chi^2_{\rm tot}$ dependence on the characteristic action scale J_0

As discussed in Section 3.3.1, models having the same triplet of free parameters $(\alpha, \eta, \mu_{\rm BH})$ are homologous, meaning that the models can be scaled on one another just changing their physical scales. In our models, such scales are given by the characteristic action scale J_0 and the total stellar mass $\mathrm{M}_\star$. In Section 3.3.1 we described the method we used to explore how the models respond to variations of $\mathrm{M}_\star$, while we just set the models spatial scale fixing the parameter r_0 to values that make the mock and models effective radius equal. We did not explore variation of r_0 (and thus J_0) and here we motivate this choice. From equation 2.3.14, J_0 can be written as

$$J_0 = \sqrt{G\mathrm{M}_\star r_0}. \tag{4.1.1}$$

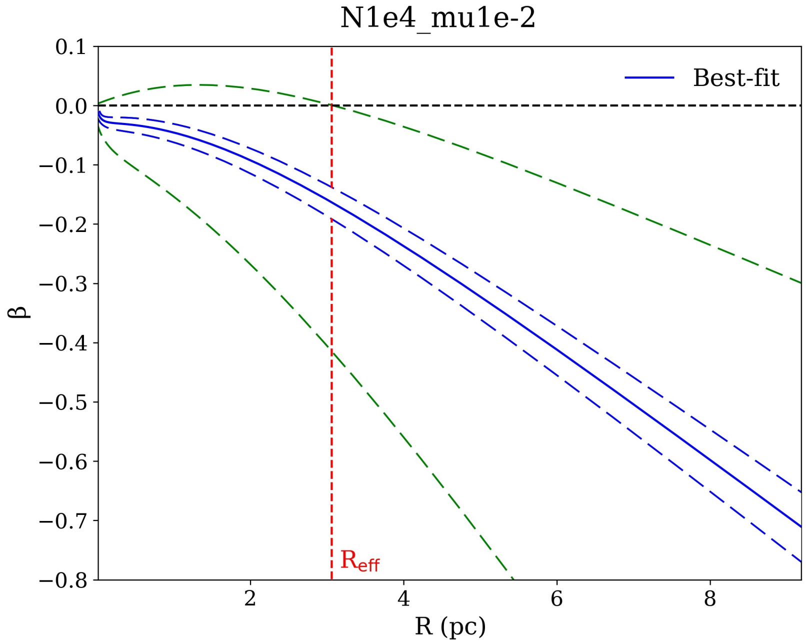

Figure 4.5: Anisotropy parameter profile (see equation 2.2.35) of the best fitting model (blue solid line), the 1σ models (blue dashed line) and the 3σ models (green dashed line; see Table 4.1) of mock N1e4_mu1e-2. We also show the effective radius of the mock ($R_{\rm eff}$, vertical red dashed line, see Table 3.3). The black dashed line is the true value ($\beta = 0$) of the of the isotropic mock.

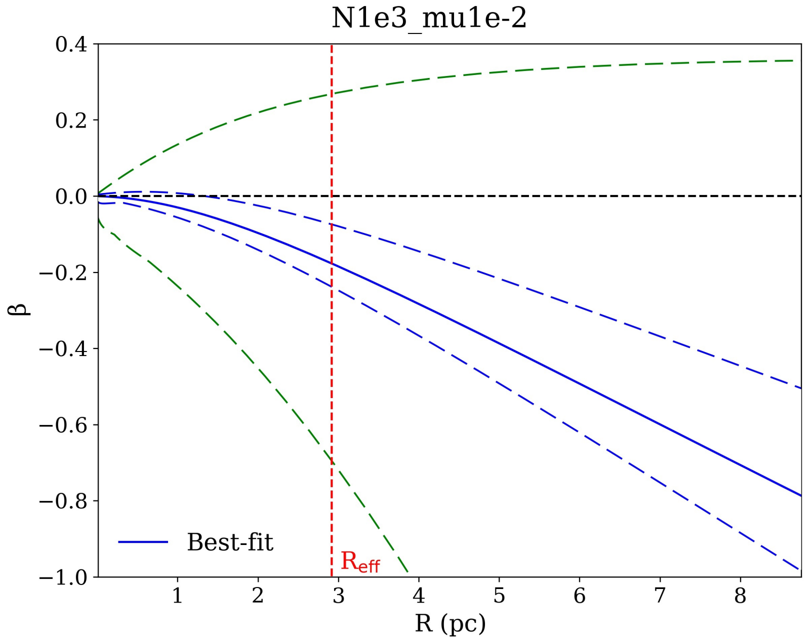

Figure 4.6: Same as Figure 4.5, but for mock N1e3_mu1e-2.

Therefore, when M$_\star$ is fixed, $J_0 \propto r_0^{1/2}$. To show an example, here we tested the variations of $\chi^2_{\rm tot}$ when changing the best fitting characteristic length of the best model of the N1e4_mu1e-2. We changed the value of r_0 of the 2 percent and we re-evaluated the $\chi^2_{\rm tot}$ according to the new values. We find that such rescaled models have $\Delta\chi^2 \equiv \chi^2_{\rm tot} - \chi^2_{\rm best} = 21.73$, where $\chi^2_{\rm best}$ is the value of $\chi^2_{\rm tot}$ of the best model (Table 4.1), greater than the threshold of the 3σ confidence levels (see Table 3.5). This is true for all the considered mocks. Therefore ,considering the large variations it generates in the $\chi^2_{\rm tot}$ of a model, throughout our analysis of the parameter space, we considered r_0 fixed to $r_{0,f}$ as described in Section 3.3.1.

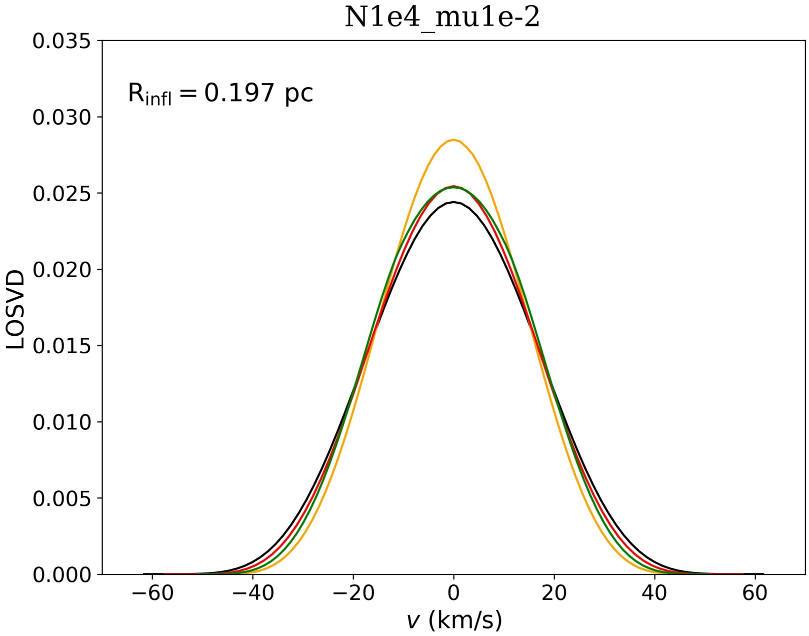

Figure 4.7: LOSVD (equation 2.2.24) of the the best fit model (black line, Table 4.1) of mock N1e4_mu1e-2, superimposed to the LOSVDs of the mock (green line), of a model having the same parameters of the best fit one, but with no IMBH (orange line) and of the best fitting model with $\mu_{\rm BH} = \mu_{\rm BH,true} = 0.01$ (red line), evaluated at the radius of influence of the IMBH ($R_{\rm infl}$, Table 3.4).

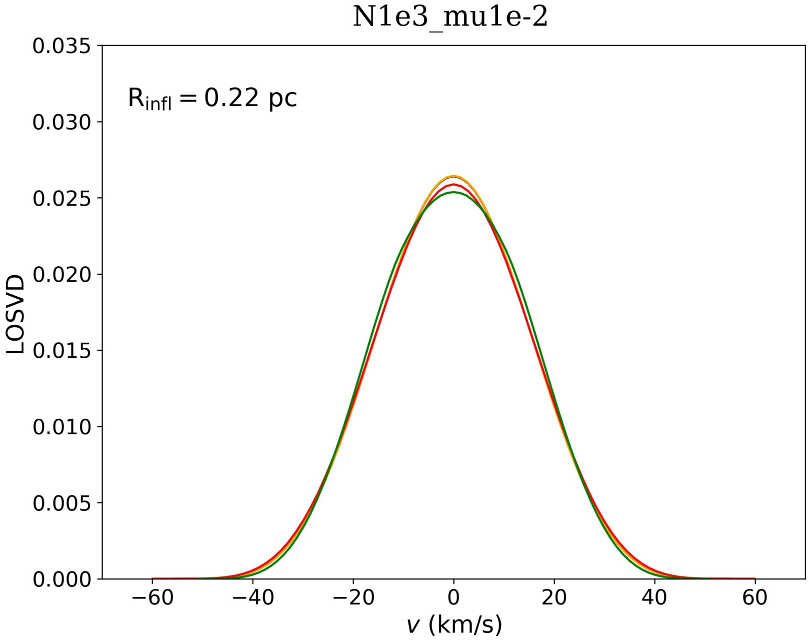

Figure 4.8: Same as Figure 4.7, but for N1e3_mu1e-2. Notice that the orange curve and the black curve overlap.

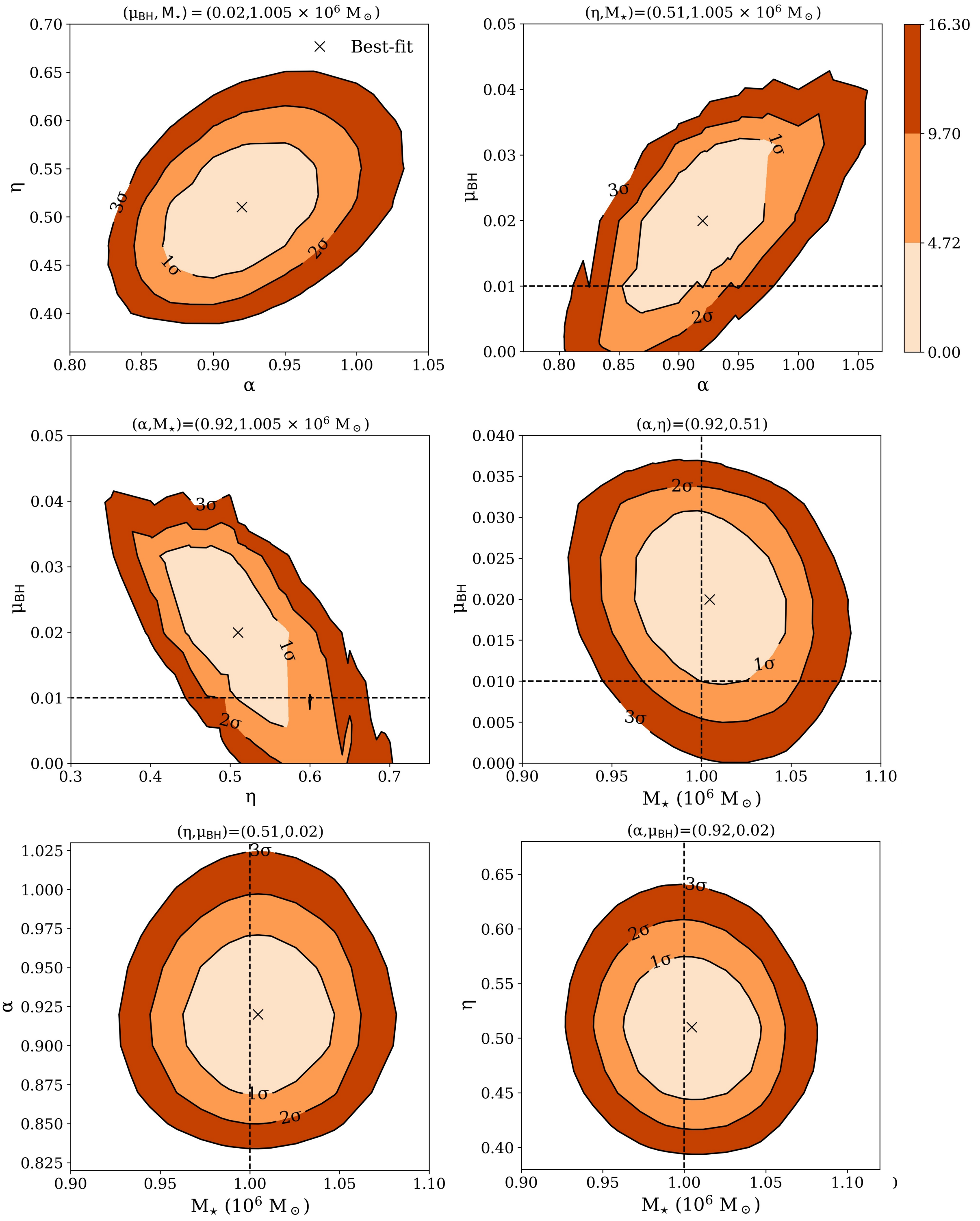

Figure 4.9: Contour plots of the free parameters for the model fitted to the mock GC N1e4_mu1e-2. Each plot has been obtained fixing the other two parameters to their best fitting values (see Table 4.1), which are also reported in the title of each plot. The black cross is the best fitting model. When present, the vertical black dashed line indicates the true value of the total mass of the mock $M_{\star,\mathrm{true}} = 10^6\,M_{\odot}$, while the horizontal black dashed line indicates the true value of the BH-to-stellar mass ratio $\mu_{\mathrm{BH,true}} = 0.01$ The contour levels have been determined according to Table 3.5, in the case of 4 free parameters.

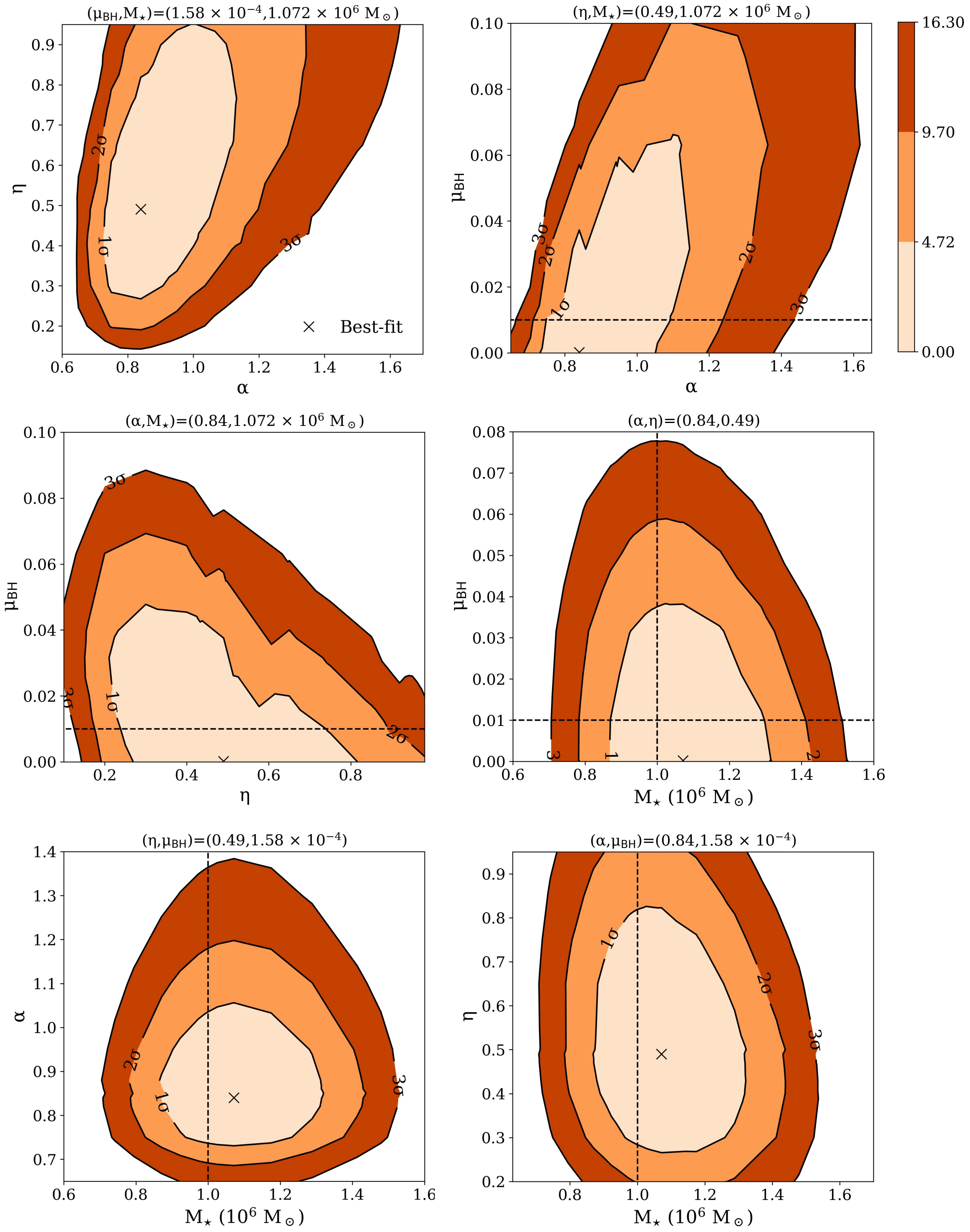

Figure 4.10: Same as Figure 4.9, but for mock N1e3_mu1e-2.

			α	η	$\mu_{\rm BH}$	$\mathrm{M}_\star$ ($10^5\,\mathrm{M}_\odot$)	J_0 (kpc km/s)	$\chi^2_{\Sigma_\star}$	$\chi^2_{\sigma_{\rm los}}$	$\chi^2_{\rm tot}$
H	N1e4_mu1e-2	Best fit	0.92	0.51	0.020	10.05	1.16×10^{-2}	6.05	1.42	7.47
		1σ	$0.90 - 0.94$	$0.50 - 0.52$	$0 - 0.010$	9.89-10.12	-	-	-	-
		3σ	$0.70 - 1.10$	$0.40 - 0.62$	$0 - 0.025$	$7.94 - 14.13$	-	-	-	-
	N1e3_mu1e-2	Best fit	0.84	0.49	1.58×10^{-4}	10.72	2.05×10^{-2}	55.67	21.33	77.00
		1σ	$0.82 - 0.92$	$0.38 - 0.60$	$0 - 0.032$	$9.98 - 11.75$	-	-	-	-
		3σ	$0.70 - 1.10$	$0.25 - 1.10$	$0 - 0.100$	$7.59 - 10.72$	-	-	-	-

Table 4.1: From the left-hand column to the right-hand column: values of the parameters ($\alpha, \eta, \mu_{\rm BH}, \mathrm{M}_\star, J_0$) and of $\chi^2_{\Sigma_\star}$, $\chi^2_{\sigma_{\rm los}}$ and $\chi^2_{\rm tot}$ of the best fit models of mocks N1e4_mu1e-2 and N1e3_mu1e-2 (Best fit). For each parameter we also show the 1σ and 3σ intervals (1σ and 3σ, respectively), except for J_0 (see Section 4.1.1).

4.2 Mock GCs with $\mu_{\rm BH} = 0.001$

We here show the results we obtain when fitting the mocks with $\mu_{\rm BH} = 0.001$ with the our DF-based models. As in the previous Section, we explore how the results depend on the number of particles of the mock in the case of GCs with IMBH as expected extrapolating the Magorrian relation at the GC masses.

Figures 4.11 and 4.12 show the projected number density profiles of the mock GCs N1e4_mu1e-3 and N1e3_mu1e-3 superimposed to the best fitting and the 1σ models. Also in these cases, the flat core of the profiles is well reproduced, while, as for the models of the previous section, in the outskirts the best fitting models decrease more steeply than the ones from the mocks. However, the considerations made in the previous section are still valid, and we consider these outer points of little significance. The inner projected density logarithmic slopes of the best models are $\gamma_{\Sigma_\star}(r \to 0) = -0.031^{+0.031}_{-0.156}$ for N1e4_mu1e-3 and $\gamma_{\Sigma_\star}(r \to 0) = -0.013^{+0.004}_{-0.066}$ for N1e3_mu1e-3, which are consistent with the theoretical value $\gamma_{\Sigma_\star} \simeq 0$ for the innermost regions the mock. As in the previous section, in Table 4.2 we show the values of the parameters of the best fit model fitted to N1e4_mu1e-3 and N1e3_mu1e-3 and the uncertainties given at a confidence levels of 1σ and 3σ.

In Figures 4.13 and 4.14 we show the line-of-sight velocity dispersion profiles of both the mock GCs and the 1σ models. The fact that the innermost point of the line-of-sight velocity dispersion profiles of the mocks is beyond the radius of influence of the BH (see Table 3.4) makes it difficult to constrain the mass of the putative IMBH. Indeed, for both mocks, models with no IMBH are in the 1σ confidence level (Table 4.2) since they well reproduce both the projected number density and line-of-sight velocity dispersion profiles.

For what concerns the anisotropy of the system, Figures 4.15 and 4.16 show the anisotropy profiles as a function of the distance from the center of the best fit models and the 1σ models for mocks N1e4_mu1e-3 and N1e3_mu1e-3, respectively. The values of $\beta(r)$ at the effective radii of the respective mocks are $\beta(R_{\rm eff}) = 0.032^{+0.023}_{-0.042}$ for N1e4_mu1e-3 and $\beta(R_{\rm eff}) = -0.053^{+0.104}_{-0.089}$ for N1e3_mu1e-3. In this case the models better reproduce the isotropic velocity distribution of the mocks, and they are consistent with isotropy within 1σ. This improvement, with respect of the cases of $\mu_{\rm BH} = 0.01$, can be due to the fact that, since the features of the IMBH are less relevant when it is lighter, the model is able to put tighter constraints on the velocity distribution of the system.

Finally, in Figures 4.17 and 4.18 we show the LOSVDs (equation 2.2.24), evaluated at the theoretical radii of influence of the IMBHs of mocks N1e4_mu1e-3 and N1e3_mu1e-3, of their best fit models (black line) and of a model with the same parameters of the best fitting one, but with no IMBH (orange line). In these cases the best fit $\mu_{\rm BH}$ of both the mocks are not high enough to cause an appreciable spread in the LOSVDs of the models, when compared to the case without IMBH. For N1e4_mu1e-3, the model without IMBH has $\sigma_{\rm los}(R_{\rm infl}) \simeq 14.60$ km/s, while the best fit model (having an IMBH of $\mu_{\rm BH} = 0.002$) has $\sigma_{\rm los}(R_{\rm infl}) \simeq 14.69$ km/s. Such a difference is not statistically significant. In the case of N1e3_mu1e-3, with a best fit BH-to-stellar mass fraction of $\mu_{\rm BH} = 3.16 \times 10^{-4}$, its effects are not appreciable, and both the models have $\sigma_{\rm los}(R_{\rm infl}) \simeq 13.33$ km/s.

For these mocks, the LOSVDs of the mocks (green line) is, at least qualitatively, not well reproduced neither by the models described above nor by the best fitting model with $\mu_{\rm BH} = \mu_{\rm BH,true} = 0.001$ is a bit. However, it would be necessary to perform a more

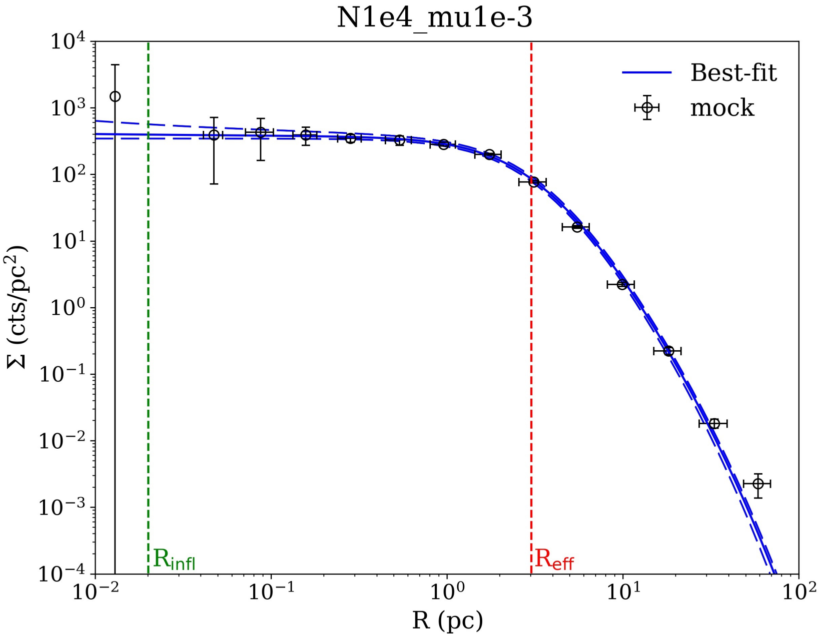

Figure 4.11: Same as Figure 4.1, but for mock N1e4_mu1e-3.

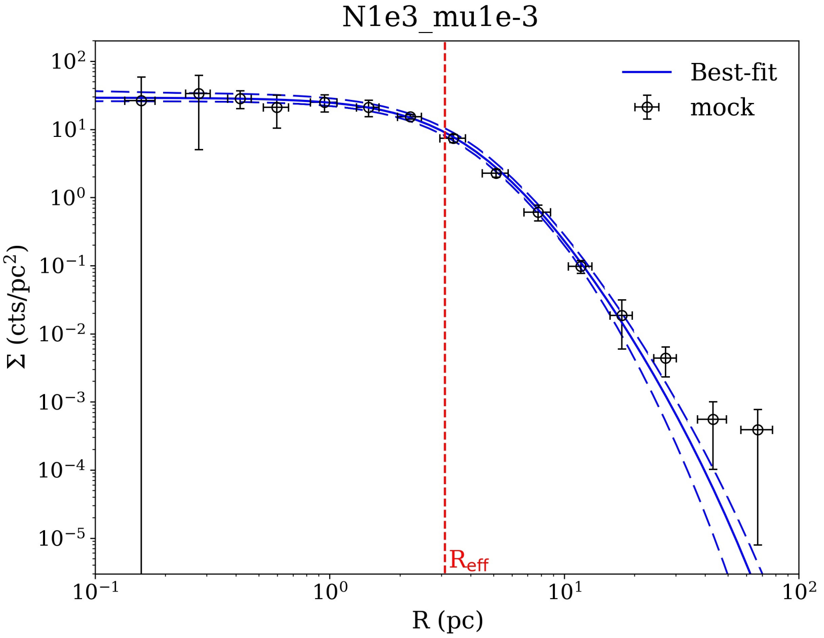

Figure 4.12: Same as Figure 4.1, but for mock N1e3_mu1e-3.

quantitevly and sistematic analysis to understand what are the free parameters of the model that better reproduces the LOSVD of the mock.

The contour plots in the parameter space for N1e4_mu1e-3 models and N1e3_mu1e-3 models are shown in Figures 4.19 and 4.20, respectively. As in the case $\mu_{\rm BH} = 0.01$, also in this $\mu_{\rm BH} = 0.001$ case, the constraints on the values of the parameters are significantly better for $N \simeq 10^4$ than for $N \simeq 10^3$ stars. In the middle left panels of Figures 4.19 and 4.20 we notice again the degeneracy between η and $\mu_{\rm BH}$, which reflects the mass-anisotropy degeneracy. We also notice that $\mu_{\rm BH}$ is degenerate with α: the lower α, the lower $\mu_{\rm BH}$. Due to such degeneracies and to the smaller mass of the IMBH, both in the case of $\sim 10^4$ and $\sim 10^3$ stars, were not able to put any lower limit on the BH mass, which is also compatible with 0 (no BH). Nonetheless, the true values of $\mu_{\rm BH}$ and $\mathrm{M}_\star$ fall within 3σ.

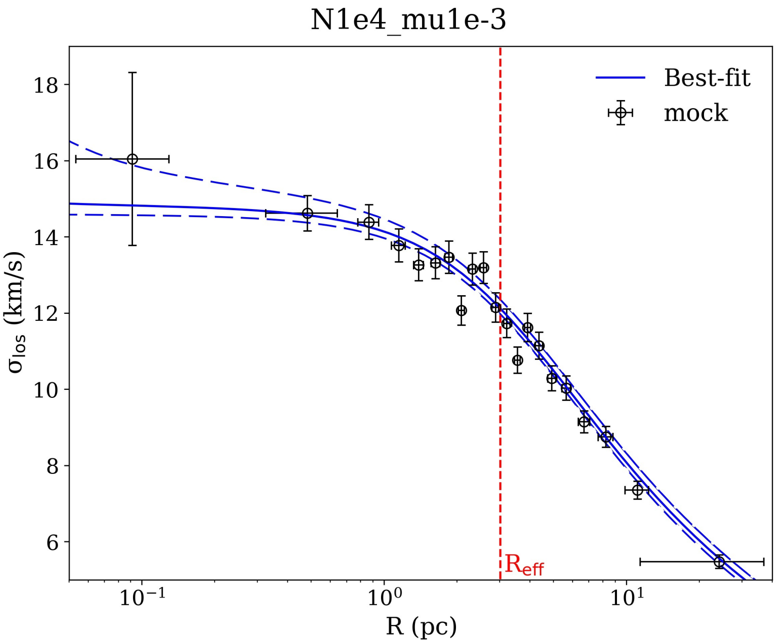

Figure 4.13: Same as Figure 4.3, but for mock N1e4_mu1e-3.

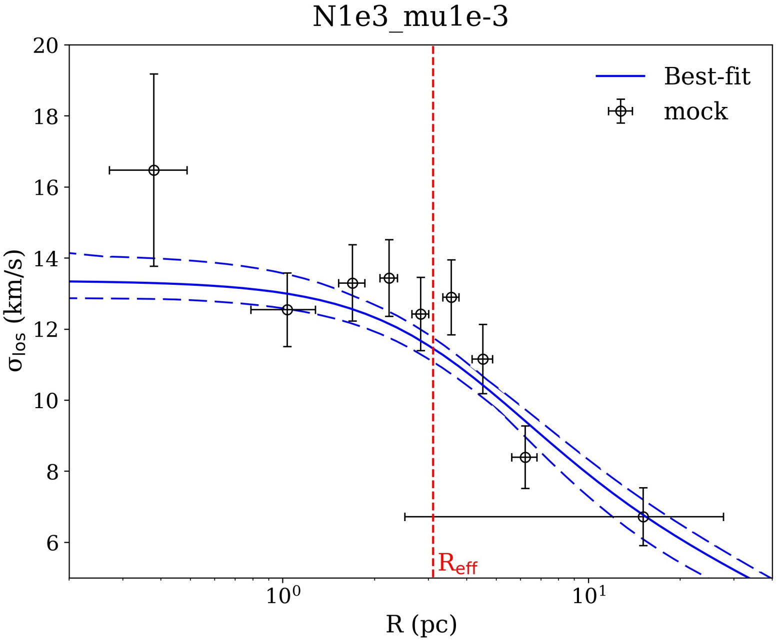

Figure 4.14: Same as Figure 4.3, but for mock N1e3_mu1e-3.

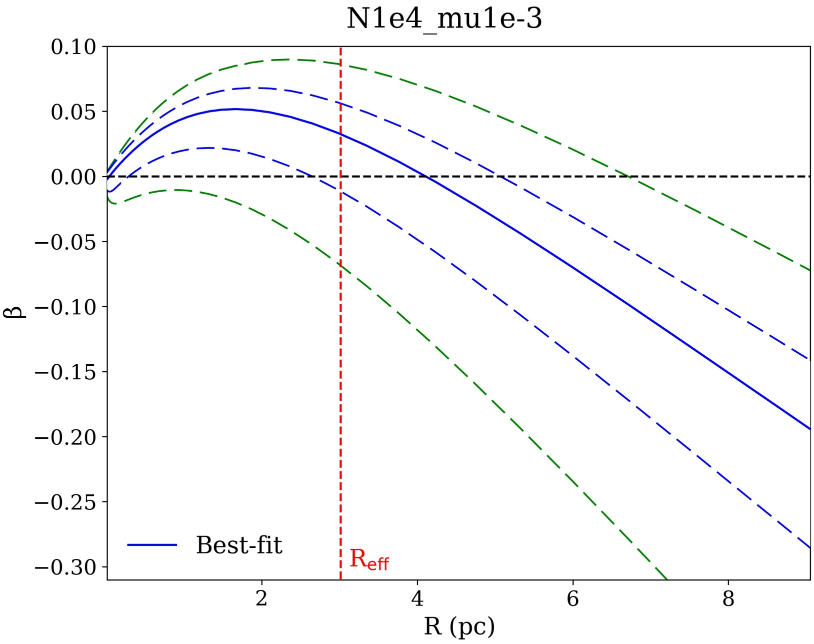

Figure 4.15: Same as Figure 4.5, but for mock N1e4_mu1e-3.

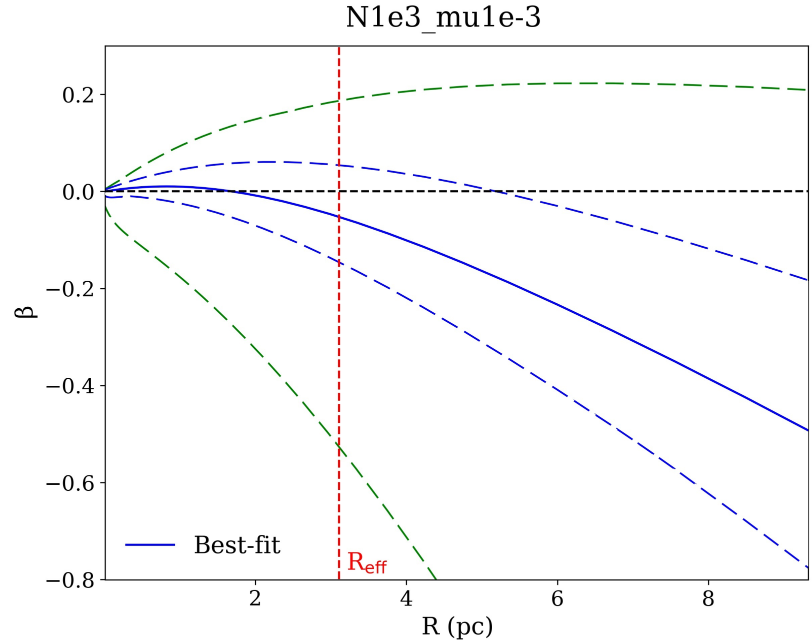

Figure 4.16: Same as Figure 4.5, but for mock N1e3_mu1e-3.

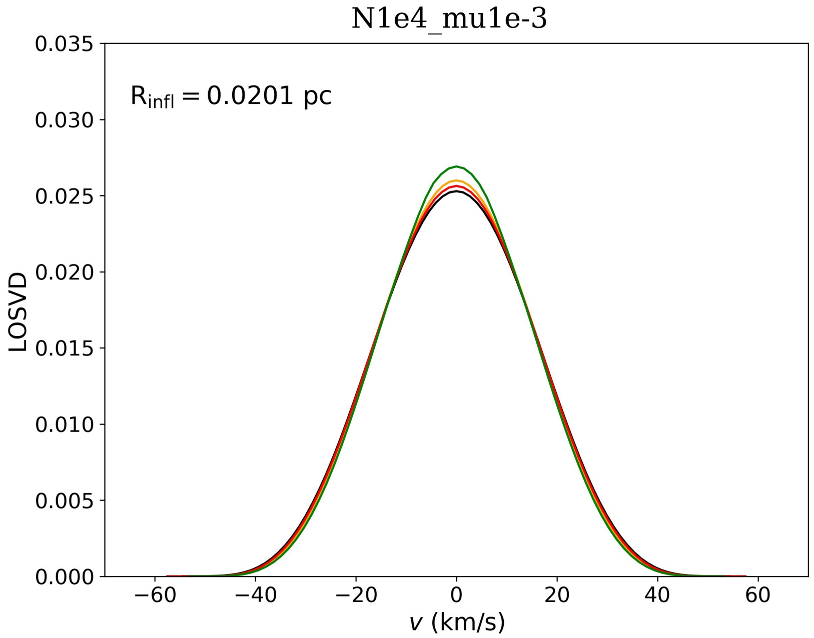

Figure 4.17: Same as Figure 4.7, but for mock N1e4_mu1e-3.

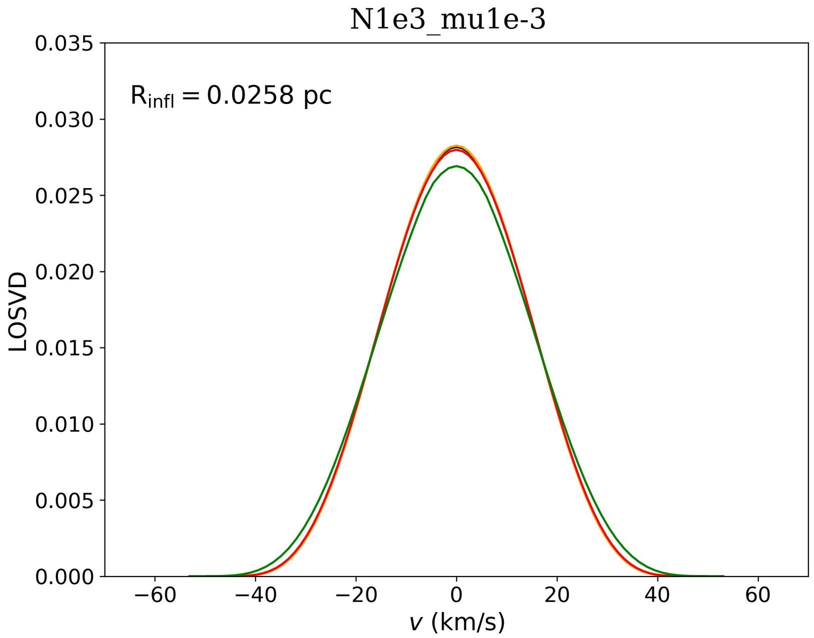

Figure 4.18: Same as Figure 4.7, but for mock N1e3_mu1e-3.

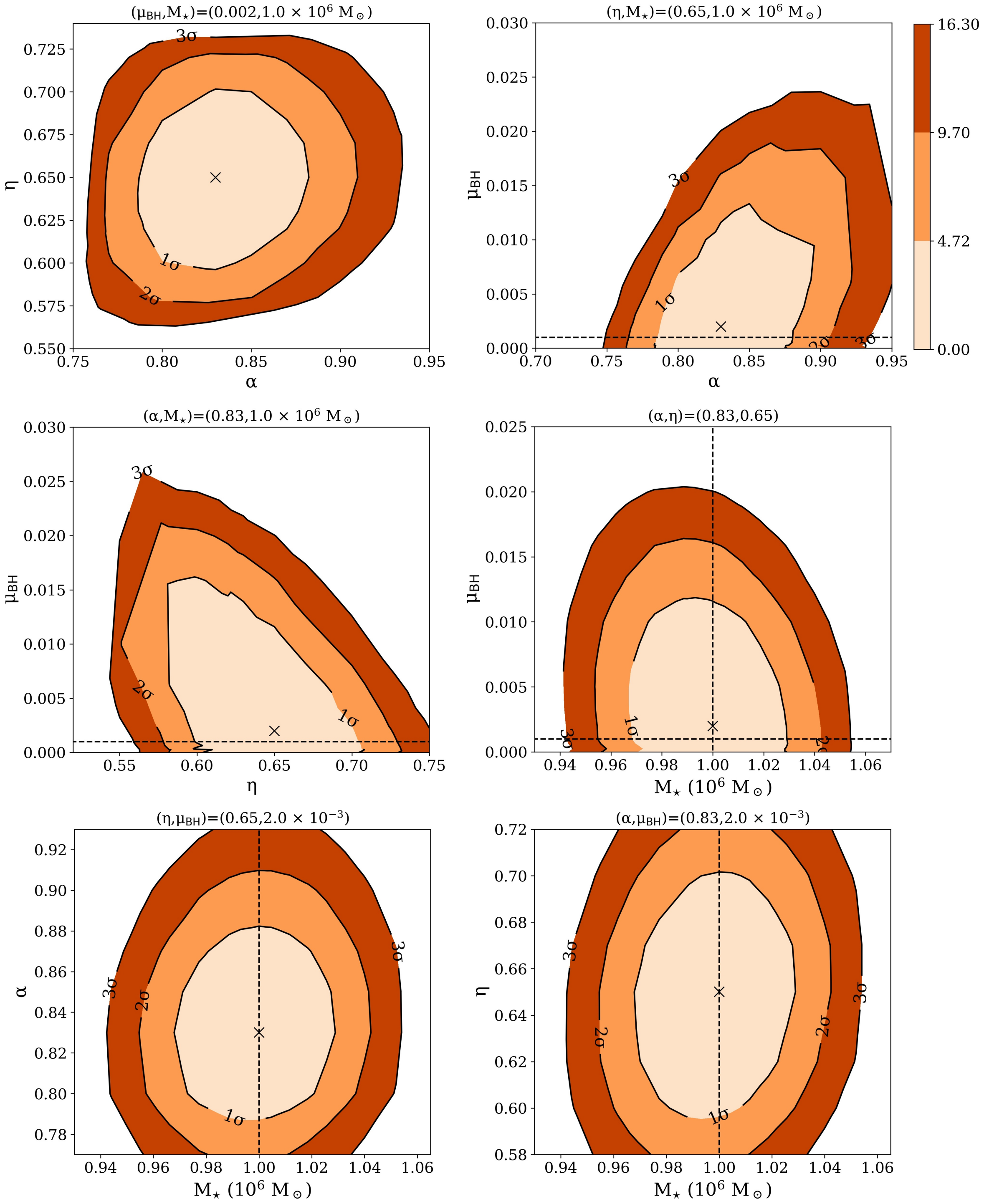

Figure 4.19: Same as Figure 4.9, but for mock N1e4_mu1e-3.

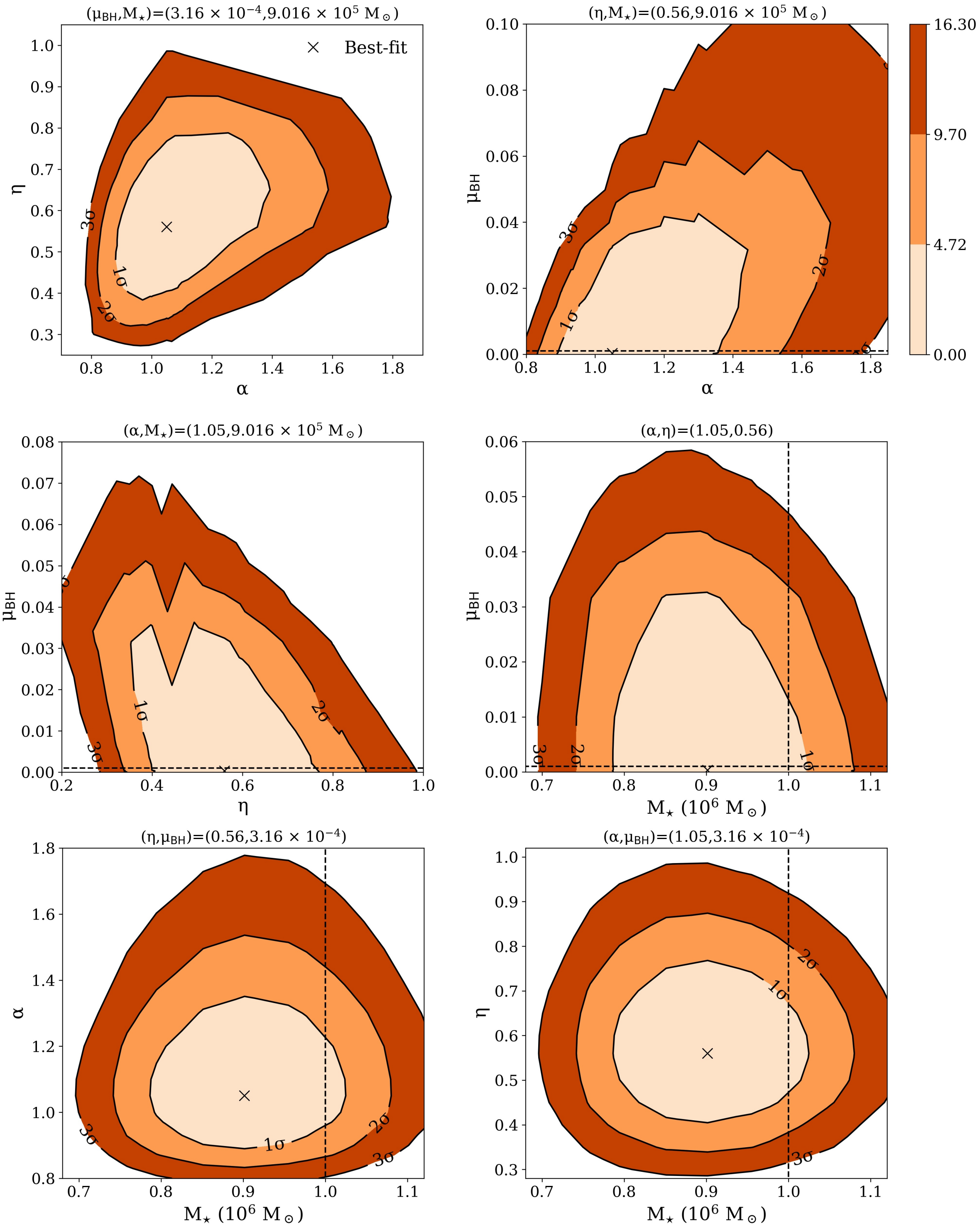

Figure 4.20: Same as Figure 4.9, but for mock N1e3_mu1e-3.

			α	η	μ_{BH}	$\mathrm{M}_\star$ $(10^5\,\mathrm{M}_\odot)$	J_0 (kpc km/s)	$\chi^2_{\Sigma_\star}$	$\chi^2_{\sigma_{\mathrm{los}}}$	χ^2_{tot}
H	N1e4_mu1e-3	Best fit	0.83	0.65	2.0×10^{-3}	10.00	1.37×10^{-2}	55.67	21.33	77.00
		1σ	$1.00 - 1.30$	$0.62 - 0.67$	$0 - 0.010$	$9.89 - 10.12$	-	-	-	-
		3σ	$0.85 - 1.50$	$0.55 - 0.72$	$0 - 0.025$	$9.55 - 10.40$	-	-	-	-
	N1e3_mu1e-3	Best fit	1.05	0.56	3.16×10^{-4}	9.02	2.05×10^{-2}	10.34	6.30	16.64
		1σ	$0.82 - 0.85$	$0.49 - 0.65$	$0 - 0.010$	$8.51 - 9.55$	-	-	-	-
		3σ	$0.77 - 0.93$	$0.29 - 0.82$	$0 - 0.050$	$7.59 - 10.72$	-	-	-	-

Table 4.2: Same as Table 4.1, but for mocks N1e4_mu1e-3 and N1e3_mu1e-3.

Chapter 5

Summary and conclusions

In this Thesis we studied the kinematic and structural properties of GCs by means of a new family of dynamical models based on analytic DFs depending on the action integrals, focusing on the open question of the presence of IMBHs in the centers of such stellar system.

1. In Chapter 1 we have described GCs and IMBHs. We started with a brief description of the stellar populations of Galactic GCs (Section 1.1.1), which were usually modelled as simple stellar populations, even though observations in the last few years confirmed their nature of multiple stellar populations. We showed that Galactic GCs can be divided into two different populations: a metal-poor, spherical population in the Galactic halo, and a metal-rich population orbiting near the Galactic disk and bulge. We then described the structural and kinematic properties of GCs, which can substantially be modelled as isothermal spheres (Section 1.1.2), even if many dynamical processes can alter the characteristics of such stellar systems (Section 1.1.3), such as dynamical friction, mass segregation and energy equipartition. Afterwards, we briefly listed some of the most important observables that can be obtain through a photometric or spectroscopic observation of a GC (Section 1.1.4).
   For what concerns IMBHs, we started explaining why we expect IMBHs to be in center of GCs, by means of scale relations that correlate the mass of the central BH to macroscopic properties of the host system, such as the system stellar mass or the average velocity dispersion, and that suggests that GCs are perfect candidates to host IMBHs (Section 1.2.1). We then described which are the observational effects that an IMBH produces on the stars of a GC orbiting closer enough to the IMBH, and how this affects the integrated properties of a GC, such as the surface brightness and the line-of-sight velocity dispersion profiles (Section 1.2.1). However, many other dynamical processes can mimic the same effects of an IMBH, such as mass-anisotropy degeneracy, mass segregation or dark remnant clusters, and in Section 1.2.2 we briefly described them. In conclusion, we showed some of the most recent results about the investigation of the presence of IMBHs in GCs, most of which gives conflicting results.

2. In Chapter 2 we introduced the concept of relaxation time $t_{\rm relax}$ as the timescale over which the dynamics of a system changes significantly. We demonstrated that GCs typically have a short $t_{\rm relax}$ enough to allow the system dynamical properties to evolve

in time (therefore they are collisional systems). Nonetheless, the evolution in time of a collisional system can be described as a sequence of collisionless states, allowing us to treat GCs as collisional system under short time intervals (Section 2.1). The description of a collisionless system can be perform by means of DFs: in Section 2.2 and 2.2.1 we exposed how a DF is defined, while Section 2.2.2 is dedicated to Jeans's theorems, which are fundamental tools in the theory of DFs. In Section 2.2.3 we showed how to obtain the moments of a DF, which provide information about the properties of the DF and they can be linked to the observables of a stellar system. We then described two particular families of DFs (Section 2.2.4), showing their peculiarities, and the DFs typically used to model GCs (Section 2.2.5).
In Section 2.3.1 the action-angle phase-space coordinates are introduced, together with their most important properties, while in Section 2.3.2 we exposed the characteristics and properties of action-based DFs. In Sections 2.3.3 and 2.3.4 we introduced the action-based DF that has been used to model the stellar population of the mock GCs that will be studied, together with the adopted technique to obtain the stellar density distribution and gravitational potential when adding an IMBH in the center if such a system.

3. In Chapter 3 we described how the mock GCs of the 5-th Gaia Challenge are generated, together with their main properties. In particular, we focused on the characteristics of the 4 mock GCs that were chosen for this Thesis (Section 3.2): isotropic, with a BH-to-stellar mass fraction $\mu_{\rm BH} = 0.01$ or 0.001, and with $N \simeq 10^4$ or $\simeq 10^3$ stars. We described how we built projected number density and line-of-sight velocity dispersion profiles from the mock GCs, analyizing the dependence of the line-of-sight velocity disperison profile on the adopted binning (Sections 3.2.2, 3.2.3 and 3.2.4). In Section 3.3 we exposed which are the free parameters of our dynamical models, how we obtain the corresponding profiles from our DFs, and how we perform the fit to the mock profiles.

4. Finally, in Chapter 4 we presented our results, showing how our best fitting models compare with the mocks discussing our inferences on the parameters of the mocks, and in particular on the mass of the IMBH.

5.1 Conclusions

Here we discuss the results exposed in Section 4. The properties of the considered mocks are described in Section 3.2: we chose 4 isotropic mock GCs, with a BH-to-stellar mass fraction $\mu_{\rm BH} = 0.01$ or 0.001, and with $N \simeq 10^4$ or $\simeq 10^3$ stars, in order to test the dependence of the quality of the fit on the the mass of the BH and on the amount of available data. The model we adopted to describe the stellar populations of such mocks is based on a DF depending on the action integrals, to which the gravity of a central IMBH is added according to Section 2.3.4. The free parameters of such a model are $(\alpha, \eta, \mu_{\rm BH}, {\rm M}_\star, J_0)$, where α and η are dimensionless parameters mainly regulating the structural and kinematic properties of the system, respectively, $\mu_{\rm BH}$ is the BH-to-stellar mass fraction, ${\rm M}_\star$ is the total mass of the system and J_0 is a characteristic action scale.

For what concerns the presence of an IMBH in the center of the mock GCs, the true value of μ_{BH} is found to be within at least 2σ in all the cases. In particular:

- for mocks with $\simeq 10^4$ stars, the true value of μ_{BH} is within 2σ in the case of N1e4_mu1e-2 ($\mu_{\mathrm{BH,true}} = 0.01$), while it falls within 1σ in the case of N1e4_mu1e-3 ($\mu_{\mathrm{BH,true}} = 0.001$);
- for mocks with $\simeq 10^3$ stars, the true value of μ_{BH} is within 1σ both in the case of N1e3_mu1e-2 ($\mu_{\mathrm{BH,true}} = 0.01$) and N1e4_mu1e-3 ($\mu_{\mathrm{BH,true}} = 0.001$).

Such results allow us to conclude that we can trust that, for an hypothetical system of known total number of stars N but unknown BH mass (such as a real GC), the real value of μ_{BH} falls within 2σ in the case of $N \simeq 10^4$ and 1σ in the case of $N \simeq 10^3$. Thus, these would be our inferences on μ_{BH} of the mocks when $N \simeq 10^4$:

- $\mu_{\mathrm{BH}} = 0.020^{+0.012}_{-0.014}$ when $\mu_{\mathrm{BH,true}} = 0.01$, corresponding to a mass $\mathrm{M}_{\mathrm{BH}} = 2^{+1.29}_{-1.38} \times 10^4\,\mathrm{M}_{\odot}$;
- $\mu_{\mathrm{BH}} \leqslant 0.020$ when $\mu_{\mathrm{BH,true}} = 0.001$, corresponding to $\mathrm{M}_{\mathrm{BH}} \leqslant 2.05 \times 10^4\,\mathrm{M}_{\odot}$.

Instead, when $N \simeq 10^3$ our inferences on μ_{BH} would be:

- $\mu_{\mathrm{BH}} \leqslant 0.013$ when $\mu_{\mathrm{BH,true}} = 0.01$, corresponding to $\mathrm{M}_{\mathrm{BH}} \leqslant 1.48 \times 10^4\,\mathrm{M}_{\odot}$;
- $\mu_{\mathrm{BH}} \leqslant 0.010$ when $\mu_{\mathrm{BH,true}} = 0.001$, corresponding to $\mathrm{M}_{\mathrm{BH}} \leqslant 9.55 \times 10^3\,\mathrm{M}_{\odot}$.

This is mainly due to the lack of stars within the radius of influence of the BH (see Section 3.2.4) for all the mocks except for N1e4_mu1e-2.

Focusing on the velocity distribution, all the mocks we have considered are isotropic, therefore $\beta \equiv 0$ independent of the radius. As shown by Pascale et al. (2019), the DF we used in this Thesis in general does not produce systems with exactly a flat anisotropy profile, and modifying the DF 2.3.11 in order to make it able to generate such anisotropy profiles would require the addition of more free parameters. We were able to recover isotropy within 1σ in case of the mocks N1e4_mu1e-3 and N1e3_mu1e-3, while, for N1e4_mu1e-2 and N1e3_mu1e-2, we recover it within 3σ. As pointed out in Sections 4.1 and 4.2, the fact that the model better infers the anisotropy of the mock with a smaller μ_{BH} can be an indication of the fact that the DF 2.3.11 is not flexible enough, even if this does not affect the ability of the models to infer the correct BH-to-stellar mass fraction.

Finally, the true total mass of the system $\mathrm{M}_{\star} = 10^6\,\mathrm{M}_{\odot}$ falls within 1σ in case of $N \simeq 10^4$, while it is at most within 2σ for the mocks within $N \simeq 10^3$. Thus, we can trust that, for a system of unknown total mass, the real value of $\mathrm{M}_{\star}$ falls within 1σ if $N \simeq 10^4$ or within 2σ if $N \simeq 10^3$. Therefore, these would be our inferences on $\mathrm{M}_{\star}$ of the mocks when $N \simeq 10^4$:

- $\log(\mathrm{M}_{\star}/\mathrm{M}_{\odot}) = 6.002^{+0.003}_{-0.003}$ when $\mu_{\mathrm{BH,true}} = 0.01$;
- $\log(\mathrm{M}_{\star}/\mathrm{M}_{\odot}) = 6.000^{+0.005}_{-0.005}$ when $\mu_{\mathrm{BH,true}} = 0.001$.

Instead, when $N \simeq 10^3$ our inferences on $\mathrm{M}_\star$ would be:

- $\log(\mathrm{M}_\star/\mathrm{M}_\odot) = 6.03^{+0.0083}_{-0.008}$ when $\mu_{\mathrm{BH,true}} = 0.01$;
- $\log(\mathrm{M}_\star/\mathrm{M}_\odot) = 5.955^{+0.050}_{-0.055}$ when $\mu_{\mathrm{BH,true}} = 0.001$.

To improve these results more data are necessary, especially coming from the innermost regions of the GCs. While a total number of stars $N \simeq 10^4$ seems to be enough to allow the model to put tight constraints on η and $\mathrm{M}_\star$, for BH-to-stellar mass fractions of $\mu_{\mathrm{BH}} = 0.001$, more stars seem to be necessary to constrain μ_{BH}. In particular, as it can be noticed in Table 3.4, in the case of N1e4_mu1e-2 ($N \simeq 10^4$ and $\mu_{\mathrm{BH}} = 0.01$), which is the mock for which we can exclude the absence of an IMBH, there are 50 stars within the influence radius of the IMBH R_{infl} (equation 1.2.3), while in the other mocks there are always less then 6 stars within R_{infl}. Having an amount of stars closer to those available for N1e4_mu1e-2 may bring enough statistics in order to exclude models with no BH.

5.2 Future applications

A promising alternative is the application of action-based DFs to single stars measurements. As the DFs are probability density functions, they provide the probability of finding a star in a certain volume of the phase space (Section 2.2). Thus, the probability of having a sample of stars of known positions on the plane of the sky and line-of-sight velocities, for instance, is the sum of the probabilities that each star is found those projected phase-space coordinates. The best fit model will be that which maximizes such probability. Moreover, using individual stellar velocity would allow us to exploit fully the kinematic information contained in the DF (for instance the LOSVD) and not only the line-of-sight velocity dispersion.

One of the possible extensions is including also proper motions (PMs) as observables (see Section 1.1.4). As shown by van der Marel & Anderson (2010) and Baumgardt et al. (2019), PMs allow one to have a complete view of the velocity distribution of the system, highly improving our capability to infer the behaviour of $\beta(r)$. Once the anisotropy parameter is well constrained, the mass-anisotropy degeneracy (Section 1.2.2) can be broken, allowing us to better constrain μ_{BH}, too.

Alternatively, one can apply different action-based DFs, looking for the DF that better reproduces the observational data. For instance, to better reproduce the velocity distribution of the mocks, one could use a more flexible DF, such as the action-based DF presented by Posti et al. (2015), or the DF implemented in AGAMA Vasiliev (2019), which is a generalization of both the DFs by Posti et al. (2015) and Pascale et al. (2018). However, these DFs have many more free parameters than one adopted in this Thesis (equation 2.3.11).

Action-based DFs can be extended to rotating and flattened systems, as pointed out in Section 2.3.2. As described in Section 1.1.2, many GCs possess non-negligible flattening and net rotation, thus a suitable model should take them into account. It is also possible to apply action-based DFs to rotating mocks, as those built by S. Rozier and included in 5-th Gaia Challenge, too. Indeed, as stated in Section 2.3.2, these models can be modified to include both flattening and rotation, becoming suitable to model axisymmetric systems.

All these applications, however, should always aim to the application of these models to real observational data, in order to concretely study the structure and kinematics of GCs, and the presence of IMBHs in these systems. However, as stated in Section 1.1.4, many issues arise when dealing with real observational data, such as contamination by field stars or position dependent mass-to-light ratio M/L, which must be carefully accounted for, especially when looking for IMBHs in the center of GCs, where many other dynamical effects can mimic the presence of a central BH, such as mass segregation and energy equipartition (Section 1.2.2).

Acknowledgments

I would like to warmly thank my supervisor, Professor Carlo Nipoti, and my co-supervisor, Dr. Raffaele Pascale. Thanks for having constantly guided me in this fascinating project, for their constant and dedicated willingness, for everything they have taught me during these months and which I will treasure. Those who know me know how much I wanted to collaborate with them and I hope, at least a little bit, to have earned their esteem, because, for my part, they have had such a lot of it for a long time.

I also thank Dr. Francesco Calura for the helpful comments and tips on an earlier version of the manuscript.

Bibliography

Alessandrini E., Lanzoni B., Miocchi P., Ciotti L., Ferraro F. R., 2014, ApJ, 795, 169

Anderson J., van der Marel R. P., 2010, ApJ, 710, 1032

Arca Sedda M., Askar A., Giersz M., 2018, MNRAS, 479, 4652

Bahcall J. N., Wolf R. A., 1976, ApJ, 209, 214

Barmby P., Huchra J. P., 2001, AJ, 122, 2458

Bastian N., Lardo C., 2018, ARA&A, 56, 83

Baumgardt H., 2017, MNRAS, 464, 2174

Baumgardt H. et al., 2019, MNRAS, 488, 5340

Beasley M. A., 2020, Reviews in Frontiers of Modern Astrophysics, 245–277

Bertin G., 2000, Dynamics of Galaxies

Binney J., 2010, MNRAS, 401, 2318

Binney J., 2012, MNRAS, 426, 1328

Binney J., 2014, MNRAS, 440, 787

Binney J., Mamon G. A., 1982, MNRAS, 200, 361

Binney J., Merrifield M., 1998, Galactic Astronomy

Binney J., Tremaine S., 2008, Galactic Dynamics: Second Edition

Breen P. G., Heggie D. C., 2013, MNRAS, 436, 584

Carroll B. W., Ostlie D. A., 1996, An Introduction to Modern Astrophysics

Chandrasekhar S., 1943, ApJ, 97, 255

Cimatti A., Fraternali F., Nipoti C., 2019, arXiv e-prints, arXiv:1912.06216

Cole D. R., Binney J., 2016, Monthly Notices of the Royal Astronomical Society, 465, 798

Djorgovski S., King I. R., 1986, ApJ, 305, L61

Event Horizon Telescope Collaboration et al., 2019, ApJ, 875, L1

Fragione G., Ginsburg I., Kocsis B., 2018, ApJ, 856, 92

Gaia Collaboration et al., 2018, A&A, 616, A1

Gao B., Goodman J., Cohn H., Murphy B., 1991, ApJ, 370, 567

Gieles M., Zocchi A., 2015, MNRAS, 454, 576

Greene J. E., Strader J., Ho L. C., 2019, arXiv e-prints, arXiv:1911.09678

Hamilton C., Fouvry J.-B., Binney J., Pichon C., 2018, MNRAS, 481, 2041

Harris W. E., 1996, AJ, 112, 1487

Heggie D. C., 1975, MNRAS, 173, 729

Holley-Bockelmann K., Gültekin K., Shoemaker D., Yunes N., 2008, ApJ, 686, 829

Jalali B., Baumgardt H., Kissler-Patig M., Gebhardt K., Noyola E., Lützgendorf N., de Zeeuw P. T., 2012, A&A, 538, A19

Jeans J. H., 1915, MNRAS, 76, 70

Jeffreson S. M. R. et al., 2017, MNRAS, 469, 4740

Kaaret P., Feng H., Roberts T. P., 2017, ARA&A, 55, 303

King I. R., 1966, AJ, 71, 64

Lanzoni B., Dalessandro E., Ferraro F. R., Miocchi P., Valenti E., Rood R. T., 2007, ApJ, 668, L139

Lanzoni B. et al., 2013, ApJ, 769, 107

Lützgendorf N., Gebhardt K., Baumgardt H., Noyola E., Neumayer N., Kissler-Patig M., de Zeeuw T., 2015, A&A, 581, A1

Lützgendorf N., Kissler-Patig M., Noyola E., Jalali B., de Zeeuw P. T., Gebhardt K., Baumgardt H., 2011a, A&A, 533, A36

Lützgendorf N., Kissler-Patig M., Noyola E., Jalali B., de Zeeuw P. T., Gebhardt K., Baumgardt H., 2011b, A&A, 533, A36

Magorrian J. et al., 1998, AJ, 115, 2285

Mann C. R. et al., 2019, ApJ, 875, 1

Merritt D., 1985, MNRAS, 214, 25P

Meylan G., Heggie D. C., 1997, A&ARv, 8, 1

Michie R. W., Bodenheimer P. H., 1963, MNRAS, 126, 269

Miocchi P., 2006, MNRAS, 366, 227

Miocchi P., 2007, MNRAS, 381, 103

Noyola E., Gebhardt K., Bergmann M., 2008, ApJ, 676, 1008

Noyola E., Gebhardt K., Kissler-Patig M., Lützgendorf N., Jalali B., de Zeeuw P. T., Baumgardt H., 2010, ApJ, 719, L60

Osipkov L. P., 1979, Soviet Astronomy Letters, 5, 42

Pascale R., Binney J., Nipoti C., Posti L., 2019, MNRAS, 488, 2423

Pascale R., Posti L., Nipoti C., Binney J., 2018, MNRAS, 480, 927

Plummer H. C., 1911, MNRAS, 71, 460

Posti L., Binney J., Nipoti C., Ciotti L., 2015, MNRAS, 447, 3060

Press W. H., Teukolsky S. A., Vetterling W. T., Flannery B. P., 1992, Numerical recipes in FORTRAN. The art of scientific computing

Pryor C., Meylan G., 1993, in Astronomical Society of the Pacific Conference Series, Vol. 50, Structure and Dynamics of Globular Clusters, Djorgovski S. G., Meylan G., eds., p. 357

Salaris M., Cassisi S., 2005, Evolution of Stars and Stellar Populations

Sanders J. L., Binney J., 2014, MNRAS, 441, 3284

Sanders J. L., Binney J., 2016, MNRAS, 457, 2107

Sargent W. L. W., Young P. J., Boksenberg A., Shortridge K., Lynds C. R., Hartwick F. D. A., 1978, ApJ, 221, 731

Sparke L. S., Gallagher, John S. I., 2007, Galaxies in the Universe: An Introduction

Spitzer, Lyman J., 1969, ApJ, 158, L139

The LIGO Scientific Collaboration et al., 2020, arXiv e-prints, arXiv:2009.01075

Tremou E. et al., 2018, ApJ, 862, 16

Trenti M., Vesperini E., Pasquato M., 2010, ApJ, 708, 1598

van de Ven G., van den Bosch R. C. E., Verolme E. K., de Zeeuw P. T., 2006, A&A, 445, 513

van der Marel R. P., Anderson J., 2010, ApJ, 710, 1063

Vasiliev E., 2019, MNRAS, 482, 1525

Vesperini E., Trenti M., 2010, ApJ, 720, L179

White R. E., Shawl S. J., 1987, ApJ, 317, 246

Wilson C. P., 1975, AJ, 80, 175

Xiao T., Barth A. J., Greene J. E., Ho L. C., Bentz M. C., Ludwig R. R., Jiang Y., 2011, ApJ, 739, 28

Zinn R., 1985, ApJ, 293, 424